A machine-learning approach to exoplanet spectroscopy

High-precision data analysis of spectrophometric observations of exoplanetary transits and eclipses

Giuseppe Morello

Submitted for the degree of Doctor of Philosophy

Department of Physics and Astronomy

University College London

I, *Giuseppe Morello*, confirm that the work presented in this Thesis is my own.

Where information has been derived from other sources, I confirm that this has been indicated in the Thesis.

Abstract

The characterization of exoplanetary atmospheres is the new frontier in the field of exoplanets. Transit and eclipse spectroscopy are invaluable sources of information, as they may reveal the chemical composition, the presence of clouds, and the temperature and pressure profiles of the atmospheres of exoplanets. A photometric precision of about one part in 10^4 is necessary to make statistically significant inferences. The native calibration of current observatories, except Kepler, is not sufficient to reach this precision. In the past, parametric models have been used extensively by most teams to remove instrumental systematics. This approach has caused many debates regarding the use of different parametric choices for the removal of systematic errors. Parametric models decorrelate the systematic noise with the aid of auxiliary information on the instrument: the so-called optical state vectors (OSVs). Such OSVs can include inter- and intra-pixel position of the star or its spectrum, instrument temperatures and inclinations, and/or other parameters. The choice of the parameters to include in the OSVs is somewhat arbitrary, as is the choice of the functional forms to approximate the dependence of systematic noise on those parameters.

The solution to many of the issues deriving from the use of OSVs lies in the use of 'blind', non-parametric techniques. Such methods do not require a model for the systematics, and for this reason, they can be applied to any instrument with few changes (if any). In this Thesis, I focus on the Independent Component Analysis (ICA) of multiple time series, which performs a linear transformation of those series into maximally independent components. The use of ICA to detrend instrument systematics in exoplanetary light-curves was first proposed by Waldmann (2012). They experimented with spectroscopic light-curves taken with *HST*/NICMOS and sequential Kepler observations as input light-curves for the ICA. In this Thesis, I present two novel approaches to detrend single photometric observations in a self-consistent way (pixel-ICA), and scanning-mode spectroscopic observations without mixing the signals at different wavelengths (stripe-ICA). The two techniques that I pioneered extend the applicability of ICA to single observations with different instrument design. Some unsupervised preprocessing steps are also tested. The better performances of these algorithms compared to other ones in the literature are demonstrated over a series of Spitzer and Hubble observations, and synthetic data sets.

The (re)analysis of archive and new data with similar techniques will cast new light on the characterization of exoplanets.

With unreserved thanks to all those who have helped me along the way.

Contents

List of Figures

List of Tables

Chapter 1

Introduction

> *"Of all objects, the planets are those which appear to us under the least varied aspect. We see how we may determine their forms, their distances, their bulk, and their motions, but we can never known anything of their chemical or mineralogical structure; and, much less, that of organized beings living on their surface ..."*
>
> — **Auguste Comte, The Positive Philosophy, 1842**

The pessimistic statement of the philosopher August Comte reported above has been spectacularly overcome with the rapid scientific and technological progress of the last two centuries. The predicted limit was motivated by the impossibility, with any foreseeable technology, of traveling to other planets and collecting samples to analyze in a laboratory. Neil Armstrong's step onto the Moon in 1969 officially opened the era of space exploration, followed by a long list of unmanned missions to other objects in our Solar System, e.g. the Mars Rovers (Spirit and Opportunity landed in 2004, Curiosity in 2012), Cassini-Huygens (also Titan's landing in 2005) and Rosetta (comet's landing in 2014) among the most famous ones. In the last two decades, the recent discovery of more than 3,000 extrasolar planets (or exoplanets), i.e. planets orbiting stars other than our Sun, has raised interest in the characterization of these new worlds and reinvigorated the search for alien life. While interstellar travels are now off-limits, remote-sensing spectroscopy enables understanding the exoplanetary composition and environments.

1.1 A steady stream of surprises

The first uncontroversial detection of planet-sized bodies out of the Solar System was reported in a paper entitled "A planetary system around the millisecond pulsar PSR1257 +12" (Wolszczan

and Frail, 1992). Pulsars are rapidly rotating neutron stars, dense remnants of stars which exploded as supernovae, which emit a tremendous amount of high-energy radiation. Such an extreme environment was certainly not the place where astronomers were expecting to discover the first exoplanet.

Three years after this first exoplanet discovery, Michael Mayor and Didier Queloz detected the first exoplanet orbiting around a main-sequence star (Mayor and Queloz, 1995). The planet, 51Peg b, is a gas giant (minimum mass of 0.5 M_J) in a small orbit (semi-major axis of 0.052 AU, orbital period of 4.23 days) around a solar-type star. As a comparison, its orbital semi-major axis is 100 times smaller than Jupiter's (5.2 AU) and 7.4 times smaller than Mercury's (0.387 AU) one. 51Peg b is the prototype of a new class of planets, named hot-Jupiters by the scientific community, which was not predicted by models of giant planet formation.

Successive discoveries have revealed an unexpectedly large variety of exoplanetary types, covering wide ranges in mass, size, density, temperature and orbital parameters. This variety breaks the dichotomy between rocky (silicate) and gaseous (hydrogen) planets observed in our Solar System, and suggests the existence of planets with different compositions, such as ocean planets (e.g. GJ1214 b; Charbonneau et al., 2009), diamond planets (e.g. 55 Cnc e; Madhusudhan et al., 2012), iron planets (e.g. KOI 1843.03; Rappaport et al., 2013) and helium planets (e.g. GJ436 b; Hu et al., 2015).

Some planets have highly eccentric orbits, e.g., HD20782 b ($e = 0.97$; O'Toole et al., 2009), HD80606 b ($e = 0.93$; Naef et al., 2001), which cause extreme seasonal variations. Other peculiarities include planets with significant stellar spin-orbit misalignment (e.g., Kepler 56 d; Huber et al., 2013), circumbinary planets (e.g., HD202206 b; Correia et al., 2005), and even planets in triple-star systems (e.g., HD188753 Ab; Konacki, 2005).

1.2 Thesis outline

The focus of this Thesis is the development of new data analysis algorithms that allow investigating the nature of exoplanets, and in particular their atmospheres, through the well-established transit and eclipse spectroscopy techniques. The pipelines that I wrote make use of Independent Component Analysis (ICA), a statistical tool which is largely adopted in several contexts, and it was used for the first time in the field of exoplanets by Waldmann (2012). The pipelines are original as they are specifically designed for different types of observations and instruments compared to the other pipelines that make use of ICA in the previous literature. An additional advantage is that they do not mix information from multiple wavelengths to detrend the transit signal, so that they are not affected by the wavelength-dependence of stellar limb darkening.

In **Chapter 2**, I will introduce to the various detection and characterization methods for exoplanets and present a brief history of the transit/eclipse spectroscopy technique and the current need of objective and effective algorithms for the data analysis.

Chapter 3 reports technical details relative to the transit/eclipse spectroscopy.

In **Chapter 4**, I describe Independent Component Analysis.

Chapter 5 is dedicated to the pixel-ICA algorithm and the results of its application over *Spitzer*/IRAC observations of the transits of two exoplanets, HD189733b and GJ436b.

Chapter 6 shows further results obtained by applying the same technique over simulated observations with a list of instrument behaviours that I generated, in order to test the strenghts and the limits of the pixel-ICA technique in a general context.

In **Chapter 7**, the wavelet pixel-ICA variant is introduced, with extended applicability to lower signal-to-noise observations and faint exoplanet signals. The results obtained for a set of Warm *Spitzer*/IRAC observations of eclipses of the exoplanet XO3b and a similar set of synthetic data created by the Spitzer Science Center are discussed, in comparison with other state-of-the-art detrending pipelines adopted by other teams. These results are part of the IRAC Data Challenge 2015.

In **Chapter 8**, I describe the stripe-ICA algorithm, designed to detrend *HST*/WFC3 scanning-mode data, and present the preliminary results obtained for the transit of HAT-P 32b.

Chapter 9 is a brief summary of the work discussed in this Thesis and discusses future projects.

Chapter 2

Detection and characterization methods

"... when you have eliminated all which is impossible, then whatever remains, however improbable, must be the truth."

— **Sherlock Holmes –The blanched soldier (A. Conan Doyle)**

2.1 Detection and characterization methods

2.1.1 Doppler spectroscopy

Better known as the radial velocity method, this was the most productive exoplanet detection technique, at least until 2014. To date, 670 planets[1], including 51Peg b, have been discovered using the Doppler spectroscopy method. It relies on the star's orbital motion induced by planets' gravity. The projected velocity of the star along the observer's line-of-sight (the radial velocity) is measured from the displacement of the star's spectral lines due to the Doppler effect. In the case of a star with one planet, the radial velocity curve is a periodic function with semi-amplitude K given by

$$K = \left(\frac{2\pi G}{P}\right)^{\frac{1}{3}} \frac{M_p \sin i}{(M_* + M_p)^{\frac{2}{3}}} \frac{1}{\sqrt{1-e^2}} \tag{2.1}$$

where M_p and M_* are the mass of the planet and star respectively, G is the gravitational constant, i is the orbital inclination and e is the eccentricity. The eccentricity also affects the shape of the periodic signal (see Figure 2.2). The inclination, i, cannot be constrained with this method, but, assuming $M_p \ll M_*$ and an independent estimate for M_* (usually from spectroscopic

[1]Number taken from the online catalog exoplanet.eu (Schneider et al., 2011) on July 27, 2016.

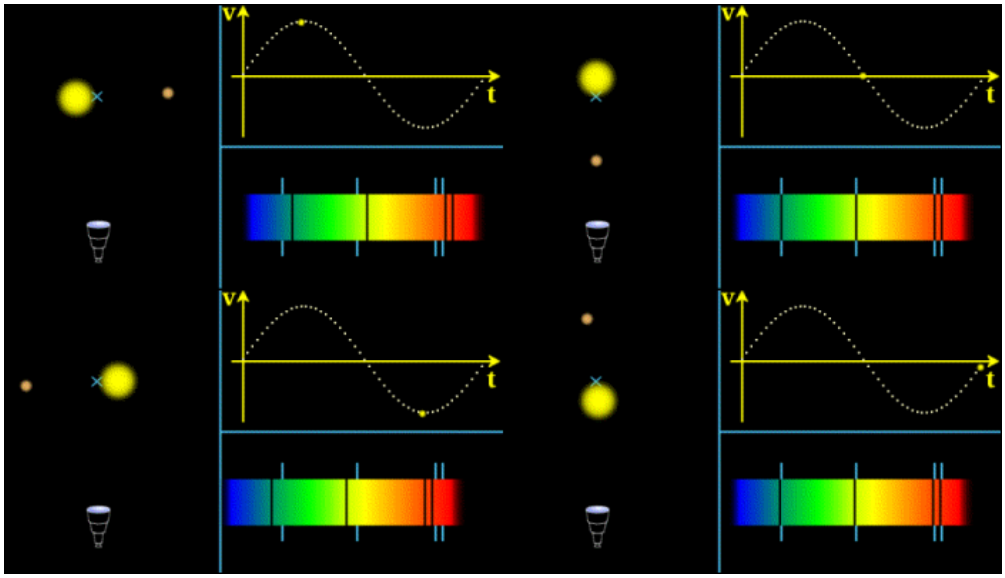

Figure 2.1: Doppler spectroscopy of the star's spectrum due to the gravitational wobble. Top left panel: redshifted spectrum due to the star moving away from the observer. Bottom left panel: blueshifted spectrum due to the star moving towards the observer. Right panels: no spectral shift, as the star's velocity is perpendicular to the observer's line-of-sight.

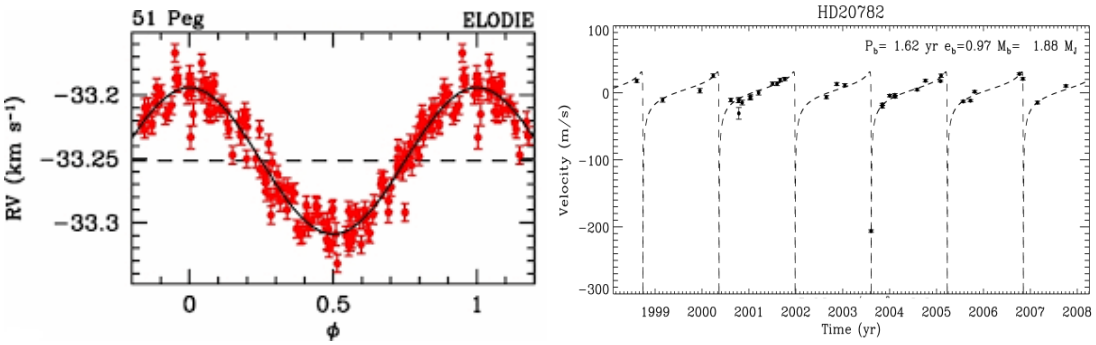

Figure 2.2: Radial velocity curves of the exoplanet host stars 51Peg (orbital eccentricity $e \approx 0$) and HD20782 (orbital eccentricity $e = 0.97$). Images from Mayor and Queloz (1995) and O'Toole et al. (2009).

observations and stellar models), it is possible to estimate the minimum mass of the planet as $M_p \sin i$. The orbital semi-major axis can be calculated using Kepler's third law.

Instrumental precision has significantly improved from the ∼20 m/s of the first discovery to the ∼1 m/s of the HARPS spectrograph on the 3.6 m telescope in La Silla, Chile (Mayor et al., 2003; Lovis et al., 2006), and HIRES on the 10 m Keck telescope in Mauna Kea, Hawaii (Howard et al., 2010), leading to the detection of less massive planets, down to 1.9 Earth masses (Mayor et al., 2009). Further technical improvements expected in future instruments such as CODEX (Pasquini et al., 2010) and ESPRESSO (Pepe et al., 2014) will push the accuracy down to ∼3–10 cm/s, allowing the detection of Earth-like planets .

2.1.2 Transits and eclipses

Some exoplanets are transiting, i.e., they pass between the host star and the observer for a portion of their orbit. Five years after the discovery of 51Peg b, the first observation of the transit of an exoplanet, HD209458 b, was announced almost simultaneously by two teams (Henry et al., 2000; Charbonneau et al., 2000). Transits were mainly observed after radial velocity detections, until the Kepler mission, launched in 2009, inverted this trend. With 2,624 transiting planets confirmed so far[2], and a similar number of candidate planets, the transit method is the one with the highest number of planet discoveries and/or follow up observations, surpassing Doppler spectroscopy since 2014. The next generation of transiting planet hunters, TESS (Ricker et al., 2014) and PLATO (Rauer et al., 2014), are expected to be launched in 2017 and 2024, respectively. A transit is detected through a drop in the stellar light-curve, as the star is partially obscured by the planet. Roughly modeling the star as a uniform emitting disc and the planet as a dark disc, the amplitude of the signal relative to the stellar flux equals the area ratio:

$$\frac{\Delta F}{F_*} \sim \frac{\pi R_p^2}{\pi R_*^2} \tag{2.2}$$

where R_p and R_* are the planetary and stellar radii, respectively. The transit duration is function of the orbital velocity and inclination. Having both transit and radial velocity measurements allows a complete determination of the orbital parameters, mass, size and mean density of the planet. I refer to Section 3.3 for details about the morphology of a transit light-curve and the parameter derivations.

If an atmosphere surrounds the planet, a fraction of the star's light will pass through the annulus created by the atmosphere. Part of this light can be absorbed by the chemical species present in the planet's atmosphere. Given that the absorption cross-section is a wavelength-dependent function for each species, the atmosphere is more or less transparent at different wavelengths, depending on the species which are present, on their quantities, and on the physical conditions (e.g., temperature and pressure). By accurately measuring the transit depths over multiple phometric bands, a "transmission spectrum" of the atmosphere is obtained, which can be used to infer some of the atmospheric properties, and in particular, to reveal the presence of atomic, ionic and molecular species.

Planetary eclipses are also observed when the planet is occulted by the star for a portion of the orbit; the first detection was reported almost simultaneously by Charbonneau et al. (2005) and Deming et al. (2005). During the eclipse, only the light emitted by the star reaches the

[2]Number taken from the online catalog exoplanet.eu (Schneider et al., 2011) on July 27, 2016.

observer, while before and after the eclipse there is also the contribution of the planet. As the surface brightness of the planet is (typically) fainter than the host star, the corresponding eclipse depth is smaller than the transit depth. A collection of eclipse depth measurements over multiple phometric bands is an "emission+reflection spectrum" of the planet, as it contains the thermal emission from the planet, which is typically higher in the IR, but also the stellar reflected light, higher in the optical and UV. Such emission+reflection spectra are mainly used to characterize the thermal profile of planets and to measure the albedo.

I refer to Section 2.2 for some historical highlights of exoplanet trasmission and emission spectroscopy.

2.1.3 Imaging

Conceptually the easiest approach to search for exoplanets, direct imaging turned out to be one of the hardest in practice, as exoplanets tend to be lost in the brilliant glare of their host stars. This happens because of the high contrast ratio between the two objects ($\gtrsim 10^4$) and the small angular separation. Coronagraphic and interferometric techniques are used to enhance the images of planets. To date, 69 planets in 64 systems, and 3 multiple systems, have been directly imaged[3]. A new generation of instruments such as the ground-based *Gemini*/GPI (Macintosh et al., 2006) and *VLT*/SPHERE (Beuzit et al., 2008) are providing high-quality images of planets over multiple photometric bands, which are used to detect the main chemical species in the atmospheres, the presence of clouds and hazes in the upper atmospheric layers, and to constrain the temperature and the surface gravity (e.g. Vigan et al., 2016; Maire et al., 2016; Zurlo et al., 2016; Bonnefoy et al., 2016). They are also expected to detect tens of new targets. The future space missions JWST (Gardner et al., 2006) and perhaps WFIRST (Content et al., 2011, 2013) will provide images of exoplanets at wavelengths not accessible from the ground.

Directly imaged planets are typically in larger orbits than the transiting ones (see Figure 2.4), hence they probe a different sample of the exoplanet population.

2.1.4 Microlensing

A microlensing event occurs when the gravitational field of an object deflects the light from a background star, magnifying it. In the case of star–star microlensing, the two stars must be almost perfectly aligned with the observer. The timescale of a microlensing event may range from days to weeks, as the two stars and Earth are all moving relative to each other. If the foreground star has a planet, it may cause a peak in the magnification (see Figure 2.3). A

[3]Numbers taken from the online catalog exoplanet.eu (Schneider et al., 2011) on July 27, 2016.

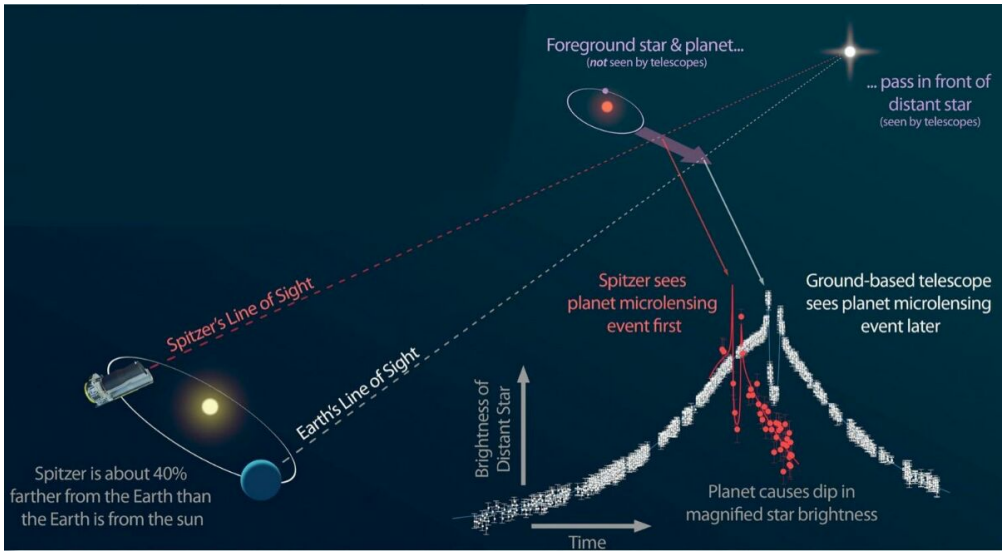

Figure 2.3: Microlensing signal observed from *Spitzer* and ground-based telescopes. Image credit: NASA/JPL-Caltech/Warsaw University (modified).

microlensing detection is more likely if the projected star–planet distance is between 1 and 4 AU (Bennett and Rhie, 1996). Microlensing is more sensitive to low-mass planets and to planets at larger distances from Earth than other detection methods, hence it may enable measuring the Galactic distribution of planets. However, the detection rate is low, i.e. 47 discoveries over 12 years[4], as microlensing events are rare and non-repeatable. Several ground-based surveys are constantly monitoring crowded areas in the Galactic disk searching for such events (OGLE, MOA, PLANET, LCOGT and KMTNet). The Spitzer Microlens Parallax program (Udalski et al., 2015; Calchi Novati et al., 2015) consists of simultaneous ground- and space-based observations from significantly different points of view, enabling distance estimates for each lens. Unfortunately, this method allows only a poor characterization of the planets themselves, as the only measurable parameters are its mass (broad estimate) and the projected star–planet separation at the moment of the event.

2.1.5 Timing

Pulsar timing was the method adopted to discover the first two exoplanets (Wolszczan and Frail, 1992). Similarly to the Doppler spectroscopy method, timing of pulsating variable stars is used to measure their radial velocities. This method is very sensitive to small planets around pulsars, for which the pulsation is extremely regular. However, with only 23 discoveries to date[4], astronomers believe that pulsar planets are rare (e.g. Kerr et al., 2015).

[4]Number taken from the online catalog exoplanet.eu (Schneider et al., 2011) on July 27, 2016.

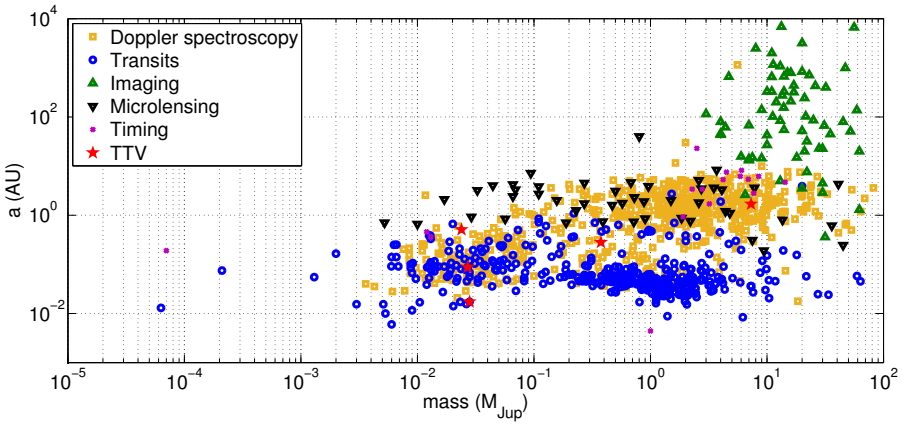

Figure 2.4: Mass vs semimajor axis of exoplanets detected with (yellow squares) Doppler spectroscopy, (blue circles) transits, (red upward triangles) direct imaging, (black downward triangles) microlensing, (purple crosses) timing and (red stars) transit timing variations. Data taken from exoplanet.eu on July 27, 2016.

2.1.6 Astrometry

Astrometry aims to measure directly the projected orbital motion of a star caused by its planet. Given the many intricacies with this method, we register only one unambiguous detection, i.e. HD176051 b (Muterspaugh et al., 2010). The GAIA mission (Gilmore et al., 2012), launched in December 2013, is expected to find every Jupiter-sized planet with an orbital period of 1.5–9 years within a distance of approximately 150 light-years from the Sun, totaling 10,000–50,000 new exoplanet discoveries (Perryman et al., 2014).

2.1.7 Transit/eclipse timing

If the orbit of a transiting exoplanet is strictly periodic, the intervals between consecutive transits or eclipses, as well as their durations, are constant over time. Slight deviations from perfect regularity may be caused by external perturbers, such as other planets (Holman and Murray, 2005) or moons (Kipping, 2009a,b), or by tidal or relativistic effects (Jordán and Bakos, 2008; Pál and Kocsis, 2008). Transit Timing Variations (TTVs) refer to the differences between the actual mid-transit points and their predicted times, according to an adopted periodic law. Transit Duration Variations (TDVs) refer to changes in the time interval between the beginning and the end of a transit event. Analogous quantities are defined for eclipses (ETVs and EDVs). Typical amplitudes for these signals are of the order of minutes or less, but the record is held by KOI 142.01 with ∼12 hour TTV amplitude (Nesvorny et al., 2013). So far, 7 confirmed exoplanets[5] have TTV measurements.

[5]Number taken from the online catalog exoplanet.eu (Schneider et al., 2011) on July 27, 2016.

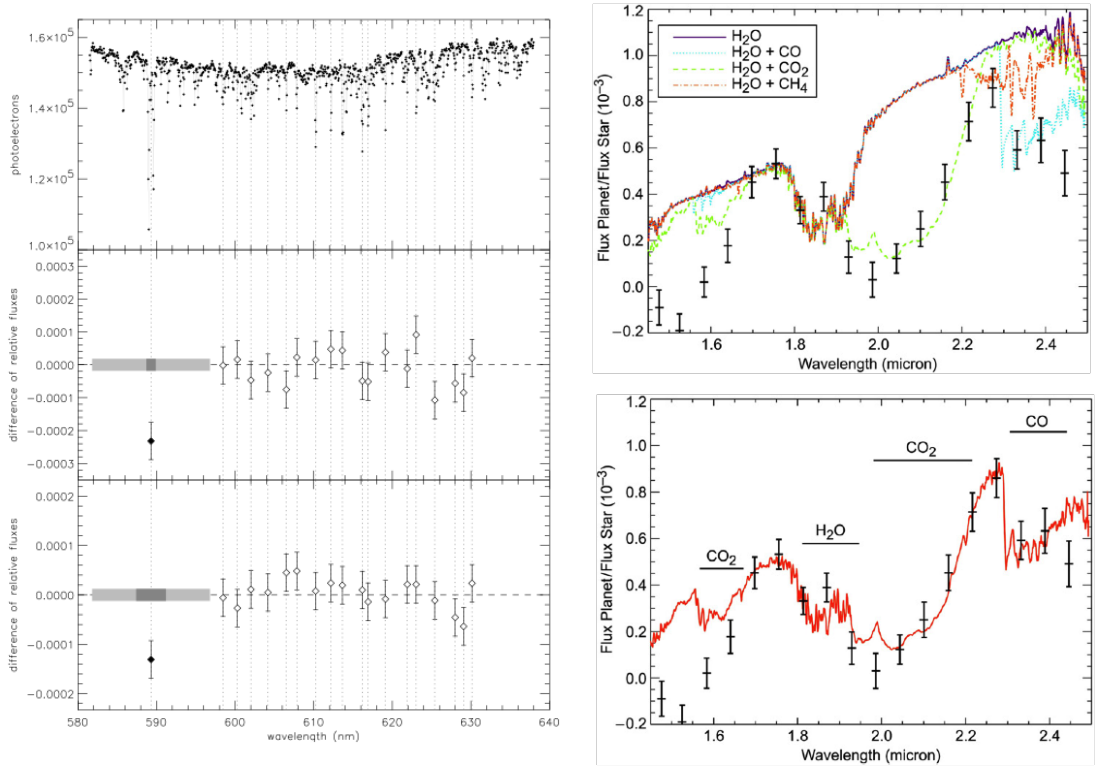

Figure 2.5: Left: (top) visible transmission spectrum of the exoplanet HD209458b, (middle) with a narrow bandpass, (bottom) with a medium bandpass. Image from Charbonneau et al. (2002). Right: near infrared emission spectrum of the exoplanet HD189733b compared with theoretical models (top) including H_2O only, H_2O + CO, H_2O + CO_2, H_2O + CH_4, and (bottom) H_2O + CO + CO_2 + CH_4. Images from Swain et al. (2009b).

2.2 Brief history of transit/eclipse spectroscopy

Charbonneau et al. (2002) reported the detection of atomic sodium in the atmosphere of the hot-Jupiter HD209458b, through the absorption feature in the region of the sodium resonance doublet at 589.3 nm observed with *HST*/STIS during the transit, relative to simultaneous observations in adjacent bands. This was the first detection of a chemical element in an exoplanetary atmosphere. In the following years, other atomic and ionic species have been detected in different exoplanets through their sharply peaked absorption features in the UV and visible, both from space- and ground-based telescopes, e.g. hydrogen Lyman-α (Vidal-Madjar et al., 2003; Lecavelier Des Etangs et al., 2010; Jensen et al., 2012), carbon II and oxygen I (Vidal-Madjar et al., 2004), magnesium II (Fossati et al., 2010), silicon III (Linsky et al., 2010), silicon IV (Schlawin et al., 2010) and potassium I (Sing et al., 2011a). Molecules are best detected through smooth infrared modulations over several microns, associated with their rovibrational transitions. Tinetti et al. (2007) announced the presence of water vapour in the atmosphere of the hot-Jupiter HD189733b based on the differential transit depths measured simultaneously with *Spitzer*/IRAC at 3.6 and 5.8 μm (Beaulieu et al., 2008), together with a previous measurement at 8.0 μm (Knutson et al.,

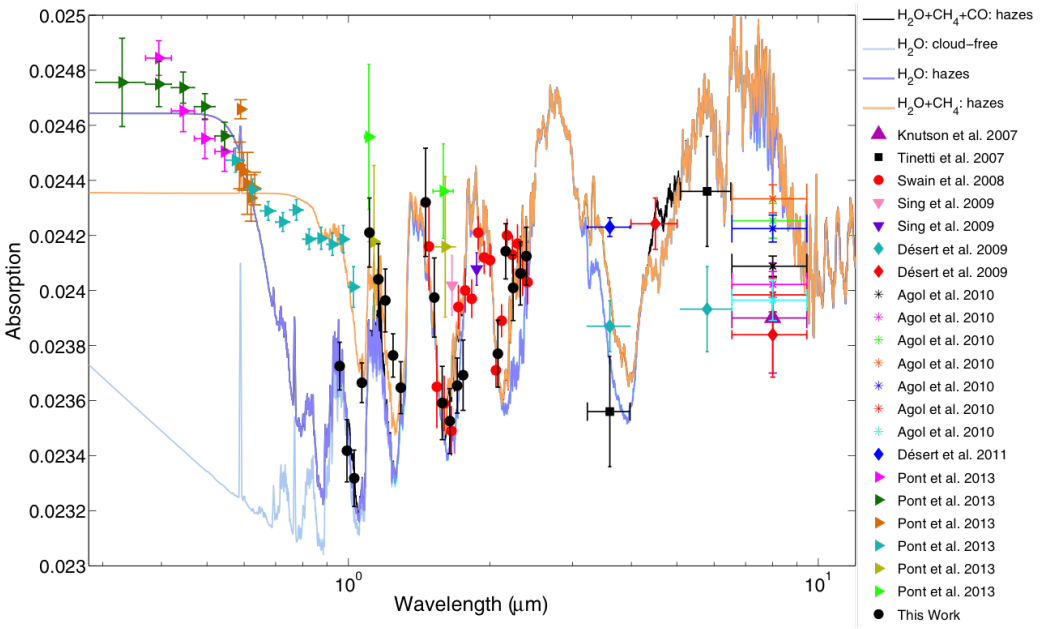

Figure 2.6: The transmission spectrum of the exoplanet HD189733b, combining measurements from different authors and comparing with some theoretical models. Image from Danielski et al. (2014).

2007a). Barman (2007) proposed water-vapour absorption to explain the modulation at $\sim$1 μm in the transmission spectrum of HD209458b measured with *HST*/STIS (Knutson et al., 2007b). The first exoplanetary emission spectra were reported by Richardson et al. (2007); Grillmair et al. (2007); Swain et al. (2008a), with no conclusive evidence of modulations. The presence of carbon molecules in the atmospheres has been inferred from IR transmission and emission spectra, e.g. methane (CH_4, Swain et al., 2008b; Agol et al., 2010; Tinetti et al., 2010), carbon dioxide (CO_2, Swain et al., 2009a) and carbon monoxide (CO, Swain et al., 2009b; Madhusudhan and Seager, 2009; Snellen et al., 2010). The first spectral measurements were limited to the brightest hot-Jupiters; now similar measurements are available for tens of exoplanets. Recently, the new *HST*/WFC3 camera allowed investigation of the atmospheres of super-Earths (Kreidberg et al., 2014; Knutson et al., 2014b; Tsiaras et al., 2016).

Despite these successes, some controversial results are debated in the literature. Here, I list three kinds of controversial result:

1. discrepant results from reanalyses of the same data sets using different parameterizations to detrending the instrument systematics;

2. variability between repeated observations of the same target, potentially due to the stellar activity or uncorrected instrument systematics;

3. difficulties in the interpretation of the spectra, e.g., because of model degeneracies, unex-

pected features, the presence of clouds, etc.

Examples of famous controversies in the previous literature relate to the presence of water and methane in the atmosphere of HD189733b (Ehrenreich et al., 2007; Tinetti et al., 2007; Beaulieu et al., 2008; Charbonneau et al., 2008; Grillmair et al., 2008; Swain et al., 2008b, 2009b, 2010; Pont et al., 2008, 2013; Désert et al., 2009, 2011; Sing et al., 2009, 2011b; Mandell et al., 2011; Waldmann et al., 2012, 2013; Danielski et al., 2014; Morello et al., 2014); the dominant carbon molecule in the atmosphere of HD209458b (Knutson et al., 2008; Beaulieu et al., 2010; Diamond-Lowe et al., 2014; Zellem et al., 2014; Evans et al., 2015); and of the warm-Neptune GJ436b (Gillon et al., 2007; Deming et al., 2007; Demory et al., 2007; Alonso et al., 2008; Coughlin et al., 2008; Cáceres et al., 2009; Pont et al., 2009; Ballard et al., 2010b; Stevenson et al., 2010; Beaulieu et al., 2011; Knutson et al., 2011, 2014a; Morello et al., 2015).

The main effort, in this Thesis, is to address the first two kinds of controversy by developing and using objective data detrending techniques, in order to obtain robust results for the transit and eclipse depth measurements.

Chapter 3

Transit/eclipse spectroscopy – technical details

3.1 The three-dimensional orbit

In this section, I introduce the parameters which are used to describe the orientation of an exoplanet orbit relative to the observer and the position of the planet. A representation is given in Figure 3.1. The nomenclature and the symbols introduced in this Section will be adopted throughout this Thesis.

I refer to the sky as the plane perpendicular to the line-of-sight to where the star lies. The two points where the planet's orbit crosses the sky are called nodes. In particular, the ascending node is where the planet is moving to the observer and the descending node is where the planet is moving away from the observer. To expedite the following explanations, I hereby anticipate that all angles defined in this section will have their vertex at the star's center. The longitude of the ascending node, Ω, is the angle between the ascending node and a reference line in the sky. The inclination, i, is the smaller of the two angles between the orbital plane and the sky ($0 \leq i \leq \pi/2$). The argument of periapsis, ω, is the angle, in the orbital plane, between the ascending node and the periapsis. The three angles, Ω, i and ω, are used to fully describe the orientation of the orbit.

The true anomaly, f, is the angular coordinate of the planet along the orbit, referred to the periapsis. Inferior conjunction is the instant when $f = \pi/2 - \omega$. Superior conjunction is the opposite point, i.e. when $f = 3\pi/2 - \omega$.

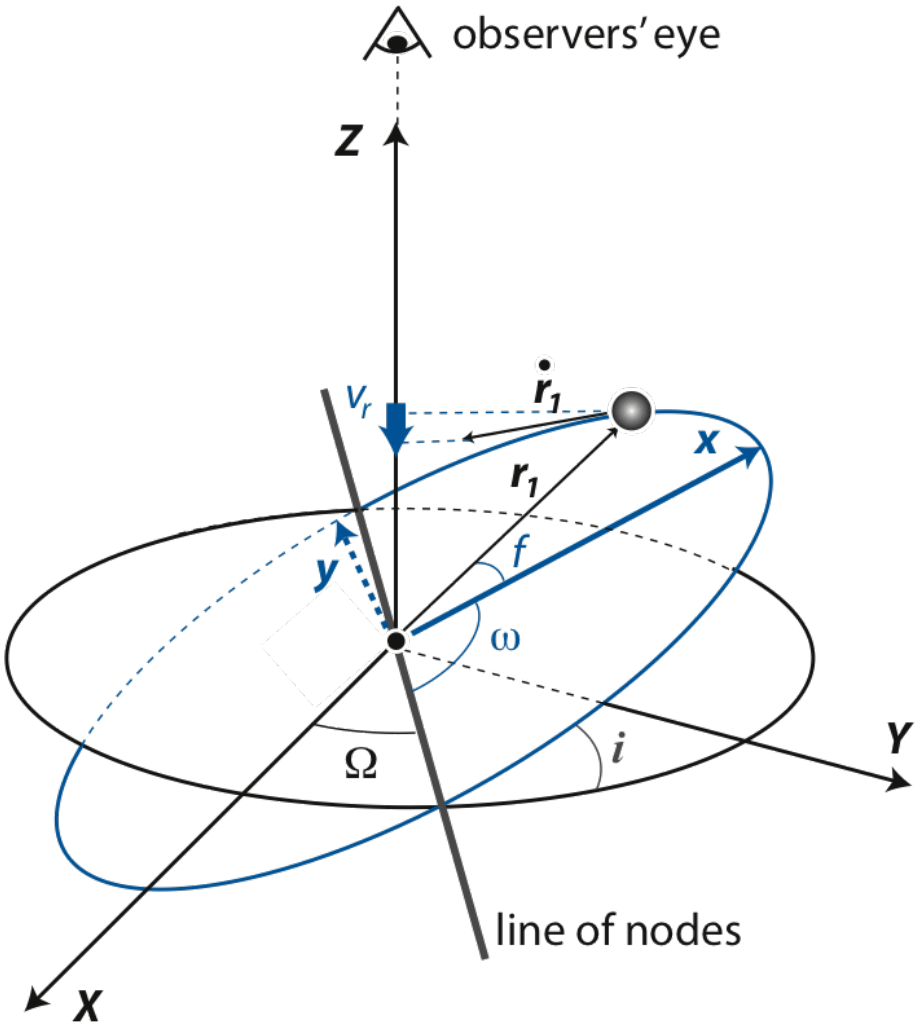

Figure 3.1: Orbital elements of an exoplanet orbiting a star. Figure from Murray and Correia (2011).

3.2 Geometric transit probability

The transit of an exoplanet in front of its host star is determined by the geometric orientation of the star–planet system relative to the observer. From the schematic representation in Figure 3.2, the following condition, for a transit to occur, can be derived for a point-like planet in a circular orbit:

$$\cos i \leq \frac{R_*}{a} \tag{3.1}$$

where a is the orbital radius, i is the inclination and R_* is the stellar radius. Using the knowledge that, for an isotropic distribution of planetary orbits, $\cos i$ is uniformly distributed between 0 and 1, we note that R_*/a is the geometric transit probability for a system with given R_* and a. The bottom panel in Figure 3.2 shows the transit probability as a function of the orbital radius for a Sun-sized star.

A general formula for the transit probability of a planet in an eccentric orbit is (Winn, 2014; Kipping, 2014)

$$p(transit|R_*, a, e) = \frac{R_*}{a}\frac{1}{1-e^2} \tag{3.2}$$

being e the eccentricity.

If R_p is the planet's radius, we can replace R_* in Equations 3.1 and 3.2 with $R_* + R_\mathrm{p}$ to account for all transits, no matter how grazing, or with $R_* - R_\mathrm{p}$ to account only for the full transits.

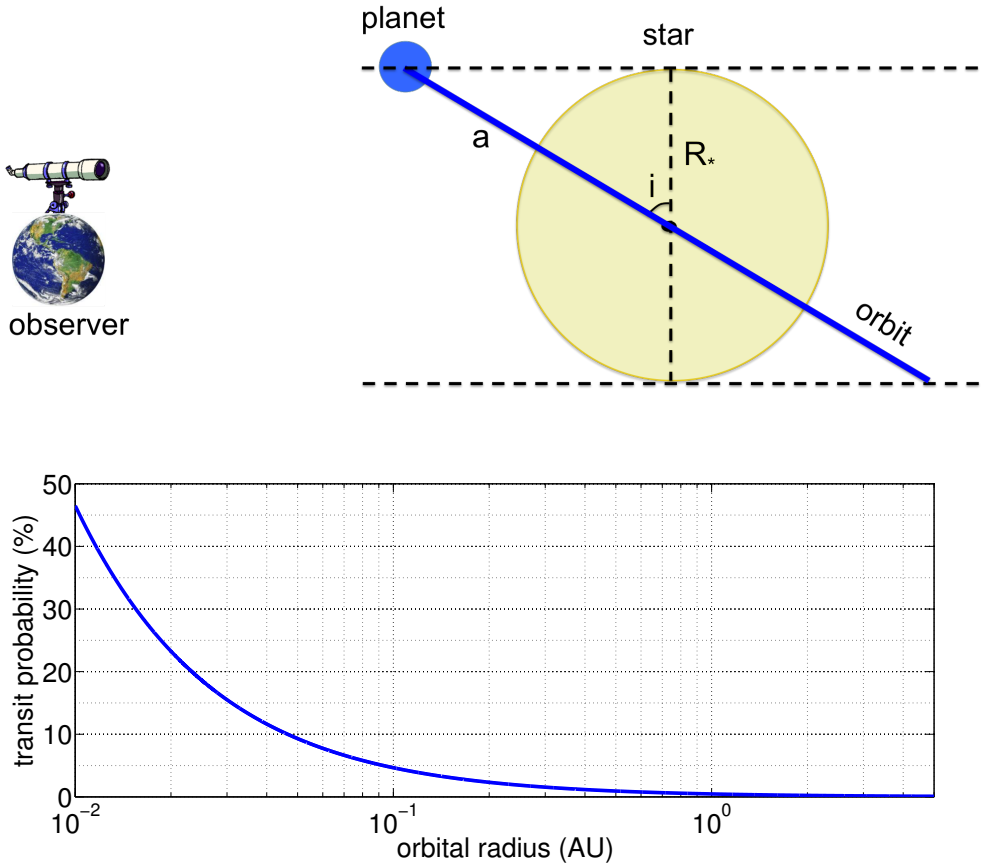

Figure 3.2: Top panel: bidimensional scheme of a star-planet system and observer, showing the limiting condition to have a transit. Bottom panel: geometric transit probability as a function of the orbital radius for a Sun-sized star.

Note that the probability of observing a transit for a planet in a Mercury's orbit ($a = 0.387$ AU) is already as low as 1.2%. This suggests that a hypothetical Solar System twin would be unlikely to be detectable with transits. Even in the case of an extremely lucky alignment, another challenge would be represented by the low frequencies of transits for the external planets, i.e. once every 12, 29, 84 and 165 years for Jupiter, Saturn, Uranus and Neptune, respectively. The success of exoplanet transit surveys is due to the existence of many different systems with planets in smaller orbits and periods from fractions to tens of days.

3.3 The transit light-curve morphology

3.3.1 The fundamental model

In a full transit, the sky-projected stellar and planetary disks are tangent at four contact times $t_{\rm I}$–$t_{\rm IV}$, illustrated in Figure 3.3. The external contacts, $t_{\rm I}$ and $t_{\rm IV}$, delimit the total transit event, i.e. when the star is partially occulted by the planet. The internal contacts, $t_{\rm II}$ and $t_{\rm III}$, delimit the full part of the transit, i.e. when the planet's disk lies entirely inside the star's disk. In a grazing transit, the planet's disk never lies entirely inside the star's disk, then $t_{\rm I}$ and $t_{\rm IV}$ are the only contact points. The two intervals, $t_{\rm I}$–$t_{\rm II}$ and $t_{\rm III}$–$t_{\rm IV}$, during which the planet's disk intersects the edge of the star's disk are called ingress and egress, respectively.

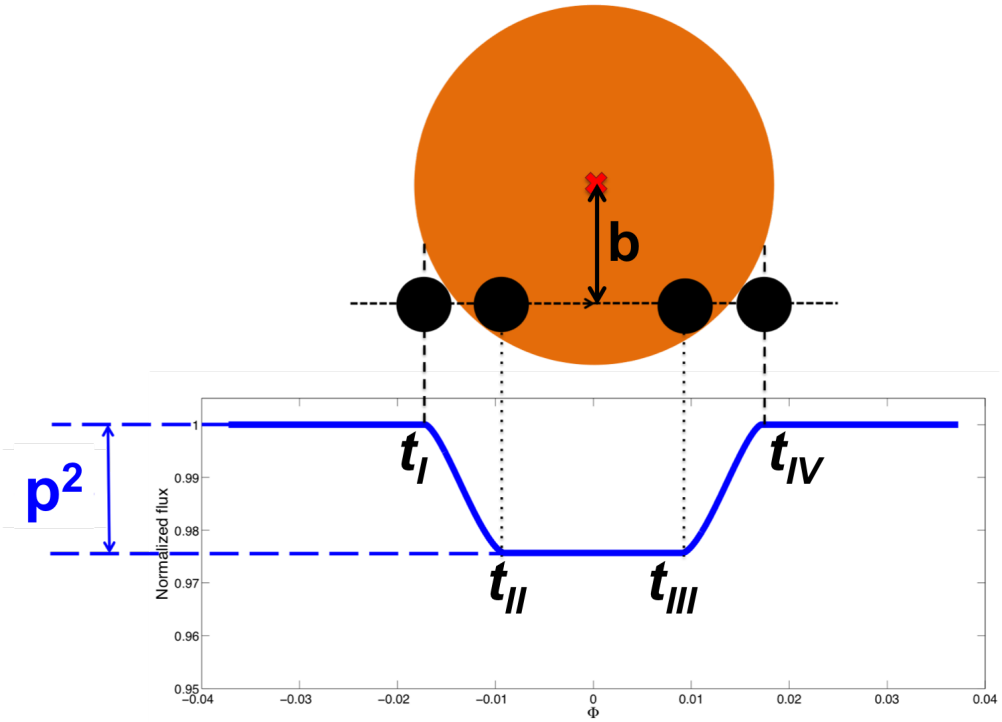

Figure 3.3: Rationale of the transit light-curve. The top part represents the (approximately linear) projected path of the planet in proximity of the transit event and the four contact points (labelled below) in particular. The bottom part shows the corresponding light-curve in the ideal case of uniformly emitting, constant star's disk and totally opaque, dark planet.

In an ideal case, where the surface brightness of the stellar disk is uniform, and the planet is dark, totally opaque and in a circular orbit, the following observables can be measured:

- the transit depth,

$$\delta_{\rm tr} = \frac{F_{\rm out} - F_{\rm in}}{F_{\rm out}} = \left(\frac{R_{\rm p}}{R_*}\right)^2 , \tag{3.3}$$

  where $F_{\rm out}$ is the measured flux before $t_{\rm I}$ and after $t_{\rm IV}$, i.e. the unperturbed stellar flux ($F_{\rm out} = F_*$), $F_{\rm in}$ is the constant flux in the interval between $t_{\rm II}$ and $t_{\rm III}$.

- the total transit duration,

$$T_{\rm tot} = t_{\rm IV} - t_{\rm I} = \frac{P}{\pi} \arcsin \left(\frac{\sqrt{\left(1 + \frac{R_{\rm p}}{R_*}\right)^2 - \left(\frac{a}{R_*}\right)^2 \cos^2 i}}{\frac{a}{R_*} \sin i} \right), \tag{3.4}$$

  where P is the orbital period.

- the full transit duration,

$$T_{\rm full} = t_{\rm III} - t_{\rm II} = \frac{P}{\pi} \arcsin \left(\frac{\sqrt{\left(1 - \frac{R_{\rm p}}{R_*}\right)^2 - \left(\frac{a}{R_*}\right)^2 \cos^2 i}}{\frac{a}{R_*} \sin i} \right). \tag{3.5}$$

Given the assumption of a circular orbit, the light-curve is symmetric with respect to the mid-transit point, defined as the instant of inferior conjunction (see Section 3.1), which is, in this case, halfway between the two external or the two internal contact points. The ingress and egress times are both equal to $(T_{\rm tot} - T_{\rm full})/2$, hence they do not add useful information. If the orbital period is known, e.g. from radial velocity measurements or consecutive transit observations, the set of Equations 3.3–3.5 can be inverted to estimate the following parameters (Seager and Mallén-Ornelas, 2003):

- the planet's radius in units of the stellar radius,

$$p = \frac{R_{\rm p}}{R_*} = \sqrt{\delta_{\rm tr}} \tag{3.6}$$

- the impact parameter, b, defined as the sky-projected planet–star separation in units of the stellar radius at the instant of inferior conjunction,

$$b = \frac{a}{R_*} \cos i = \left[\frac{(1-p)^2 - \frac{\sin^2\left(\frac{\pi T_{\rm full}}{P}\right)}{\sin^2\left(\frac{\pi T_{\rm tot}}{P}\right)} (1+p)^2}{1 - \frac{\sin^2\left(\frac{\pi T_{\rm full}}{P}\right)}{\sin^2\left(\frac{\pi T_{\rm tot}}{P}\right)}} \right]^{\frac{1}{2}} \tag{3.7}$$

- the orbital semi-major axis in units of the stellar radius,

$$a_R = \frac{a}{R_*} = \left[\frac{(1+p)^2 - b^2\left(1 - \sin^2\left(\frac{\pi T_{\rm tot}}{P}\right)\right)}{\sin^2\left(\frac{\pi T_{\rm tot}}{P}\right)} \right]^{\frac{1}{2}} \tag{3.8}$$

- the orbital inclination,

$$i = \arccos\left(\frac{b}{a_R}\right) \tag{3.9}$$

An independent estimate of the stellar radius, usually obtained from spectroscopic observations and stellar models, is needed to determine the absolute sizes of the planet's radius and semi-major axis.

3.3.2 Eccentric orbits

The main effect of a non-zero orbital eccentricity is to break the system symmetry. In general, the mid-transit point (conjunction), the central point of the total transit, $(t_{\rm I} + t_{\rm IV})/2$, and the central point of the full transit, $(t_{\rm II} + t_{\rm III})/2$, are three distinct instants. The exact shape of the light-curve, normalized to the out-of-transit flux, is uniquely determined by 6 parameters: p, a_R, i, e, ω and t_{mid}. The definitions of the first three parameters are identical to the case of a circular orbit; in particular, $p = R_{\rm p}/R_*$, $a_R = a/R_*$, and i is the angle between the orbital plane and the sky. The new parameters are the orbital eccentricity, e; the argument of periapsis, ω; and the mid-transit time, t_{mid} (see Section 3.1).

The inverse problem, i.e. determining the 6 parameters above from the light-curve, is virtually impossible for a number of reasons:

- there are only 4 independent observables, i.e. the transit depth and 3 interval durations between contact points, to determine 6 parameters;
- there are (not simple) analytic expressions for the durations (Kipping, 2008);
- different sets of parameters may generate very similar light-curves, that cannot be distinguished with the precision of current instruments.

Even if e and ω are known, e.g. from radial velocity measurements, Equations 3.4–3.5 and 3.7–3.9 cannot be used for $e > 0$. I refer to Kipping (2010) for an approximate solution to the problem of the 'eccentric fundamental model' and a critical comparison of several approximate formulas adopted in the literature. The approach adopted in this Thesis is different, as it does not use a set of observables to derive the physical and orbital parameters (see Section 3.3.4), for reasons that will be clear from the next Section (3.3.3).

3.3.3 Stellar limb darkening

In a real situation the stellar disk is not uniform, because of the thermal stratification of the star's atmosphere and the effect of optical depth. In particular, the radiation reaching us from the center of the disk includes the contributions from deeper layers than the radiation reaching us from the limb, and there being a negative gradient of temperature vs radius of the star from the center to the surface, the center of the disk appears brighter than the limb. This is the

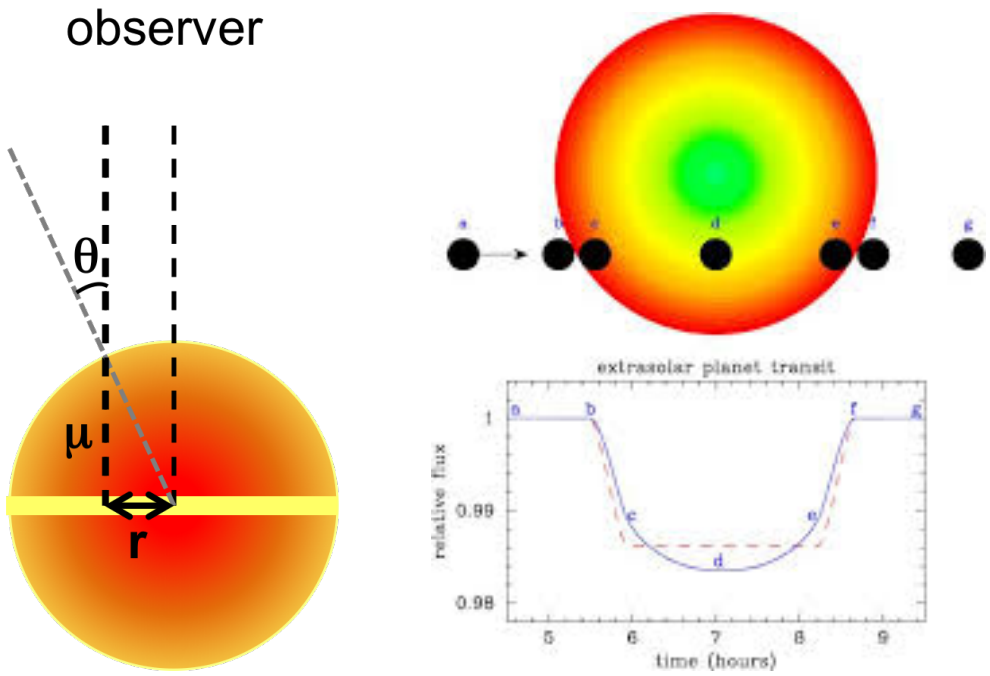

Figure 3.4: Left panel: geometry of the stellar limb darkening. The section of the sky-projected stellar disk is yellow, θ is the angle between the line-of-sight and the perpendicular to the stellar surface, $\mu = \cos\theta$, $r = \sqrt{1-\mu^2}$ is the radial coordinate. Right panel: representation of a limb darkened transit.

so called "limb darkening" effect. The main consequence for the transit light-curve is that the flux is not constant between the contact points $t_{\rm II}$ and $t_{\rm III}$, as the decrement in flux depends on which part of the stellar disk is occulted by the planet.

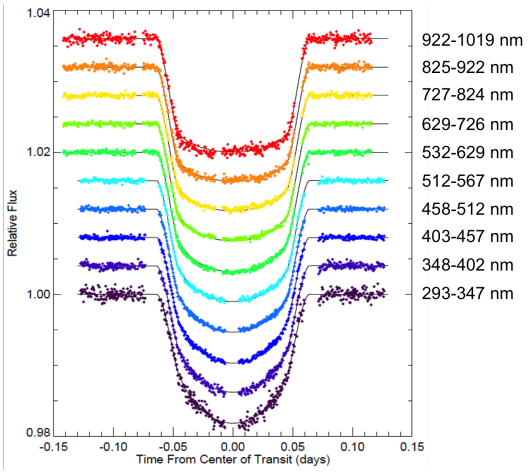

Figure 3.5: Transit shapes of HD209458b at different wavelengths. Image adapted from Knutson et al. (2007b).

The resulting limb-darkened light-curve strongly deviates from the approximately trapezoidal shape towards a U-shape, particularly in the UV and visible (see Figure 3.5). The U-shape makes it hard, if not impossible, to identify the internal contact points, and hence the duration $T_{\rm full}$. No matter how we re-define the transit depth for the limb-darkened case, the information about the size of the planet relative to the star is coupled with the intensity distribution over the stellar disk.

Determining the unknown physical and orbital parameters through some basic observables of the transit light-curve, as illustrated for the fundamental model in Section 3.3.1, is, at best, impractical in real cases. Instead, the standard approach is to compare the observed light-curve

with a parameterized model: best estimates for the unknown parameter values are obtained by minimizing the residuals between the observation and the model (typically in the least-squares sense).

3.3.4 Transit light-curve models

In the work presented in this Thesis, I made the following assumptions when modeling a transit light-curve, unless otherwise specified:

1. the planet's disk is circular, totally opaque and dark, i.e. its only effect is to block the light from the geometrically occulted part of the stellar disk;
2. the star's disk is limb-darkened, symmetric with respect to its center;
3. the unit of length is the stellar radius, i.e. $R_* = 1$.

With these assumptions, the observed flux at a given instant is a function of the planet's radius, p, and the sky-projected star–planet separation at the given instant, z.

If $I(r)$ is the intensity emitted by the stellar disk at a radial coordinate r (such that $r = 0$ at the center and $r = 1$ at the limb), the instantaneous flux, in units of stellar flux, is given by:

$$F(p, z) = 1 - \Lambda(p, z) \tag{3.10}$$

with

$$\Lambda(p, z) = \left[\int_0^1 I(r)\ 2\pi r\, dr\right]^{-1} \int_0^1 I(r)\ 2\pi r\ f_{p,z}(r)\, dr \tag{3.11}$$

The first integral in Equation 3.11 gives the unperturbed stellar flux, F_*, and acts as a normalization factor. The second integral differs for the term $f_{p,z}(r)$, which is the fraction of the circumference with radius r covered by the planet's disk:

$$f_{p,z}(r) = \left\{ \begin{array}{ll} \frac{1}{\pi} \arccos \frac{r^2+z^2-p^2}{2zr} & |z-p| < r < z+p \\ 0 & r \leq z-p \ or \ r \geq z+p \\ 1 & r \leq p-z \end{array} \right|_{0 \leq r \leq 1} \tag{3.12}$$

Several functional forms have been proposed in the literature to approximate the intensity profile of the stellar disk (e.g. Howarth, 2011a for a review). The two most popular ones in the field of transiting exoplanets are:

- the quadratic law

$$I_\lambda(\mu) = I_\lambda(1)[1 - \gamma_1(1-\mu) - \gamma_2(1-\mu)^2]; \tag{3.13}$$

- the Claret's four-coefficients law (Claret, 2000)

$$I_\lambda(\mu) = I_\lambda(1)\left[1 - \sum_{n=1}^{4} c_n \left(1 - \mu^{\frac{n}{2}}\right)\right] \tag{3.14}$$

where $\mu = \cos\theta = \sqrt{1-r^2}$, being θ the angle of incidence (see Figure 3.4). Mandel and Agol (2002) calculated analytical solutions for the integral in Equation 3.11 with $I(r)$ expressed according to Equations 3.13 and 3.14, providing a fast code for the quadratic case, which I adopted. Recently, my colleague Angelos Tsiaras provided our group with a similarly fast code for the four-coefficients law (https://github.com/ucl-exoplanets/pylightcurve), which I adopted in my latest work. I computed ad hoc stellar limb darkening coefficients for each target analyzed, to replace in Equation 3.13 or 3.14, by using the modified version of the ATLAS9 code presented in Howarth (2011b), and, in some cases, from models obtained with the PHOENIX Web Simulator (Allard and Hauschildt, 1995; Allard et al., 2001).

The instantaneous star–planet separation, z, is determined by the orbital parameters a_R, i, e, ω, and the time of inferior conjunction, t_{mid}. Because of the orbital periodicity, it is possible to define Φ, i.e. a sort of normalized time, also called "phase", so that each position of the planet in its orbit is associated to a value of Φ. Conventions in transit studies are:

- $\Phi(t_{mid}) = 0$;
- Φ values are in the range $[-0.5,\ 0.5]$.

The "angular phase" is defined as:

$$\Theta = 2\pi\Phi \tag{3.15}$$

In the case of circular orbit:

$$z = a_R\sqrt{1 - \cos^2\Theta \sin^2 i} \tag{3.16}$$

For an eccentric orbit, z is obtained through the following steps:

1. Calculate the mean anomaly

$$M = \left(\frac{\pi}{2} - \omega\right) + \Theta \tag{3.17}$$

2. Solve the Kepler's Equation for the eccentric anomaly (E)

$$M = E - e\sin E \tag{3.18}$$

3. Calculate the true anomaly

$$f = 2 \arctan\left(\sqrt{\frac{1+e}{1-e}} \tan\frac{E}{2}\right) \tag{3.19}$$

4. Then the sky-projected star-planet separation is given by

$$z = \frac{a_R(1-e^2)}{1+e\cos f}\sqrt{1-\sin^2(f+\omega)\sin^2 i} \tag{3.20}$$

3.3.5 Transit parameter fitting

In the previous Section 3.3.4, I explained how a light-curve model is calculated if the parameters p, a_R, i, e, ω, P, t_{mid} and the stellar limb darkening coefficients are given.

For the targets that I analyzed in this Thesis, the orbital period, P, and the so-called "Epoch of Transit", E.T., i.e. the mid-transit point of a reference transit, are reported in the literature with high accuracy, as many transits have been observed, and also radial velocity measurements have been taken. I use them to transform time into phase:

$$\Phi = \frac{t - E.T.}{P} - n \tag{3.21}$$

where n is an integer number, corresponding to the number of periods elapsed from the Epoch of Transit (rounded to the nearest integer).

I also assume the eccentricity, e, and the argument of periapsis, ω, reported in the literature, typically obtained with radial velocity measurements.

For the limb darkening coefficients, I take the basic stellar parameters from the literature, in particular the effective temperature, T_{eff}, surface gravity, $\log g$, and metallicity, $[M/H]$, which are sufficient to generate a complete stellar model, with some typical assumptions about the specific chemical abundances, with ATLAS9 or the PHOENIX Web Simulator (Allard and Homeier, 2014), as discussed in Section 3.3.4. An optional output of the stellar models is a grid of intensities at multiple angles of incidence, in order to fit a limb darkening law (Equations 3.13 and 3.14).

I often find discrepant values for a_R and i in the literature, hence I fit for them, rather than assuming their values. Also, most of the targets show potential TTVs of up to tens of seconds, hence I include t_{mid} as free parameter in the fits.

The other fitting parameters are p, which is the diagnostic parameter for the atmospheric studies, a normalization factor for the flux (as models and observations are not in the same units), and other coefficients related to the instrument systematics which are present in observations.

Details about the correction of instrument systematics and some experiments with different sets of fitting parameters are described for specific cases in the following Chapters.

Here I describe the general fitting algorithm that I adopted in this Thesis.
First, I use a Nelder-Mead optimization algorithm (Lagarias et al., 1998) to obtain point estimates of the parameters which minimize the sum of squared residuals between the real light-curve and the model. Then, I assume uninformative priors for the same parameters, i.e. typically uniform prior over a wide range, and run an Adaptive Metropolis algorithm with delayed rejection (Haario et al., 2006), starting from the point estimates, in order to sample the posterior probability distributions of the fitting parameters. The likelihood function is the standard $e^{-\chi^2}$, where χ^2 is originally set as the variance of the residuals, then sampled together with the other parameters. Mean values and standard deviations of the sampled chains are used to estimate the best parameter values and error bars, being the posterior distributions approximately gaussian. The error bars are re-scaled to include the potential uncertainties related with the method adopted to detrend the instrument systematics, as it will be discussed for the specific cases in the following Chapters.

3.4 The eclipse light-curve morphology

The morphology of the planetary eclipse light-curve is analogous to the idealized transit model with four contact points, $t'_{\rm I}$–$t'_{\rm IV}$, corresponding to the instants at which the sky-projected star's and planet's disks are tangent.

3.4.1 Eclipse light-curve models

In the case of a circular orbit, the eclipses occur half-way between consecutive transits, i.e. at phase $\Phi = 0.5$. In general, the eclipse phasing depends on the orbital eccentrity and the argument of periapsis. Conventionally, in eclipse studies, the Φ values are in the range $[0,\ 1]$. Stellar limb darkening has no effect, because the star is not occulted during the eclipse. Therefore, the flux observed between the internal contact points, $t'_{\rm II}$ and $t'_{\rm III}$, is the stellar flux, which is usually constant within the eclipse timescale. If the planet is dark, no flux variations are observed during the eclipse. If the planet emits a flux F_p, uniformly distributed over its surface, the instantaneous flux, in units of stellar flux, is given by:

$$F(p,z) = 1 + \frac{F_p}{F_*}\left(1 - \frac{\Lambda(p,z)}{p^2}\right) \tag{3.22}$$

where $\Lambda(p, z)$ is the same as in Equation 3.11 with a constant $I(r)$, as there is no limb darkening. The assumptions of dark planet for the case of transit and non-dark for the eclipse are not contradictory. In fact, during the transit the planet shows its night-side to the observer, i.e. the part not irradiated by the star, while before and after the eclipse it shows its day-side, i.e. the part irradiated by the star, which is typically brighter than the respective night-side (Showman et al., 2008a,b, 2009; Knutson et al., 2009). In general, the brightness of the planet is a function of the orbital phase; the observed star+planet flux during one orbit is called "phase-curve" (Langton and Laughlin, 2008; Showman et al., 2009; Cowan and Agol, 2011; Kataria et al., 2013). Figure 3.6 shows an example of exoplanetary phase-curve.

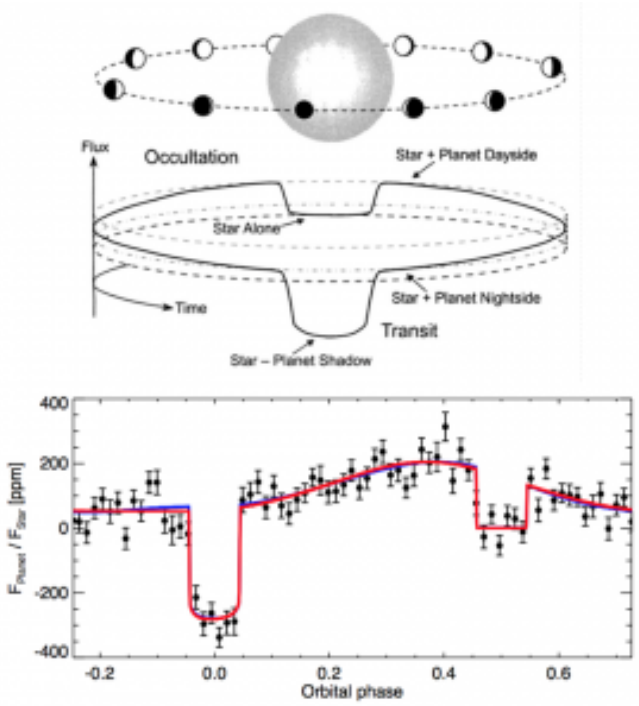

Figure 3.6: Top panel: illustration of the phase-curve of an exoplanet transiting its host star. Image from Winn (2014). Bottom panel: phase-curve of the exoplanet 55 Cnc e observed with *Spitzer*/IRAC at 4.5 μm. Image from Demory et al. (2016).

In this Thesis, I approximate the planet's phase-curve in the region of the eclipse as a linear function of the time, the slope is called "phase constant", adopting the same terminology found in the relevant literature. The slope is only due to planet's flux variations. While the planet is completely occulted by the star, the flux is constantly 1. The eclipse depth is defined as the (unseen) planet's flux at the mid-eclipse point, i.e. superior conjunction, in units of stellar flux.

Figure 3.7 shows the generic transit and eclipse models adopted in this Thesis. The use of a more complex model for the eclipse is motivated by the following points:

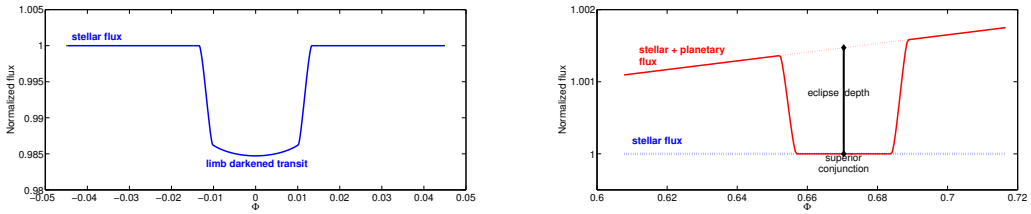

Figure 3.7: Left panel: generic transit model adopted in this Thesis (see Section 3.3.4). Right panel: generic eclipse model adopted in this Thesis (see Section 3.4.1).

1. the higher planetary brightness in proximity of the eclipses than transits;

2. the possibility to measure directly the unperturbed stellar flux during the eclipse;

3. the higher eccentricity of the specific planet analysed, which may cause a higher phase-curve slope in proximity of the eclipse event, according to models.

3.4.2 Eclipse parameter fitting

As for the analysis of transits, the first step is to transform time into phase by using Equation 3.21. I assume the parameters p, a_R, i, e, ω and P from the literature, as they are loosely constrained by the eclipse alone and the eclipse depth is independent on these parameters. The three fitting parameters are the eclipse depth, the mid-eclipse point and the phase constant (see Section 3.4.1).

3.5 Spectroscopy of transiting exoplanets

3.5.1 Atmospheric transmission spectra

The transit depth is a measure of the optically thick radius of an exoplanet, which is a wavelength-dependent function. In fact, planets are typically surrounded by an atmosphere, i.e. a gaseous envelope that can be more or less transparent to the stellar radiation at different wavelengths, depending on the absorption from the chemical species present in the atmosphere. While the distinction between the solid/liquid core and the gaseous atmosphere is conceptually clear for the rocky planets, the atmosphere of a gaseous planet can be thought of as the part which is not totally opaque at all wavelengths. Figure 3.8 illustrates the stellar light filtered through an exoplanet's atmosphere. According to Beer-Lambert's law, the observed intensity at a geometric atmospheric height z is

$$I_\lambda(z) = I_\lambda(0)e^{-\tau_\lambda(z)}, \tag{3.23}$$

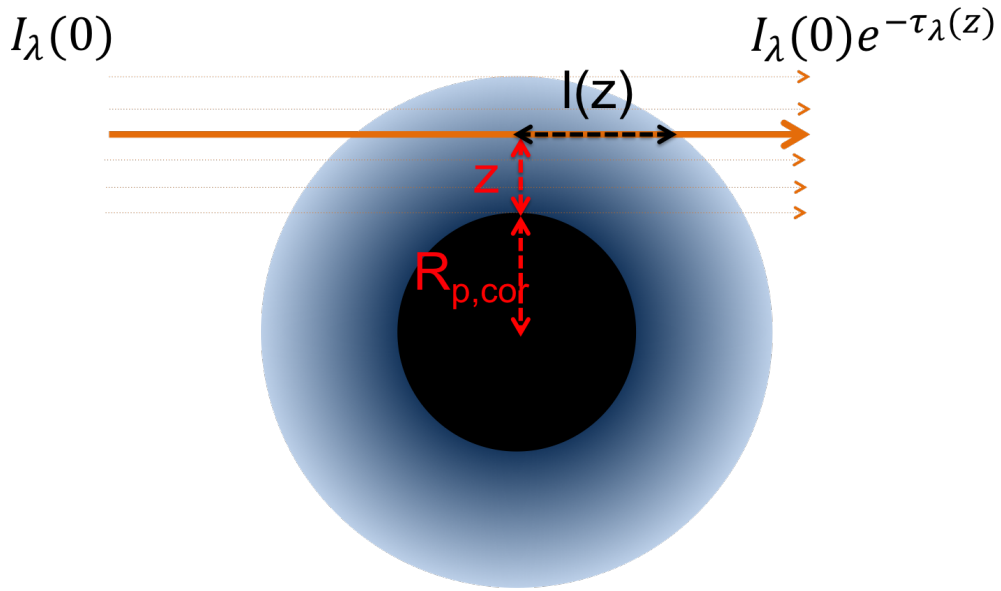

Figure 3.8: Stellar light filtered through an exoplanet's atmosphere.

where $I_\lambda(0)$ is the incident stellar intensity and $\tau_\lambda(z)$ is the optical depth of the atmosphere at height z and wavelength λ. The total optical depth is the sum of the optical depths due to different absorbing species:

$$\tau_\lambda(z) = \sum_i \tau_{\lambda,i}(z) \tag{3.24}$$

$$\tau_{\lambda,i}(z) = 2\int_0^{l(z)} \zeta_i(\lambda)\chi_i(z)\rho_N(z)dl. \tag{3.25}$$

Here, $l(z)$ is half the geometric path through the atmosphere at height z, $\zeta_i(\lambda)$ is the absorption cross-section of the species denoted with the index i at wavelength λ, $\chi_i(z)$ is the relevant column density and $\rho_N(z)$ is the total number density. The resulting transit depth is

$$p^2(\lambda) = \frac{R_{\rm p,cor}^2 + \int_0^{z_{max}} 2\left(R_{\rm p,cor}+z\right)\left(1-e^{\tau_\lambda(z)}\right)dz}{R_*^2} \tag{3.26}$$

3.5.2 Atmospheric emission+reflection spectra

The eclipse depth is a direct measure of the planet's flux relative to the stellar flux, before and after eclipse. In general, the planetary flux is a function of the orbital phase. The collection of eclipse depths over multiple bandpasses is called an "emission+reflection spectrum". The two main contributions to the planet's flux are the stellar reflected light, normally dominating in the visible and UV, and the intrinsic thermal emission, normally dominating in the infrared.

Examples of codes to generate models of exoplanet spectra and the inverse atmospheric retrieval are reported in Terrile et al. (2008); Madhusudhan and Seager (2009); Lee et al. (2012);

Benneke and Seager (2012); Line et al. (2012); Barstow et al. (2013); Griffith (2014); Waldmann et al. (2015b,a).

Chapter 4

Independent Component Analysis

"We all see only that which we are trained to see."

— **R. A. Wilson - Masks of the Illuminati**

4.1 The "Cocktail Party Problem"

Imagine a room where n people are speaking simultaneosly, as happens in cocktail parties. Each person emits a speech signal, here denoted by $s_j(t)$, j being an integer index running from 1 to n. Suppose also that m microphones are placed in the room recording the received signals. Each recorded signal $x_i(t)$, with i integer between 1 and m, is a weighted sum of the speech signals:

$$x_i(t) = \sum_{j=1}^{n} a_{ij} s_j(t) \tag{4.1}$$

where the a_{ij} are called mixing coefficients, and depend on the distances of the microphones from the speakers (Hyvärinen and Oja, 2000).

Is it possible to extract the original speech signals from only the recorded signals? If the mixing coefficients are known, it becomes a simple algebraic question, that is, if a system of m linear equations with n unknowns is solvable:

$$\begin{cases} x_1(t) = a_{11}s_1(t) + a_{12}s_2(t) + ... + a_{1n}s_n(t) \\ x_2(t) = a_{21}s_1(t) + a_{22}s_2(t) + ... + a_{2n}s_n(t) \\ \vdots \\ x_m(t) = a_{m1}s_1(t) + a_{m2}s_2(t) + ... + a_{mn}s_n(t). \end{cases} \tag{4.2}$$

The system is solvable when the number of independent equations is equal to the number of

unknowns ($m = n$). If $m > n$ it is solvable, in principle, using just a subset of n independent equations. A more compact notation for Equation 4.2 is:

$$\mathbf{x} = \mathbf{A}\mathbf{s} \tag{4.3}$$

where, $\mathbf{x}$ and $\mathbf{s}$ are the column vectors of the observed and source signals respectively, and $\mathbf{A}$ is the matrix of the mixing coefficients, also called mixing matrix. If $m = n$, $\mathbf{A}$ is a squared invertible matrix, so the source signals are given by:

$$\mathbf{s} = \mathbf{A}^{-1}\mathbf{x} = \mathbf{W}\mathbf{x} \tag{4.4}$$

The problem arises when neither the matrix $\mathbf{A}$ nor the source signals $\mathbf{s}$ are known. This is the classic "Cocktail Party Problem". This type of problem is found in several applications, for different kinds of signals involved, such as separation of artifacts in magneto-encephalography (e.g. Vigário et al., 1998), reducing noise in natural images (e.g. Bell and Sejnowski, 1997), finding hidden factors in financial data (e.g. Kiviluoto and Oja, 1998), and separation of coalesced signals and instrument systematics in astrophysics (e.g. Stivoli et al., 2006; Maino et al., 2002, 2007; Aumont and Macías-Pérez, 2007; Wang et al., 2010). The rationale for the case of exoplanetary light-curves is presented in Section 4.4.

4.2 ICA: statistical independence

The claim to obtain the source signals from a number of independent observations, without knowledge of the mixing coefficients, can be accomplished through some assumptions about the signals or the mixing matrix or both. Independent Component Analysis is a method to solve problems with the same structure as the "Cocktail Party Problem", assuming only statistical independence of the source signals. This is a very reasonable assumption in many cases, where the sources are separate, non-interacting physical systems. Moreover, it can be a good approximation even if it is not exactly true in practice (Hyvärinen et al., 2001b).

4.2.1 Definition of statistical independence

The concept of statistical independence is defined for random variables, i.e. variables that are associated with a probability density function (pdf). The conjunction of two or more random variables is a new random variable with a joint pdf. The variables are *statistically independent*

if and only if the joint pdf equals the product of the single variables' pdfs:

$$p_{x,y}(x,y) = p_x(x)p_y(y) \tag{4.5}$$

where x and y are two random variables, p_x and p_y are the respective pdfs, $p_{x,y}$ is their joint pdf. Equation 4.5 generalises in a natural way for more than two random variables.

Statistical independence is a much stronger property than uncorrelatedness. Two or more variables are *uncorrelated* if and only if the expectation for their product equals the product of the individual expectations:

$$E\{xy\} = E\{x\}E\{y\} \tag{4.6}$$

where x and y are random variables, and $E\{\cdot\}$ indicates the expectation value[1] of the variable in parenthesis. Equation 4.6 naturally generalises for more than two variables.

It is possible to show that a definition of statistical independence equivalent to the definition given in Equation 4.5, in terms of expectation values, is (Hyvärinen et al., 2001a):

$$E\{g(x)h(y)\} = E\{g(x)\}E\{h(y)\} \tag{4.7}$$

for all possible choices of the functions $g(x)$ and $h(y)$. Comparing Equation 4.6 and 4.7, it is evident that independent variables are uncorrelated, but not vice versa. However, it is noteworthy that, if the random variables have gaussian distributions, uncorrelatedness implies independence (Hyvärinen et al., 2001a).

4.2.2 Visualising statistical independence

An elementary way to visualise whether two variables are independent or not is to plot one as a function of the other. Consider two sets of n values generated through successive extractions of independent random variables, each one with a given pdf.

First, I consider the case of two sets s_1 and s_2 generated with uniform pdfs between -0.5 and 0.5. Plotting the points $(s_{1,i}, s_{2,i})$, with $i = 1, ..., n$, yields a uniform distribution of points over a square (Figure 4.1). The s_1 coordinate is independent of s_2 and vice versa: knowledge of the s_1 coordinate does not allow inference of the corresponding s_2 value. In order to mix the two sources, I applied an orthogonal matrix to the column vector $\mathbf{s} = (s_1 \ s_2)^T$, obtaining

[1] The expectation value of a random variable x is, intuitively, the sample mean of a large number of realizations of the variable. Mathematically, it is $E\{x\} = \int xp(x)dx$, where $p(x)$ is the random variable's pdf.

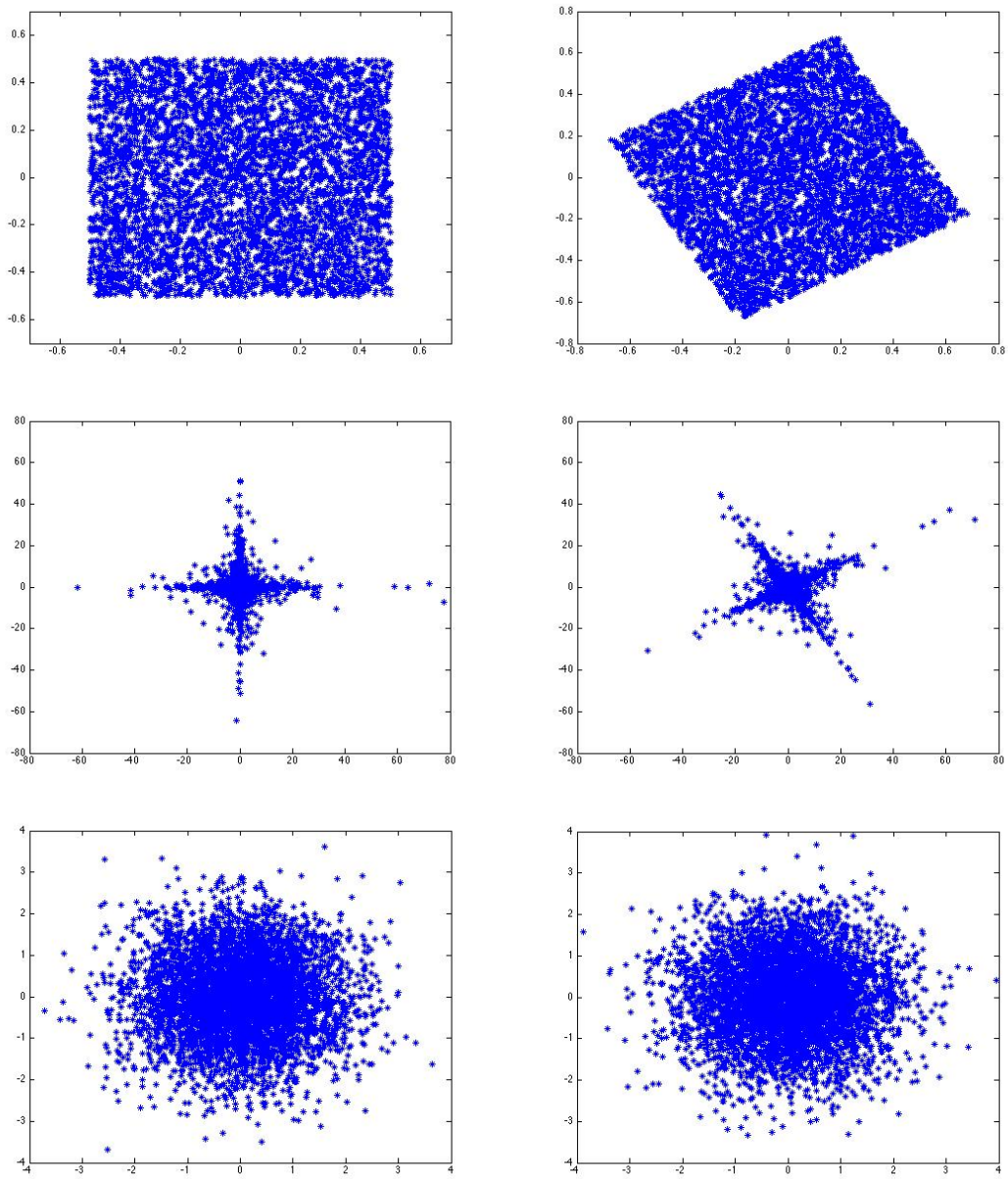

Figure 4.1: Plots of a random variable vector as function of another random variable vector with the same pdf. Top: uniform pdfs; Middle: exponential pdfs; Bottom: gaussian pdfs; Left: plot of the original vectors; Right: plot of the vectors after an orthogonal transformation.

$\mathbf{x} = (x_1\ x_2)^T$ as in Equation 4.3:

$$\begin{pmatrix} x_1 \\ x_2 \end{pmatrix} = \mathbf{A} \begin{pmatrix} s_1 \\ s_2 \end{pmatrix} \tag{4.8}$$

$$\mathbf{A} = \begin{pmatrix} \sqrt{3}/2 & -1/2 \\ 1/2 & \sqrt{3}/2 \end{pmatrix}. \tag{4.9}$$

The signals x_1 and x_2 are linear combinations of s_1 and s_2. Note that the plot of x_2 as a function of x_1 is a rotated square (see Figure 4.1, top panels). The rotated variables are no longer independent. For example, note that knowledge of $x_{1,i}$ constrains the range of possible values for $x_{2,i}$.

The case represented in the middle panels in Figure 4.1 is less obvious than the previous one but, again, the two original variables (left panel) are (generated) independent(ly) and the most striking indication is the alignment of the distribution along the axes. The rotation introduces a strong degree of dependence: moving x_1 away from zero, the conditional probability distribution for x_2 is bimodal, and the two peaks depend on the specific x_1 value.

Non-orthogonal transformations in general introduce a deformation, apart from the rotation; for example, if $\mathbf{A}$ in Equation 4.9 had not been orthogonal, the plot of Figure 4.1 top right would have been a parallelogram instead of a rotated square and the transformed variables would have been correlated. In practical applications, to find independent components from non-independent ones, it is convenient to first "remove the deformation" , then "rotate" to align the "main directions" with the axes. The discussion in this section makes use of heuristic concepts such as "main directions". More precise and advanced mathematical techniques, mostly used in practical applications, are described in Section 4.2.3.

Finally, I maintain the heuristic approach to make another point. The bottom panels in Figure 4.1 are relative to identical gaussian variables. In this case orthogonal transformations maintain the radial simmetry, so that there are no "main directions" to identify and the rotated diagram (right panel) is indistinguishable from the original one (left panel). These figures explain, intuitively, why gaussian uncorrelated signals are also independent.

4.2.3 Measuring statistical independence

Information entropy

Entropy is the basic concept of Information Theory. For a random vector $\mathbf{y} = (y_1, y_2, ..., y_n)$ it is defined as (Hyvärinen et al., 2001a):

$$H(\mathbf{y}) = -\int p(\mathbf{y}) \log p(\mathbf{y})\, d\mathbf{y} \qquad \text{for a continuous variable} \tag{4.10}$$

$$H(\mathbf{y}) = -\sum_k p(\mathbf{y}_k) \log p(\mathbf{y}_k) \qquad \text{for a discrete variable} \tag{4.11}$$

The index k associated to the bold-font variable $\mathbf{y}$ in Equation 4.11 indicates possible realizations of the multivariate variable $\mathbf{y}$. It must not be confused with the index of the vector's component, in which case the letter is not in bold. Entropy is a measure of the uncertainty associated with a random variable, as demonstrated, at least in part, by the following properties. For the case of a discrete variable:

1. H is minimum, i.e. zero, if there is only one exit with probability 1 and the others have probability 0 (no uncertainty);

2. H is maximum if all the possible exits for the variables are equally probable (maximum uncertainty).

For a continuous variable:

1. H is small, i.e. negative with a large absolute value, if $p(\mathbf{y})$ is concentrated within a strict interval;

2. among the $p(\mathbf{y})$ distributions which are non-zero over the same interval, H is maximum if the distribution is uniform.

Mutual information

Mutual information is a measure of the information that members of a set of random variables have on the other random variables in the set. If $\mathbf{y} = (y_1, y_2, ..., y_n)$ is the set of random variables, the mutual information is defined as

$$I(y_1, y_2, ..., y_n) = \sum_{i=1}^{n} H(y_i) - H(\mathbf{y}) \tag{4.12}$$

where H is the entropy function. Note that $I(y_1, y_2, ..., y_n) = 0$ if the variables are statistically independent, i.e. the joint pdf is factorizable, and $I(y_1, y_2, ..., y_n) > 0$ in all other cases. For the

source signals in Equation 4.4, the mutual information can be written as

$$I(s_1, s_2, ..., s_n) = \sum_{i=1}^{n} H(s_i) - H(\mathbf{x}) - \log|\det(\mathbf{W})| \tag{4.13}$$

If the x_i are uncorrelated and of unit variance (see Section 4.3.1), then $\det(\mathbf{W})$ is constant and it does not affect the search for the minimum mutual information or maximum independence. Because mutual information is hard to compute, different estimators are used in practical contexts.

Negentropy

Among all the distributions with fixed mean and covariance, the gaussian distribution has the maximum entropy. This property suggests defining negentropy as an estimator of non-gaussianity:

$$J(\mathbf{y}) = H(\mathbf{y}_{gauss}) - H(\mathbf{y}) \tag{4.14}$$

where $\mathbf{y}_{gauss}$ is a random gaussian vector with the same covariance matrix as $\mathbf{y}$. Its entropy is

$$H(\mathbf{y}_{gauss}) = \frac{1}{2}\log|\det(\mathbf{C}_y)| + \frac{n}{2}[1 + \log(2\pi)] \tag{4.15}$$

where $\mathbf{C}_y$ is the covariance matrix and n is the dimension of $\mathbf{y}$. The elements of the covariance matrix are the covariances between the components of the multivariate variable:

$$C_{ij} = \mathrm{cov}(y_i, y_j) = E\{(y_i - \overline{y}_i)(y_j - \overline{y}_j)\}. \tag{4.16}$$

Note that, from Equation 4.6, if y_i and y_j are uncorrelated, the covariance matrix is diagonal. Negentropy is a measure of non-gaussianity, being $J(\mathbf{y}) = 0$ if $\mathbf{y}$ is gaussian, and $J(\mathbf{y}) > 0$ in other cases.

The Central Limit Theorem states that the distribution of the sum (or any linear combination) of n independent random variables converges to a gaussian distribution in the limit $n \to \infty$. Generalising from this theorem, it can be inferred that, in most cases, a finite linear combination of independent random variables is "more gaussian" than both the original variables, where the (non-)gaussianity is a mathematically defined quantity. According to this theorem, in the ICA problem, the independent components are less gaussian than any linear combination, therefore can be obtained by maximising the sum of their non-gaussianities, e.g. their negentropies.

Because negentropy is also hard to compute, other estimators are typically used.

Kurtosis

Kurtosis is a fourth-order function of the moments of the pdf. In the zero-mean case it is defined by

$$\text{kurt}(y) = E\{y^4\} - 3E\{y^2\}^2 \tag{4.17}$$

or, in the normalised form, by

$$\tilde{\text{kurt}}(y) = \frac{E\{y^4\}}{E\{y^2\}^2} - 3 \tag{4.18}$$

Gaussian random variables have zero kurtosis, those with positive kurtosis are called super-gaussian (or leptokurtic), and are more peaked, those with negative kurtosis are called sub-gaussian (or platykurtic), and are flatter. There exist also non-gaussian random variables with zero kurtosis, but they are very rare. For these reasons kurtosis, or rather its absolute value, is used as a measure of non-gaussianity. For two scalar random variables, y_1 and y_2, and a numerical constant, α, the following linearity properties are valid:

$$\text{kurt}(y_1 + y_2) = \text{kurt}(y_1) + \text{kurt}(y_2) \tag{4.19}$$

$$\text{kurt}(\alpha y_1) = \alpha^4 \text{kurt}(y_1) \tag{4.20}$$

The major advantage of kurtosis is its simplicity, but it is not an optimal estimator, because its range, i.e. $[-2, +\infty[$, is not symmetric. In addition, it is very sensitive to outliers.

Negentropy approximations: contrast functions

Hyv̈arinen (1999) developed a formula to approximate negentropy:

$$J(y) \approx \sum_{i=1}^{p} k_i [E\{G_i(y)\} - E\{G_i(\nu)\}]^2 \tag{4.21}$$

where k_i are some positive constants, and ν is a random gaussian variable of zero mean and unit variance, the variable y is assumed to be of zero mean and unit variance, and the functions G_i are not quadratic. The G_i functions are called "contrast functions". Often, only one contrast function is used, so that Equation 4.21 becomes

$$J(y) \propto [E\{G(y)\} - E\{G(\nu)\}]^2 \tag{4.22}$$

Examples of contrast functions commonly adopted are:

$$G_1(y) = \frac{1}{a_1} log[\cosh(a_1 y)] \tag{4.23}$$

$$G_2(y) = -\exp(-y^2/2) \tag{4.24}$$

$$G_3(y) = \frac{1}{4} y^4 \tag{4.25}$$

The choice of the contrast functions is important to optimise the performances of the algorithm. This point is discussed in Section 4.3 for specific algorithms.

Temporal correlations

The definitions of uncorrelatedness and independence for time series are:

$$E\{(y_i(t) - \overline{y}_i)(y_j(t) - \overline{y}_j)\} = \rho_i \delta_{ij} \qquad \text{(uncorrelatedness)} \tag{4.26}$$

$$E\{(y_i(t+\tau) - \overline{y}_i)(y_j(t+\tau) - \overline{y}_j)\} = \rho_i(\tau) \delta_{ij} \qquad \text{(independence)} \tag{4.27}$$

where $\rho_i(\tau)$ is the so-called time-lagged covariance of the i-th component, δ_{ij} is Kronecker's delta, i.e. δ_{ii} =1 and δ_{ij} =0 if $i \neq j$. The time covariances in Equation 4.26 differ from the covariances in Equation 4.16, as the time covariances only use the products at corresponding times, while the covariances include all the possible products between two variable's realizations. A non-zero time covariance between two time series indicates that they have a similar temporal structure, at least in part. In some cases, two identical signals with a relative time shift can have also a zero time covariance, but they are clearly not independent. Equation 4.27 states that, for independent signals, the time-lagged covariances are all equal to zero.

4.3 ICA: algorithm

Many algorithms have been written with different implementations of the ICA technique. I will not discuss all the existing algorithms, but I will present a list of algorithms which are propaedeutic to the code that I adopted in this Thesis, i.e. MULTICOMBI (Tichavsky et al., 2008), and, of course, the MULTICOMBI code itself. The code can be downloaded from Tichavsky's home page (http://si.utia.cas.cz/downloadPT.htm). The descriptions of the algorithms will not include the derivations of all the formulas, which are beyond the scope of this Thesis and, in most cases, they would require tens of pages filled with mathematical formulas. I refer to the relevant literature for technical and mathematical details about the algorithms presented.

4.3.1 Whitening

Whitening is useful pre-processing step common to many ICA algorithms, though it is not strictly necessary. It is a transformation of the input signals into mean-subtracted uncorrelated (according to Equation 4.6) components with unit variances:

$$\tilde{\mathbf{x}} = \mathbf{V}\left(\mathbf{x} - \bar{\mathbf{x}}\right) \tag{4.28}$$

where $\bar{\mathbf{x}} = (\bar{x}_1\ \bar{x}_2 \ldots \bar{x}_n)^T$. A simple and fast method to calculate a possible whitening matrix, $\mathbf{V}$, is by using the eigenvalue decomposition of the covariance matrix:

$$\mathbf{C}_x = \mathbf{E}\mathbf{D}\mathbf{E}^T \tag{4.29}$$

where $\mathbf{C}_x$ denotes the covariance matrix of $\mathbf{x}$, $\mathbf{E}$ is the orthogonal matrix of eigenvectors and $\mathbf{D}$ is the diagonal matrix of its eigenvalues. Then:

$$\mathbf{V} = \mathbf{E}\mathbf{D}^{-\frac{1}{2}}\mathbf{E}^T = \mathbf{C}_x^{-\frac{1}{2}} \tag{4.30}$$

The $\mathbf{D}$ and $\mathbf{E}$ matrices can be obtained through a Principal Component Analysis (Hyvärinen et al., 2001b; Jolliffe, 2002).

The whitening matrix is not unique. If $\mathbf{O}$ is an orthogonal matrix, $\mathbf{V'} = \mathbf{VO}$ is also a valid whitening matrix. Being uncorrelated is a necessary condition for independence, so the inverse mixing matrix for the problem with whitened data,

$$\tilde{\mathbf{s}} = \tilde{\mathbf{W}}\tilde{\mathbf{x}}, \tag{4.31}$$

must be orthogonal. This reduces the number of coefficients to determine from n^2 to $n(n-1)/2$. How to find $\tilde{\mathbf{W}}$ to obtain the independent components is the argument of the following Sections 4.3.3–4.3.8.

The two-step process of whitening followed by an appropriate orthogonal transformation is the mathematical equivalent of the heuristic "remove the deformation" and then "rotate" described in Section 4.2.2.

4.3.2 Interference-to-Signal Ratio

Before describing the ICA algorithms, I introduce the concept of Interference-to-Signal Ratio (ISR) matrix. If the source signals $\tilde{\mathbf{s}}_i$ and the mixing matrix $\tilde{\mathbf{A}}$ are known, it is possible to

evaluate the quality of the separation, via the so-called gain matrix $\tilde{\mathbf{G}}$:

$$\tilde{\mathbf{G}} = \hat{\tilde{\mathbf{W}}}\mathbf{A} \approx I \tag{4.32}$$

where $\hat{\tilde{\mathbf{W}}}$ is the estimated demixing or inverse matrix. In case of perfect demixing, the gain matrix $\tilde{\mathbf{G}}$ is the identity. Non-diagonal terms $\tilde{\mathbf{G}}_{ij}$ indicate the residual contamination of the i-th component in the estimated j-th one. The Interference-to-Signal Ratio (**ISR**) matrix is defined by:

$$\mathbf{ISR}_{ij} = \frac{\tilde{\mathbf{G}}_{ij}^2}{\tilde{\mathbf{G}}_{ii}^2} \approx \tilde{\mathbf{G}}_{ij}^2 \tag{4.33}$$

The interference-to-signal ratio for the i-th estimated component is:

$$\mathbf{isr}_i = \frac{\sum_{j=1, j\neq i}^{n} \tilde{\mathbf{G}}_{ij}^2}{\tilde{\mathbf{G}}_{ii}^2} \tag{4.34}$$

In a real case, where the source signals and the mixing matrix are not known, Equation 4.32 cannot be used. However, for specific algorithms, it is possible to compute theoretical estimates of the **ISR** matrix (Yeredor, 2000; Koldovsky et al., 2006; Tichavsky et al., 2006, 2008).

4.3.3 Iterative FastICA

Iterative FastICA is one of the oldest and simplest ICA algorithms (Hyvärinen and Oja, 2000). It sequentially extracts the independent components by maximising the negentropies of the projections $J(\tilde{\mathbf{w}}_i^T \tilde{\mathbf{x}})$, where $\tilde{\mathbf{w}}_i$ is the i-th row of the inverse mixing matrix $\tilde{\mathbf{W}}$. Assuming that i components have been extracted, the $(i+1)$-th is computed by the following iteration scheme:

1. Choose an initial weight vector $\tilde{\mathbf{w}}_{i+1}$;

2. Increment:
$$\tilde{\mathbf{w}}_{i+1} = E\{\tilde{\mathbf{x}} g(\tilde{\mathbf{w}}_{i+1}^T \tilde{\mathbf{x}})\} - E\{g'(\tilde{\mathbf{w}}_{i+1}^T \tilde{\mathbf{x}})\}\tilde{\mathbf{w}}_{i+1}; \tag{4.35}$$

3. Decorrelate:
$$\tilde{\mathbf{w}}_{i+1} = \tilde{\mathbf{w}}_{i+1} - \sum_{j=1}^{i} \tilde{\mathbf{w}}_{i+1}^T \tilde{\mathbf{w}}_j \tilde{\mathbf{w}}_j; \tag{4.36}$$

4. Normalise:
$$\tilde{\mathbf{w}}_{i+1} = \frac{\tilde{\mathbf{w}}_{i+1}}{||\tilde{\mathbf{w}}_{i+1}||} \tag{4.37}$$

5. If not converged, i.e. condition on the distance between the updated $\tilde{\mathbf{w}}_{i+1}$ and the one at the previous iteration, go back to 2.

The g function in Equation 4.35 is the derivative of a non-linearity G (see Equations 4.22–4.25). A disadvantage of the iterative scheme is that the estimation errors build up in the process.

4.3.4 Parallel FastICA

Parallel FastICA uses a similar iteration scheme (Hyvärinen and Oja, 2000), but the components are estimated simultaneously, so that the estimation errors are uniformly distributed:

1. Choose an initial orthogonal matrix $\tilde{\mathbf{W}}$;
2. Increment:
$$\tilde{\mathbf{W}} = g\left(\tilde{\mathbf{W}}\tilde{\mathbf{x}}\right)\tilde{\mathbf{x}}^T - \operatorname{diag}\left[g'\left(\tilde{\mathbf{W}}\tilde{\mathbf{x}}\right)\mathbf{1}_n\right]\tilde{\mathbf{W}} \tag{4.38}$$
(here $\mathbf{1}_n$ is a column vector of ones);
3. Symmetric orthogonalisation:
$$\tilde{\mathbf{W}} = \left(\tilde{\mathbf{W}}\tilde{\mathbf{W}}^T\right)^{-\frac{1}{2}}\tilde{\mathbf{W}} \tag{4.39}$$

The performance of the FastICA algorithms depends on the choice of the non-linearity g and the statistical properties of the independent random variables.

4.3.5 EFICA

EFICA stands for Efficient FastICA. It is an evolution of the FastICA algorithm with an adaptive choice of the non-linearity g (Koldovsky et al., 2006). It consists of the following three steps:

1. running the parallel FastICA algorithm with a predetermined non-linearity, e.g. $g(s) = \tanh s$;
2. adaptive choice of the non-linearities g_i for each component;
3. running a modified FastICA algorithm with the optimal non-linearities.

The non-linearities in step 2 are assigned according to the following scheme, based on the fourth moment of the component's distribution:

$$g_i(s) = \begin{cases} s\ e^{-\eta_1|s|}, & \text{for } \left\langle s_i^4\right\rangle > 3 \\ sign(s)\cdot|s|^{min(\alpha_i-1,14)}, & \text{for } 1.8 < \left\langle s_i^4\right\rangle \leq 3 \\ sign(s)\cdot|s|^{14}, & \text{for } \left\langle s_i^4\right\rangle \leq 1.8 \end{cases} \tag{4.40}$$

where $\eta_1 = 3.348$ and α_i is the index of the Generalized Gaussian distribution (Koldovsky et al., 2006) with fourth moment equal to $\left\langle s_i^4\right\rangle$.

4.3.6 SOBI and WASOBI

SOBI is a popular algorithm to separate gaussian auto-regressive signals, i.e. when the output variable is linearly dependent on the previous values and a stochastic term (Belouchrani et al., 1997). It adopts the definition of independence from Equation 4.27, leading to the equation

$$\tilde{\mathbf{W}} E\left\{\tilde{\mathbf{x}}(t+\tau)\tilde{\mathbf{x}}^T(t)\right\}\tilde{\mathbf{W}}^T = \mathbf{I} \tag{4.41}$$

for any time-lag τ. The matrix $\tilde{\mathbf{W}}$ is estimated as an approximate joint diagonaliser for a set of lagged-covariance matrices

$$\tilde{\mathbf{R}}_{\tilde{\mathbf{x}}}(\tau_k) = E\left\{\tilde{\mathbf{x}}(t+\tau_k)\tilde{\mathbf{x}}^T(t)\right\} \tag{4.42}$$

The approximate joint diagonaliser is obtained by minimising an estimator of non-diagonality for the $\tilde{\mathbf{W}}\tilde{\mathbf{R}}_{\tilde{\mathbf{x}}}(\tau_k)\tilde{\mathbf{W}}^T$ matrices in a least-squares sense. WASOBI is a Weights-Adjusted SOBI algorithm (Yeredor, 2000), which incorporates proper weighting, inversely proportional to the covariance in the correlation estimates, in the fitting of the joint diagonaliser.

4.3.7 COMBI

EFICA and WASOBI are complementary algorithms, as the former is designed to separate mixtures of non-gaussian signals, while the latter is designed to separate gaussian auto-regressive signals. Typically, real data are mixtures of both non-gaussian and gaussian signals. The COMBI algorithm includes the EFICA and WASOBI algorithms for a better separation of such data (Tichavský et al., 2006). It proceeds as follows:

1. Apply both EFICA and WASOBI to $\tilde{\mathbf{x}}$; let the estimated source signals $\tilde{\mathbf{s}}^{EF}$ and $\tilde{\mathbf{s}}^{WA}$ respectively, the interference matrices $\mathbf{ISR}^{EF}$ and $\mathbf{ISR}^{WA}$, the corresponding vectors $\mathbf{isr}^{EF}$ and $\mathbf{isr}^{WA}$;

2. Let $E = min_k \mathbf{isr}_k^{EF}$ and $W = min_k \mathbf{isr}_k^{WA}$;

3. If $E < W$, accept those signals $\mathbf{s}^{EF}$ for which $\mathbf{isr}_k^{EF} < W$, else those $\mathbf{s}^{WA}$ for which $\mathbf{isr}_k^{WA} < E$; reject the other signals;

4. If there is more than one rejected signal, start again from step 1.

4.3.8 MULTICOMBI

It is possible to have sets of signal components well separable from the others in the mixture but difficult to separate one from another in the same set. It might be the case of nearly

gaussian distribution signals for EFICA, and signals with similar power spectra for WASOBI. The algorithm MULTICOMBI is a sort of hierarchical multistep COMBI, in order to separate clusters of signals in subclusters until all clusters are singletons (Tichavsky et al., 2008). The interference-to-signal ratio for clusters of signals is defined as:

$$isr(\zeta) = \alpha_\zeta \sum_{i \in \zeta, j \notin \zeta} \mathbf{ISR}_{ij} \tag{4.43}$$

where ζ denotes a cluster and α_ζ is a normalization coefficient:

$$\alpha_\zeta = \frac{d-1}{|\zeta|(d-|\zeta|)} \tag{4.44}$$

being d the number of signals and $|\zeta|$ the dimension of the cluster ζ.
The algorithm MULTICOMBI runs as follows:

1. Pick any cluster in $\mathbf{x}$ that is not a singleton; let $\mathbf{z}$ be a generic cluster;
2. Apply both EFICA and WASOBI to each cluster, obtaining the separated signals $\mathbf{s}^{EF}$ and $\mathbf{s}^{WA}$, the estimated matrices $\mathbf{ISR}^{EF}$ and $\mathbf{ISR}^{WA}$;
3. Consider any subcluster ζ, and compute $isr^{EF}(\zeta)$ and $isr^{WA}(\zeta)$;
4. Let $E = \min_\zeta isr^{EF}(\zeta)$ and $W = \min_\zeta isr^{WA}(\zeta)$;
5. If $E < W$ pick up the best EFICA-separated clusters, one to one until there are no EFICA-separated clusters remaining or the best of them is worse than the best WASOBI-separated cluster and extract the new subclusters and related signals from $\mathbf{s}^{EF}$; else extract similarly the new subclusters and related signals from $\mathbf{s}^{WA}$;
6. Repeat the same procedure until all signals extracted are singletons.

4.3.9 Rescaling the signals

After extracting the independent components from the whitened data, the subtracted mean can be reinstated by combining Equations 4.31 and 4.28, then readjusting to obtain

$$\mathbf{s} = \tilde{\mathbf{s}} + \tilde{\mathbf{W}}\mathbf{V}\bar{\mathbf{x}} = \tilde{\mathbf{W}}\mathbf{V}\mathbf{x}, \tag{4.45}$$

which is equivalent to Equation 4.4 with the identification

$$\mathbf{W} = \tilde{\mathbf{W}}\mathbf{V} \tag{4.46}$$

However, it must be noted that the source signals can be retrieved up to a scaling factor. This can be seen because multiplying one source signal by a scalar factor and dividing the corresponding column of the mixing matrix by the same factor, as shown in Equation 4.47, produces the same mixed signals without affecting the statistical independence of the sources:

$$\mathbf{x} = \left(\dots \frac{\mathbf{a}_j}{\alpha_j} \dots \right) (\dots \alpha_j s_j \dots)^T \tag{4.47}$$

where α_j is a scalar factor and $\mathbf{a}_j$ is the i-th column of $\mathbf{A}$. This ambiguity is not problematic in many contexts, including the study of transits, for two reasons:

1. the scaling factors can be retrieved by fitting the source signals to the observed light-curves (see Section 5.2.1);
2. the information about the planet is contained in the observed flux decrement relative to the stellar flux.

4.4 Rationale

An exoplanetary transit or eclipse light-curve is the sum of more than one signal. It contains at least three contributors:

1. the astrophysical signal;
2. the systematic noise component, mostly instrumental effects;
3. stochastic noise.

These are mutually independent, originating from independent sources, which makes it possible to separate them using ICA. It is possible to decompose further both the astrophysical and systematic signals, if they are sums of several independent effects. For example, in the case of an exoplanetary transit, the main astrophysical signal is given by the partial obscuration of the star due to the planet, but there might be also stellar variability effects, especially for active stars. As discussed in Section 4.1, in order to disentangle n components, an equal number of observations (light-curves, in the context of interest) is required. The number of physical components is not known a priori, but it can be determined a posteriori, if enough lightcurves (more, or as numerous as, the components) have been used.

Chapter 5

Application to *Spitzer*/IRAC transit observations

"To acquire knowledge, one must study; but to acquire wisdom, one must observe."

— **Marilyn Vos Savant**

5.1 Spitzer Space Telescope

The Spitzer Space Telescope is an infrared space-borne observatory launched in 2003. It is one of the four NASA Great Observatories, each one dedicated to cover a specific region of the electromagnetic spectrum. It follows a heliocentric orbit, trailing and drifting away from Earth's orbit at approximately 0.1 AU per year, a so-called "earth-trailing" orbit. The telescope has an aperture of 85 cm diameter. Since it is designed to detect infrared radiation, its detectors and telescope were cooled to less than 5.5 K to avoid that its own thermal emission interferes with its observations, using liquid helium as a cryogen. There are three infrared detectors:

- the InfraRed Array Camera (IRAC), which performs photometry in four bands at nominal wavelengths 3.6 μm (channel 1), 4.5 μm (channel 2), 5.8 μm (channel 3) and 8.0 μm (channel 4);
- the InfraRed Spectrograph (IRS), with low spectral resolution in the ranges 5.3–14 μm and 14–40 μm and high spectral resolution in the ranges 10–19.5 μm and 19–37 μm;
- the Multiband Imaging Photometer (MIPS), working at 24 μm, 70 μm, 160 μm and able to perform spectroscopy.

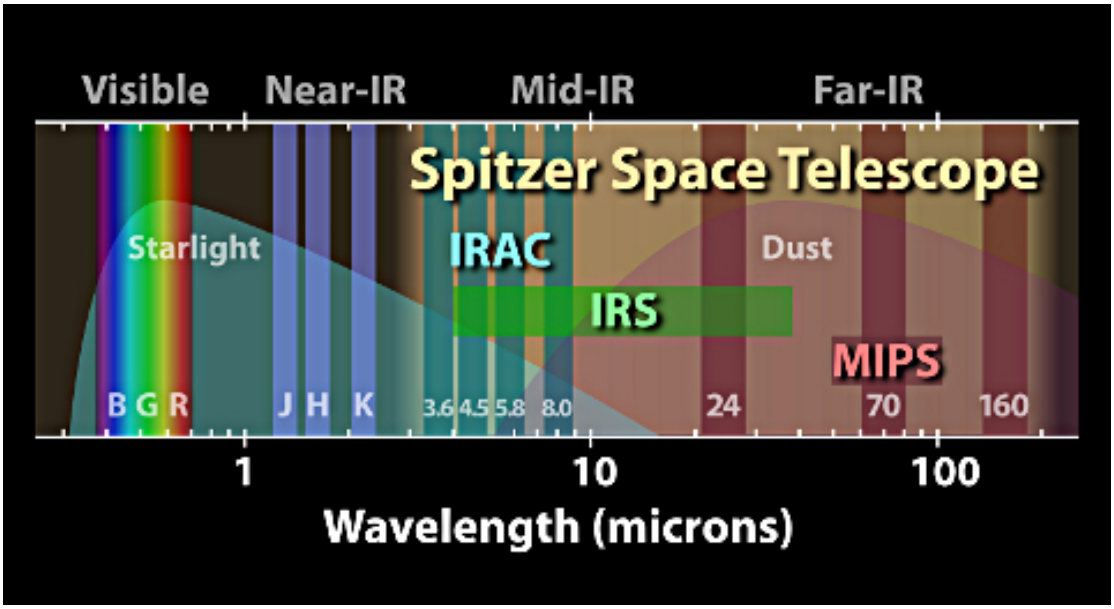

Figure 5.1: Observational bands of the three infrared detectors of Spitzer: IRAC, IRS and MIPS. In order to put Spitzer bands in context, the figure also shows the blackbody spectrum of a sun-like star and the dust spectral emission along with standard photometric bands in the optical (B, G, R) and infrared (J, H, K) bands.

Since depletion of liquid helium supply in May 2009, most of the instruments are no longer usable, except the two IRAC channels at 3.6 and 4.5 μm, which are now operating in the so-called "*Spitzer* Warm Mission".

5.1.1 The InfraRed Array Camera (IRAC)

Overview

IRAC is a four-channel camera that has four detectors, each with a small bandpass around its nominal wavelength (see Figure 5.2). The detectors are square arrays of 256×256 pixels in size. Their mounting is such that channels 1 and 3 observe the same field of view (within a few pixels), and the other two channels observe another field of view simultaneously. The two fields of view are $5.2' \times 5.2'$ and are separated by $\sim 1.52'$, with no overlap. The spatial scale is $\sim 1.2''$/pixel. Table 5.1 reports basic properties of the detectors "Point Response Function", on which I will comment in Section 5.2.

Readout modes and frame times

In full-array readout mode, there were four selectable frame times during the cryogenic mission: 2, 12, 30, and 100 *s*. The warm mission added the 0.4 and 6 *s* frame times.

Stellar photometry mode was available for observations of objects much brighter in channels 1 and 2 than in 3 and 4 (typically stars) in the cryogenic mission. This mode took short exposures

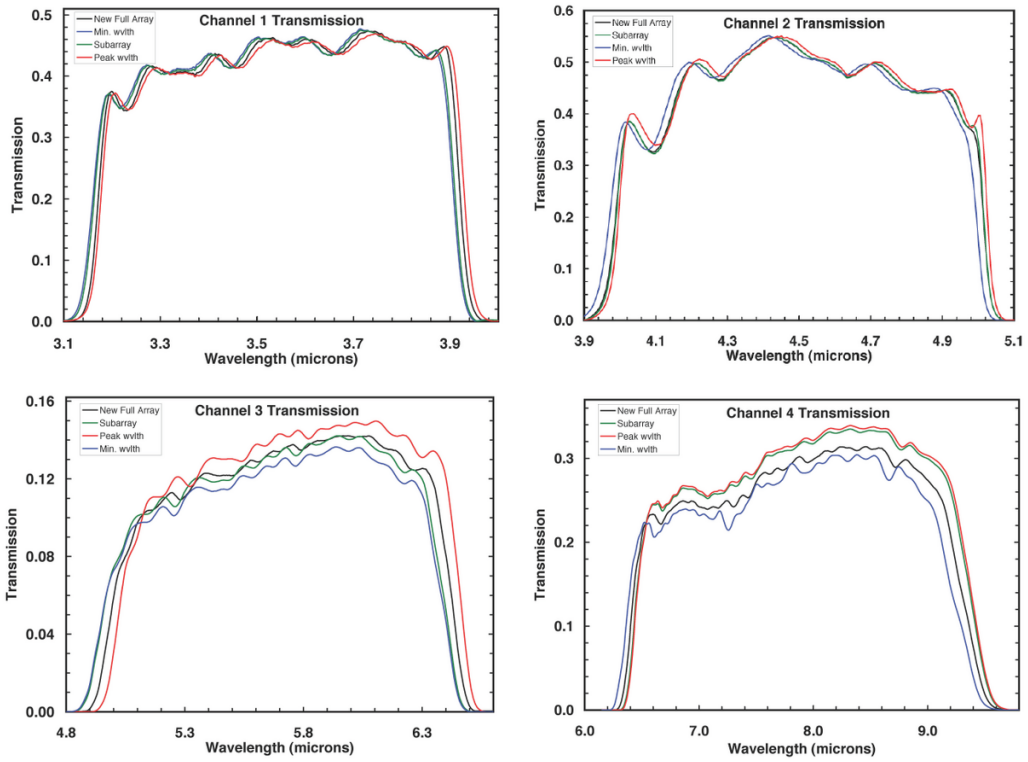

Figure 5.2: Spectral response (throughput) curves for all four IRAC channels, in particular, (black) the full-array average curve, (green) the sub-array average curve. Also shown the transmission curves of two individual pixels having (blue) the minimum and (red) the maximum average wavelength. Figure from the IRAC Instrument Handbook.

channel	FWHM (mean,″)	FWHM (centered PRF, ″)	central pixel flux (peak, %)
1	1.66	1.44	42
2	1.72	1.43	43
3	1.88	1.49	29
4	1.98	1.71	22

Table 5.1: Properties of the Point Response Function for the four IRAC detectors. The first column reports the Full Width at Half Maximum of the Point Response Functions averaged over the detectors. The second column is for a source well-centered in a pixel. The third column is the percentage of flux in the central pixel for a source well-centered in the pixel. Table from the IRAC Instrument Handbook.

in channels 1 and 2, and longer exposures in channels 3 and 4. Three framesets were available. The shortest set took a single 0.4 s frame in channels 1 and 2, and a 2 s frame in channels 3 and 4. The next set took two undithered 2 s frames in channels 1 and 2, and a 12 s frame in channels 3 and 4. The longest frame time combination took two undithered 12 s frames in channels 1 and 2, and a 30 s frame in channels 3 and 4.

For very bright sources, a sub-array mode is available. In this mode, only a 32×32 pixel portion of the array is read. There were three selectable frame times: 0.02, 0.1, and 0.4 s. The warm mission added the 2 s frame time. For each repeat in sub-array mode, a set of 64 consecutive frames is taken.

Basic Calibrated Data

The Spitzer Science Center performed routine calibrations of IRAC, using observations of standard stars and other astronomical objects. The IRAC Level 1 pipeline is designed to take a single Level 0 image, i.e. the raw output, from a single IRAC detector and produce a flat-fielded, cosmic ray-corrected and flux-calibrated image with all well known instrumental systematic effects (systematics) removed. These are called Basic Calibrated Data (BCD), and are identified by the final part of their names and extension: "bcd.fits". They are used as starting point in my analyses.

Other systematics

The data analysed in this Thesis have been observed with the IRAC channels 1 and 2. The systematic effects present in data sets from these two detectors are mostly caused by spacecraft-induced motions coupled with intra-pixel sensitivity variations. This can be inferred from the correlations between the measured flux and the source's centroid positions on the detector array.

The most notable effect is a sawtooth modulation (Fazio et al., 2004; Reach et al., 2005; Morales-Calderón et al., 2006). This originally had a period of ∼1 hr, an amplitude of ∼0.15″ in the centroid position, corresponding to 1/8 the pixel size, and up to 5% in flux variations. It is believed to be due to thermo-mechanical expansions and contractions of many spacecraft components, caused by the periodic on-off cycling of a battery heater within the spacecraft bus (Grillmair et al., 2012; Krick et al., 2015). After the cycling range was reduced on 17 October 2010, the period changed to ∼39 min and the amplitude of the centroid oscillation reduced by a factor 2.

Some observations show an initial pointing drift, also called settling drift, of up to 0.5″ over 30–60 min, which appears to be caused by thermal heating due to the incident solar light,

depending on the orientation of the spacecraft (Grillmair et al., 2012; Krick et al., 2015).

A long-term drift of $\sim 0.34''$ per day is probably due to small inconsistencies in the velocity aberration corrections (Grillmair et al., 2012; Krick et al., 2015).

Higher-frequency jitter is detected with periods ranging from 0.02 s to 3 min, potentially caused by many effects (Grillmair et al., 2012; Krick et al., 2015).

Systematics detrending pipelines

Because of the known coupling between the centroid position and the intra-pixel sensitivity, the earliest methods for correcting the instrument systematics in *Spitzer*/IRAC observations at 3.6 and 4.5 μm used either a simple radial function from a pixel's center (Reach et al., 2005; Morales-Calderón et al., 2006) or a polynomial function of the x and y coordinates (e.g., Charbonneau et al., 2005; Stevenson et al., 2010; Beaulieu et al., 2011; Knutson et al., 2011). Multiple reanalyses of the same data sets with the polynomial method show that, in some cases, results can be sensitive to some specific options/variants, such as the degree of the polynomial adopted, partial data rejection, including temporal or other decorrelations (e.g. Beaulieu et al., 2008, 2011; Désert et al., 2009; Stevenson et al., 2010; Knutson et al., 2011). The necessity of more objective and effective techniques to achieve the precision for characterising the exoplanetary atmospheres became clear. Several alternative methods have been proposed by different teams to decorrelate *Spitzer*/IRAC data: gain mapping (Ballard et al., 2010a; Cowan et al., 2012; Knutson et al., 2012; Lewis et al., 2013; Zellem et al., 2014), bilinearly interpolated sub-pixel sensitivity mapping (BLISS, Stevenson et al., 2012), Independent Component Analysis using pixel time series (pixel-ICA; Morello et al., 2014, 2015), pixel-level decorrelation (PLD; Deming et al., 2015), and Gaussian Process models (Evans et al., 2015).

5.2 Pixel-ICA

The algorithm that I have developed to decorrelate *Spitzer*/IRAC data is called "pixel-ICA", as it uses the time series registered by individual pixels, so-called "pixel light-curves", as input for the ICA. This is possible because, even if stars are approximate point sources of light which are not resolved by detectors, they are typically detected with a spatial distribution of intensity on a finite region of the detector, which contains or intersects more than one pixel. The intensity profile immediately before the light reaches the detector is the so-called "Point Spread Function" (PSF), and it is determined by the optics; the measured intensity profile also depends on the response of the detector, and it is called "Point Response Function" (PRF) [1]. Table 5.1 reports

[1] The distinction between PSF and PRF is not important in this discussion.

the Full Width at Half Maximum for the IRAC detectors (showing that is larger than the pixel size of 1.2″), and the maximum percentage of flux in the central pixel relative to the total flux (showing that a significant amount of stellar flux is spread over the surrounding pixels). Since

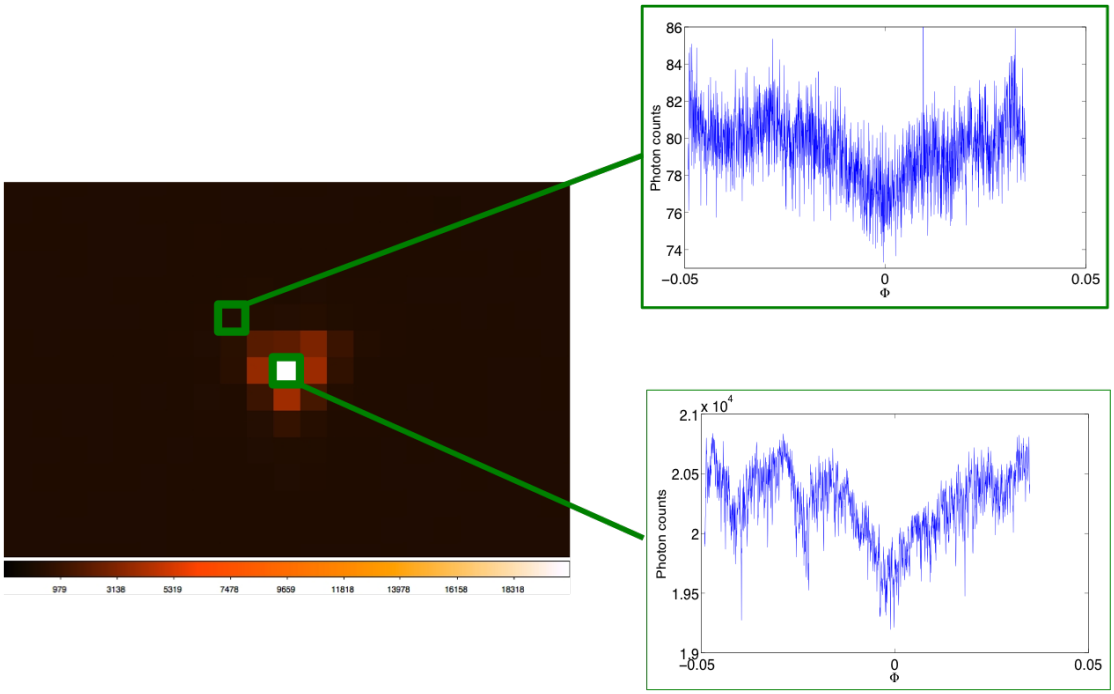

Figure 5.3: Representation of a *Spitzer*/IRAC frame showing the stellar source spread in more than one pixel and two examples of pixel light-curves.

the star's centroid is stable to within 1 pixel during a typical transit observation, i.e. few hours, there will be multiple pixels detecting the same astrophysical signals at all times, but with different scaling factors, depending on their sensitivity and the instrument PSF. The diversity of the signals registered by the pixels allows extraction of the various components.

After extracting the independent components from a selected set of pixel light-curves, different approaches to obtain the transit signal can be considered.

Method 1: *direct identification of the transit component.* If one of the independent components has the morphology of the transit signal, it can be identified with the transit signal itself, up to an undetermined scaling factor. This component can be normalised by the mean value calculated on the out-of-transit part, so that the out-of-transit level is unity, then fitted with a transit model. Alternatively, the normalisation factor can be fitted simultaneously with the transit model. This method is not applicable to the ICA extraction from spectroscopically resolved observations at different wavelengths because of the wavelength dependence of the stellar limb darkening effect. This is not a problem in our case, because all the pixels record the same wavelengths.

Method 2: *non-transit components subtraction.* Another approach to estimating the transit

signal is to remove all the other effects from an observed light-curve, i.e., by subtracting all the components other than the transit one, properly scaled. The scaling factors can be determined by fitting a linear combination of the components, plus a constant term, to the out-of-transit part of the light-curve. After subtraction, the detrended transit signal is normalised and model-fitted.

These two methods were implemented in the original version of the pixel-ICA algorithm, which I adopted for the data analyses discussed in this Chapter. Recently, I have considered a third method.

Method 3: *non-transit components + transit model fitting.* Similar to method 2, but the non-transit components are fitted over the whole time series, not just out-of-transit, simultaneously with the transit model and its normalisation factor. No constant term is needed in this configuration.

According to the mixing model, the pixel light-curves are linear combinations of the same components, so that any of them can be potentially chosen as reference light-curve to apply methods 2 and 3. Under this hypothesis, the spatially integrated light-curve, obtained by summing all the individual pixel light-curves, is also a linear combination of the same components. I found that using the integrated light-curve as the reference is advantageous, because it is less noisy than the individual pixel light-curves. The validity and the limits of the ICA model have been assessed with several tests and analysis of the residuals over a long list of real and simulated datasets, as discussed in the next sections of this chapter, in the following chapters and in the relevant peer-reviewed publications.

5.2.1 Light-curve fitting and error bars

When applying method 2, i.e. sequential detrending and astrophysical model-fitting, I used a Nelder-Mead optimisation algorithm (Lagarias et al., 1998) to obtain point estimates of the coefficients of the non-transit components to subtract from the reference light-curve. Then, I used the same algorithm to find point estimates of the free parameters in the transit model, followed by a MCMC calculation (Haario et al., 2006), as described in Section 3.3.5. When applying method 3, the coefficients of the components are included as free parameters in the MCMC fitting.

Let $\sigma_{par,0}$ be the standard deviation of a parameter chain. This would be the parameter error bar based on the fitting residuals, assuming no bias is introduced by the detrending method and the model adopted. For the ICA detrending, it is possible to estimate the uncertainty on the components extracted using the **ISR** matrix (see Section 4.3.2). I represented this as an additional term, σ_{ICA}, on each point in the time series. If σ_0^2 is the sampled likelihood's variance,

approximately equal to the variance of the residuals, then the total likelihood's variance is

$$\sigma_{like}^2 = \sigma_0^2 + \sigma_{ICA}^2 \tag{5.1}$$

The MCMC fitting should be repeated with the updated likelihood's variance to determine the final parameter error bars, σ_{par}. I found that, in the cases analysed, this approach is equivalent to rescaling the error bars as

$$\sigma_{par} = \sqrt{\frac{\sigma_0^2 + \sigma_{ICA}^2}{\sigma_0^2}}. \tag{5.2}$$

The formulas adopted for σ_{ICA} are:

$$\sigma_{ICA}^2 = \begin{cases} f^2 \mathbf{ISR}_i & \text{method 1} \\ f^2 \left(\sum_j o_j^2 \mathbf{ISR}_j + \sigma_{ntc-fit}^2 \right) & \text{method 2} \\ \sum_j o_j^2 \mathbf{ISR}_j & \text{method 3} \end{cases} \tag{5.3}$$

where

$$\mathbf{ISR}_i = \sum_{j=1, j \neq i}^{n} \mathbf{ISR}_{ij}, \tag{5.4}$$

is the interference-to-signal ratio for the i-th component, i.e. a sort of theorical root-mean-square error associated with the i-th component. If method 1 is adopted, with i the index of the transit component, this term is a direct estimate of the uncertainty in the transit component. If it is normalised prior to fitting the transit model and σ_0 is relative to the normalised component, then σ_{ICA} also needs to be rescaled by the same factor, f. If method 2 is adopted, o_j are the coefficients associated with the non-transit components, and $\sigma_{ntc-fit}$ is the standard deviation of residuals for the non-transit components out-of-transit. The first term is the sum of the uncertainties associated with the components included in the fit, while the second term accounts for the remaining variance. The first term increases with the number of components, while the second term should decrease. Similarly to method 1, if the detrended transit signal is normalised prior to fitting the astrophysical model, the σ_{ICA} term must be scaled accordingly. The formula for method 3 derives from the one for method 2. The $\sigma_{ntc-fit}$ term disappears because all the residuals are included in σ_0, being the non-transit components' coefficients and the astrophysical parameters fitted simultaneously.

5.3 Transits of HD189733b

5.3.1 The exoplanetary system around HD189733

The exoplanet HD189733b is a hot-Jupiter with mass $\sim$1.15 M_J and radius $\sim$1.2 R_J, orbiting a main-sequence K star at a distance of $\sim$0.0312 AU with a period of $\sim$2.2 days (Bouchy et al., 2005). The host star has an apparent magnitude of $\sim$5.5 in the infrared K band. The transit depth is of the order of 2–3% relative to the stellar flux. These properties make HD189733b one of the most favorable targets for extensive atmospheric examination. Tinetti et al. (2007) announced the detection of water vapour in its atmosphere, based on differences in transit depth measured with *Spitzer*/IRAC at 3.6 and 5.8 μm (Beaulieu et al., 2008). A subsequent reanalysis of the same observations with a different parameterization of the instrument systematics (Désert et al., 2009) does not confirm the detection. Désert et al. (2011) report the analysis of a second *Spitzer*/IRAC dataset at 3.6 μm using the same detrending technique. The new parameter estimates are significantly different, e.g. 4 σ between the transit depths at the two different epochs. The authors attributed such discrepancies to the effects of stellar variability.

5.3.2 Observations

I reanalysed the two transit observations at 3.6 μm with the pixel-ICA technique. The two observations were performed on 2006 October 31 (ID 30590) and 2007 November 25 (ID 40732).

The first observation consists of 1,936 data points using the stellar readout mode with a frame time of 0.4 s. The interval between consecutive exposures is 8.4 s. The total duration was 4.5 hr: 1.8 hr on the primary transit of the planet, 1.6 hr before, and 1.1 hr after transit.

The second observation consists of 122,880 exposures using the sub-array readout mode with a frame time of 0.1 s. Each set of 64 consecutive frames is followed by a reset time of 2 s. The total duration was 4.5 hr: 1.8 hr on the primary transit of the planet, 1.7 hr before, and 1 hr after transit. For this observation, I binned over 64 frames, in order to have a manageable number of data points, to reduce the random scatter, and to have the same sampling as observation ID 30590.

5.3.3 Analysis

Fixed and free parameters

I assumed the orbital period from Collier Cameron et al. (2010), a circular orbit, and calculated the quadratic limb darkening coefficients for the star (Equation 3.13), using the modified version of ATLAS9 code described in Howarth (2011b). The values of the fixed parameters are reported

in Table 5.2. The other astrophysical parameters, i.e. p, a_R, i and t_{mid}, were kept free in the fitting process, as explained in Section 3.3.5.

P	2.218573 days
e	0
γ_1	7.82118×10^{-2}
γ_2	2.00656×10^{-1}

Table 5.2: Values of the parameters fixed while generating the transit models. The limb darkening coefficients, γ_1 and γ_2, were computed for a star with effective temperature $T_{\rm eff}$ =5000 K, gravity $\log g$ =4.5, mixing-length parameter l/h =1.25, solar abundances.

Choice of the pixel-array

The first step in the analysis is the choice of the pixel light-curves to analyse. This may be influenced by:

- the instrument point response function (PRF), i.e. the measured intensity profile of the star on the detector;
- the noise level of the detector;
- the effective number of significant components to disentangle.

The number of significant components is not known a priori. The ICA code extracts a number of components equal to the number of light-curves that it receives as input. Apart from the collective behaviour common to all the pixel light-curves, each pixel introduces an individual signature. Only if the individual signatures are negligible compared to the collective behaviour it is possible to select enough light-curves to disentangle the significant components. The PRF and the noise level of the detector limit the number of pixels containing potentially useful astrophysical information.

In practice, I considered several arrays of pixels with the stellar centroid at their centers, having dimensions 3×3, 5×5, 7×7, 9×9 and 11×11 pixels. Figure 5.4 shows the corresponding integrated light-curves. The light-curves observed in sub-array mode appear to be less affected by the instrument systematics and less noisy. Within the same observations, the light-curves from different arrays are similar in shape, the 3×3 showing slightly larger systematics. Note that 3 pixels is about the size of the Airy diameter. The mean flux over the 3×3, 5×5, 7×7 and 9×9 light-curves are, respectively, ∼83%, ∼92%, ∼96% and ∼98% of the mean flux over the 11×11 light-curve. As the interest is on the relative flux variation during the transit and not on the absolute stellar photometry, it is not necessary to select an array that fully contains the PSF. Larger arrays may be disfavoured, because they include noisier pixels. Figure 5.5 reports the

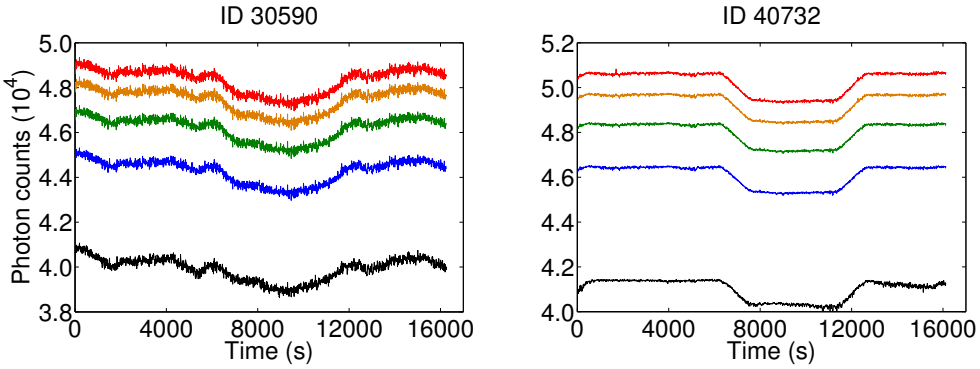

Figure 5.4: Raw integrated light-curves from several squared arrays of pixels: (black) 3×3, (blue) 5×5, (green) 7×7, (orange) 9×9 and (red) 11×11.

transit depth estimates obtained from the different arrays and the corresponding σ_0 and σ_{ICA} values for the two observations, using method 2 (see Section 5.2). The results indicate that:

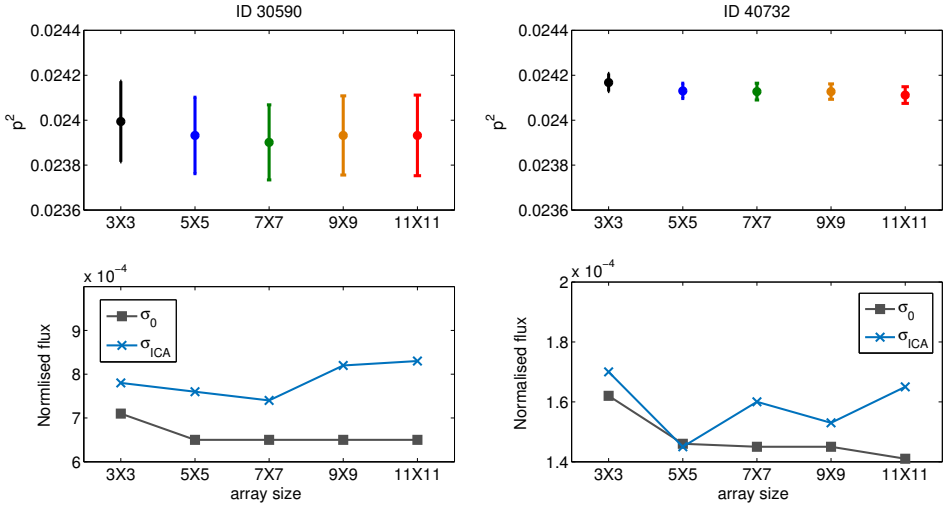

Figure 5.5: Top panels: transit depths obtained from the five arrays considered, using method 2 (see Section5.2), for the observations (left) ID 30590 and (right) ID 40732. Bottom panels: corresponding values of σ_0 and σ_{ICA}.

1. the choice of the array is not crucial for these observations, as the parameter results are consistent well within 1 σ and with similar error bars;

2. the 3×3 arrays appear to be less photometrically stable, as revealed by the higher σ_0;

3. larger arrays tend to have higher σ_{ICA} values, probably due to the inclusion of noisier pixel light-curves in the mixing model;

4. the 5×5 array appears to be the optimal choice.

Outlier rejection

Outliers were identified as points more than 5 σ away from a first transit model (fitted on the original data), and replaced with the mean values of the points immediately before and after. Only one outlier has been found in the observation ID30590, nine in the ID40732.

Choice of the components

Figure 5.6 shows the independent components extracted from the two observations using the 5×5 array. By inspection, a few of the components clearly present time structures, while others

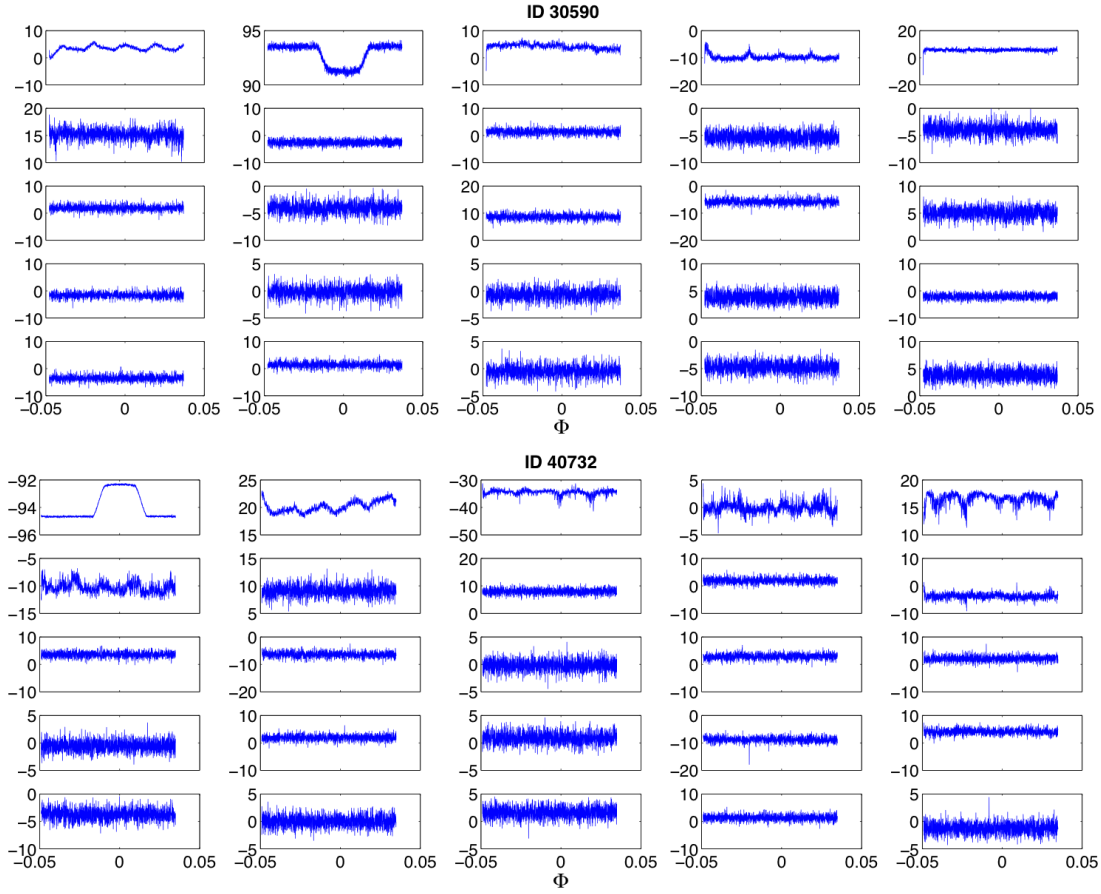

Figure 5.6: Top panel: independent components extracted from observation ID 30590 using the 5×5 array. Bottom panel: the same for observation ID 40732.

appear to be high-frequency components or white noise. I created a ranking of the components, inversely related to the residuals of the single-component fits on the out-of-transit part of the integrated light-curve, then I performed all the fits with the first n components, with $1 \leq n \leq 24$. The results are shown in Figures 5.7 and 5.8. Most systematics are contained in one major component, but the use of multiple components increases the detrending accuracy, up to a saturation point. There is no evidence of an inversion of this trend. For this reason, I decided

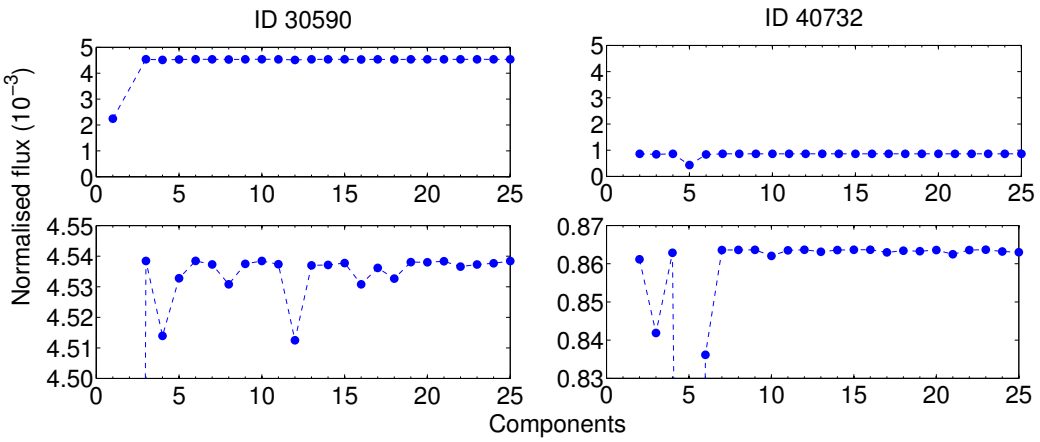

Figure 5.7: Top: standard deviations of the residuals of the single-component fits, normalised to out-of-transit level; 5×5 array. Bottom: the same, zooming on the topmost part of the curve.

to include all the non-transit components in the fitting process.

Other tests: method 1 vs method 2, subdatasets

The results obtained using method 1, i.e. direct identification of the transit component, are consistent with the results obtained using method 2, i.e. subtracting the non-transit components. However, method 1 led to larger error bars by a factor 3–4, mainly due to the σ_{ICA} term.

I tested the effect of considering shorter observations, which I called subdatasets, with different starting and ending times. The scatter in the transit parameters obtained from a long list of subdatasets is $\lesssim$1 σ. This test also confirmed that the results obtained using method 1 are less robust, as suggested by the larger error bars.

5.3.4 Results

Figure 5.9 shows the normalised transit signals extracted using the 5×5 arrays, considering all the independent components; the relative best light-curve fits to the binned and detrended data; and the residuals. The standard deviations of the residuals are $\sigma_0^{ID30590}$ =6.4×10^{-4} and $\sigma_0^{ID40732}$ =1.45×10^{-4}. Note that the signal extracted from observation ID 40732 has a dispersion smaller by a factor ∼4.4. The final parameter results are reported in Table 5.3.

5.3.5 Discussion

The planetary, orbital and stellar parameters derived separately from the two observations, reported in Table 5.3, are all consistent within 1 σ. The difference in transit depth is further decreased by injecting the orbital parameters obtained from the best-quality observation into the other one, with a negligible impact on the fitting residuals, showing that part of the apparent

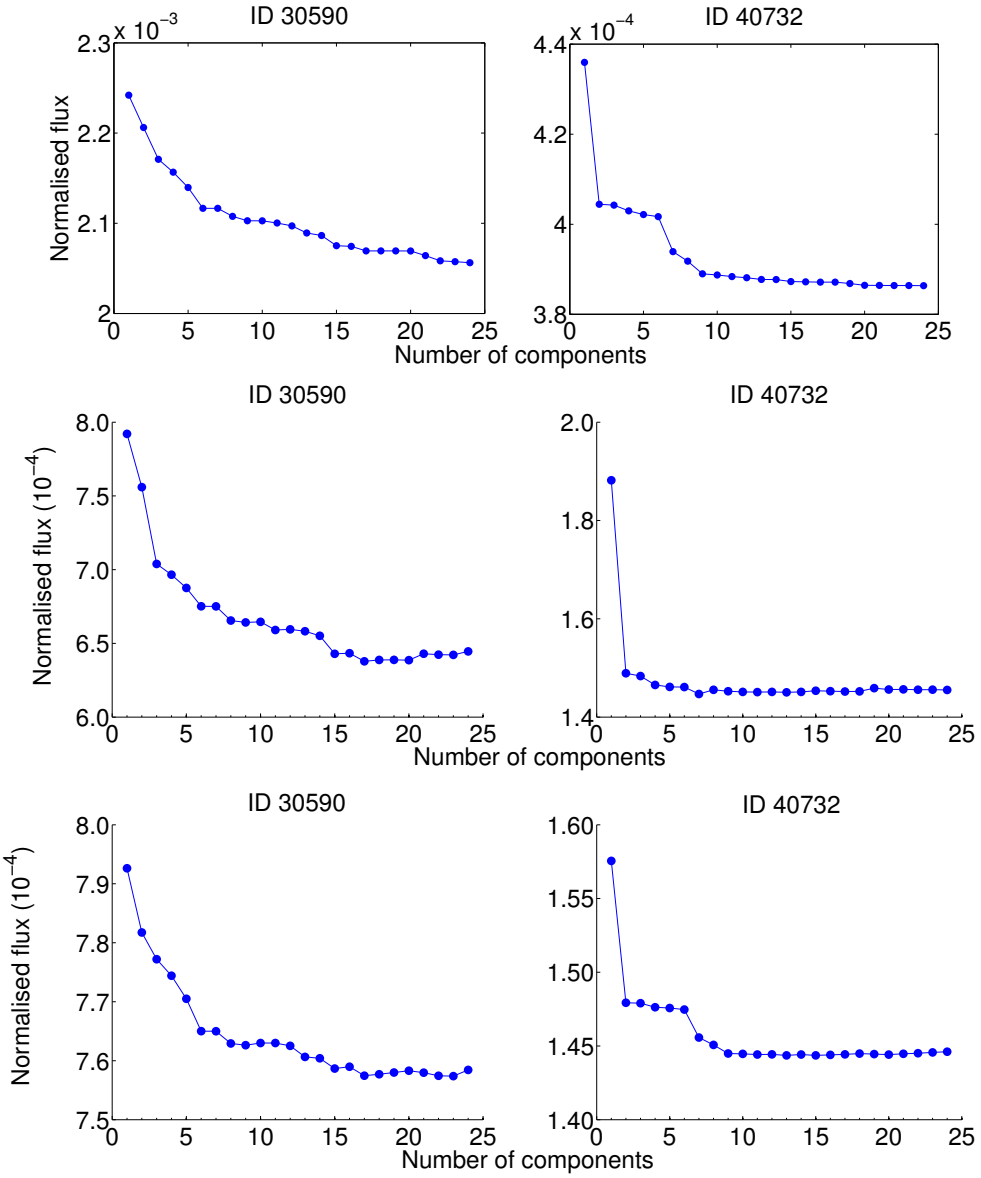

Figure 5.8: Top: standard deviations of the residuals of the fits with multiple components, normalised to out-of-transit level, 5×5 array. Middle: standard deviations of the residuals between the transit signals estimated using method 2 with the n most important components, and the corresponding best model fits, i.e. σ_0. Bottom: σ_{ICA} values using method 2 with the n most important components.

discrepancy was due to the parameter degeneracies. This reanalysis does not support the claims of stellar variability reported in the previous literature (Désert et al., 2009, 2011) and puts an upper limit of one part in $\sim 10^4$ on the overall instrument+astrophysical variability between the two observations one year apart. For the first observation (ID 30590), I obtained larger parameter error bars by a factor $\sim$1.6 compared to the ones reported in Désert et al. (2009). This factor comes from adding the ICA errors to the MCMC error bars based on the fitting residuals only. Désert et al. (2009, 2011) applied parametric corrections for data detrending, without attributing any uncertainties to the detrending processes. I obtained smaller error

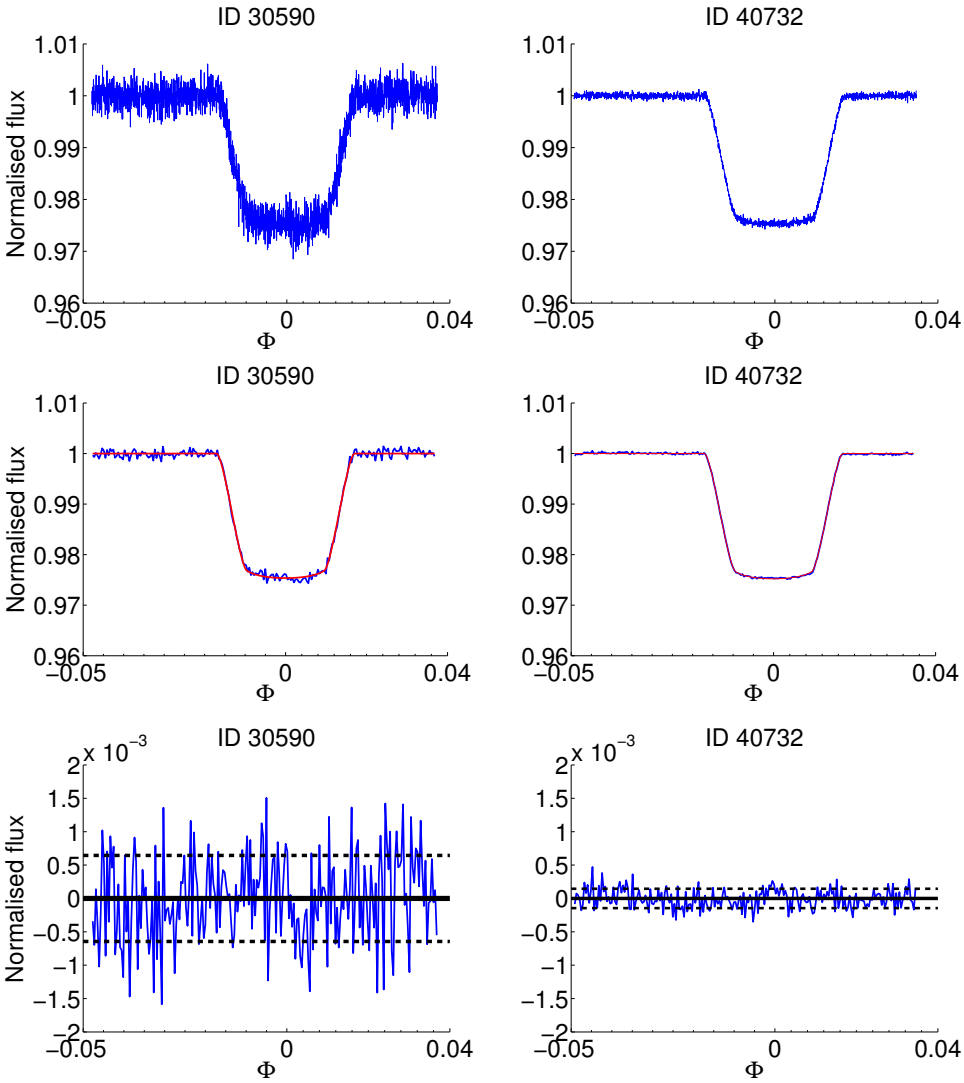

Figure 5.9: Top panel: transit time series extracted using the 5×5 array, method 2 subtracting all the independent components. Middle panel: (blue) the same series, binned by nine points, (red) relative best model fit. Bottom panel: residuals between the extracted time series and the model. Dashed black lines indicate the standard deviations of the residuals.

	ID 30590	ID 40732
p	0.1547±0.0005	0.15534±0.00011
	(0.1551±0.0004)	
a_R	9.05±0.16	8.92±0.03
i	85.93±0.15	85.78±0.03
p^2	0.02394±0.00017	0.02413±0.00003
	(0.02405±0.00014)	
b	0.64±0.03	0.657±0.005
T	5170±200 s	5157±34 s

Table 5.3: Final best parameter values for the exoplanet HD189733b at 3.6 μm. The values in parenthesis are obtained by assuming the same orbital parameters of the best quality observation.

bars for the second observation (ID40732), even including the uncertainties associated with the detrending process. This suggests that, in that context, the blind extraction performed much better than their parametric correction. Finally, I checked that the estimated orbital parameters are consistent within 1 σ with newer measurements at 8 μm reported by Agol et al. (2010). Figure 5.10 compares the various results discussed in this Section.

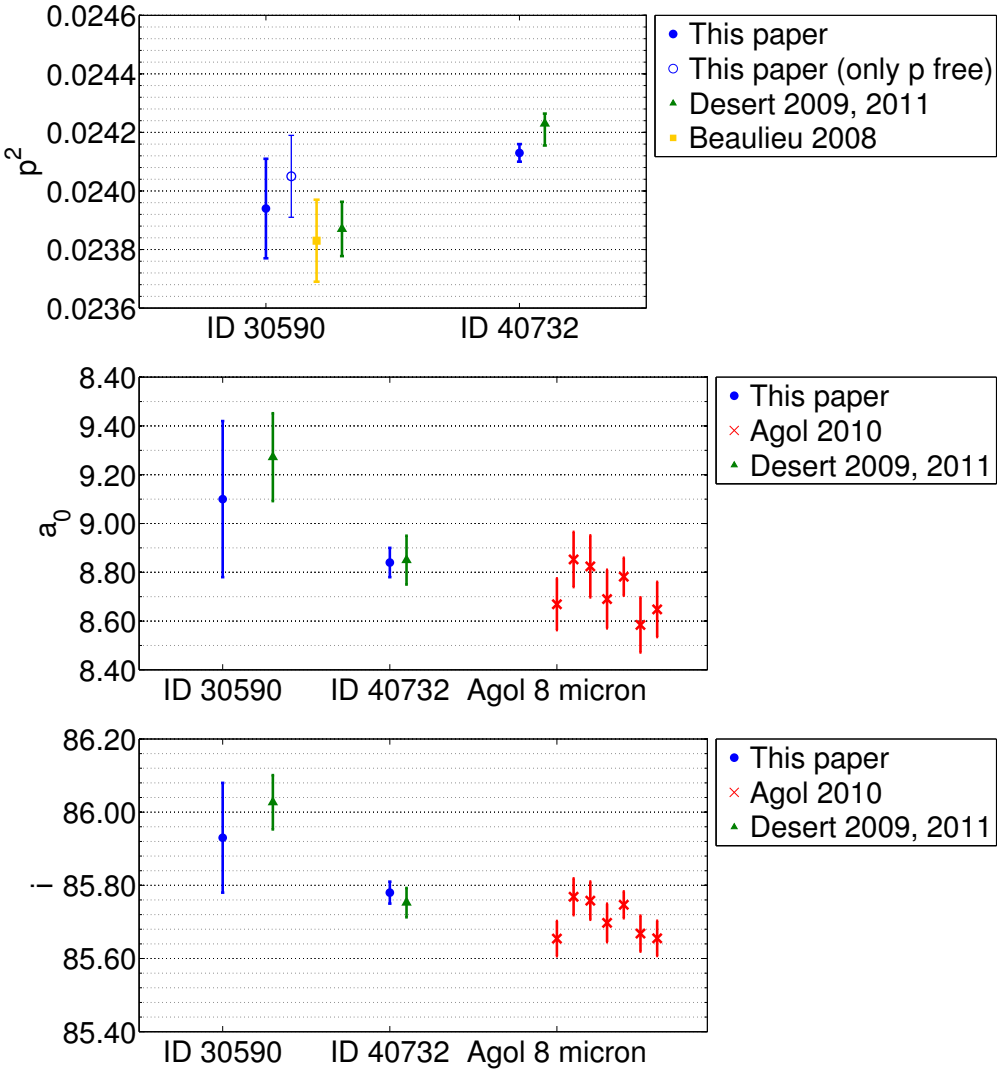

Figure 5.10: Comparison of the parameters p^2, a_R and i, (blue) obtained for HD189733b with the pixel-ICA technique, with the ones reported in (green) Désert et al. (2009, 2011), (yellow) Beaulieu et al. (2008) and (red) observations at 8 μm by Agol et al. (2010). Images from Morello et al. (2014).

5.4 Transits of GJ436b

5.4.1 The exoplanetary system around GJ436

GJ436b is a Neptune-sized planet orbiting around an M dwarf with radius $\sim 0.46 R_{\odot}$ at a distance $\sim$0.03 AU. The apparent magnitude of the host star is $\sim$6.1 in the infrared K band. This planet is interesting for several reasons. It is one of the smallest (radius $\sim 4.3 R_{\oplus}$) and coolest ($\sim$ 700K) exoplanets for which optical–to–IR spectra have been measured (Gillon et al., 2007; Deming et al., 2007; Demory et al., 2007; Alonso et al., 2008; Coughlin et al., 2008; Cáceres et al., 2009; Pont et al., 2009; Ballard et al., 2010b; Stevenson et al., 2010; Beaulieu et al., 2011; Knutson et al., 2011, 2014a). The primary transit depth is $\sim$0.7%. Another peculiarity of GJ436b is its high orbital eccentricity ($e \sim 0.16$), inferred from radial velocity measurements (Maness et al., 2007) and from secondary eclipse phasing (Deming et al., 2007). Both the physical and dynamical properties of GJ436b are debated in the literature.

Maness et al. (2007) and Demory et al. (2007) investigated the origin of the high orbital eccentricity of GJ436b, concluding that the circularization timescale ($\sim 10^8$ yr) is significantly smaller than the age of the system ($\gtrsim 6 \times 10^9$). Maness et al. (2007) also found a long-term trend in radial velocity measurements; they suggested the presence of an external perturber in a wider orbit to explain both the high eccentricity of GJ436b and the trend in radial velocity measurements. Ribas et al. (2008) hypothesized a super-Earth in a close orbit to explain the data, but later retracted. Transit timing variations (TTVs) reported by Alonso et al. (2008) and by Cáceres et al. (2009) do not provide any evidence of external perturbers. Stevenson et al. (2012) claimed the possible detection of two sub-Earth-sized exoplanets transiting in the GJ436 system; according to the authors, the dynamics of the proposed system is consistent with the current non-TTV-detections.

Based on multiwavelength infrared eclipse measurements, Stevenson et al. (2010) proposed a high CO–to–CH_4 ratio compared to thermochemical equilibrium models for hydrogen-dominated atmospheres. Their atmospheric model includes non-equilibrium processes, such as vertical mixing and polymerization of methane, to explain the observed deficiency of CH_4. Beaulieu et al. (2011) suggested strong CH_4 absorption in the 3.6, 4.5, and 8.0 μm *Spitzer*/IRAC passbands from primary transit observations, and their reanalysis of secondary eclipse data is consistent with this detection. Knutson et al. (2011) measured significant time variations of the transit depths at the same wavelengths, which strongly affect the inferred transmission spectrum. They attributed such variations to the stellar activity and found that different results are obtained depending on the observations considered. By rejecting those observations that they believe to be

most strongly affected by stellar activity, their final results support CO as the dominant carbon molecule, with very little, if any, CH_4. More recent *HST*/WFC3 observations in the 1.2–1.6 μm wavelength interval, analyzed by Knutson et al. (2014a), indicate a featureless transmission spectrum, which is consistent with an atmosphere with a high cloud or haze layer.

5.4.2 Observations

I reanalysed two 3.6 and two 4.5 μm transits of GJ436b (program ID 50051) with the pixel-ICA technique. The dates of the observations are detailed in Table 5.4. Each observation consists of

Obs. Number	Detector	Wavelength (μm)	UT Date	Orbit Number
1a	IRAC, ch1	3.6	2009 Jan 9	234
1b	IRAC, ch1	3.6	2009 Jan 28	241
2a	IRAC, ch2	4.5	2009 Jan 17	237
2b	IRAC, ch2	4.5	2009 Jan 31	242

Table 5.4: Spitzer observations of primary transits of GJ436b.

1,829 exposures using IRAC's sub-array mode, taken over 4.3 hr: 0.8 hr on the primary transit of the planet, the remaining 3.5 hr before and after transit. The interval between consecutive exposures is 8.4 s. Each exposure includes 64 consecutive frames integrated over 0.1 s. I replaced the 64 reads of each exposure with their mean values, in order to have a manageable number of data points and to reduce the random scatter.

5.4.3 Analysis

Fixed and free parameters

I assumed the orbital period from Cáceres et al. (2009), the eccentricity and argument of periapsis from Maness et al. (2007). I tested two different sets of quadratic limb darkening coefficients (Equation 3.13), one generated with the modified version of ATLAS9 code (Howarth, 2011b), the other set obtained from a Phoenix stellar model (Allard and Hauschildt, 1995; Allard et al., 2001). The values of the fixed parameters are reported in Table 5.5. The stellar limb darkening coefficients for the two models at the two wavelengths are reported in Table 5.6. The other astrophysical parameters, i.e. p, a_R, i and t_{mid}, were kept free in the fitting process, as explained in Section 3.3.5.

P	2.6438986 days
e	0.16
ω	351°

Table 5.5: Values of the parameters fixed while generating the transit models.

ATLAS	3.6 μm	4.5 μm
γ_1	5.489×10^{-2}	1.331×10^{-2}
γ_2	3.0653×10^{-1}	2.8396×10^{-1}
PHOENIX	3.6 μm	4.5 μm
γ_1	3.87×10^{-3}	3.27×10^{-3}
γ_2	2.3615×10^{-1}	1.8193×10^{-1}

Table 5.6: Limb darkening coefficients for a star with effective temperature $T_{\rm eff}$ =3,680 K, gravity $\log g$ =4.78 and solar abundances.

Choice of the pixel-array

As in the analysis of HD189733b, I adopted a 5×5 array of pixels; the choice of the array is not critical.

Outlier rejection

No outliers have been found in the four datasets.

Choice of the components

As in the analysis of HD189733b, I included all the non-transit components when fitting for the instrument systematics.

New test: subdatasets and test of pixel-phase correlations

To investigate the effectiveness of the data detrending I measured the correlations of the signals with the pixel-phase position, before and after the corrections. The pixel-phase is defined as the distance of the centroid position from the center of the pixel containing the centroid (Fazio et al., 2004; Morales-Calderón et al., 2006). The centroid coordinates are measured using a simple flux-weighted center-of-light method, which is accurate at the level of 0.05 pixels (Ingalls et al., 2014). I refer to the Pearson product–moment correlation coefficient (PCC), defined as:

$$PCC = \frac{cov(X,Y)}{\sigma_X \sigma_Y} \tag{5.5}$$

where $cov(X,Y)$ is the covariance of the signals X and Y, σ_X and σ_Y are the standard deviations. In this context, X and Y are temporal series of fluxes and pixel-phases, shown in Figures 5.11 and 5.12. The PCCs are measured over three intervals, i.e. pre-, in-, and post-transit, where the astrophysical signals are expected to be almost flat [2]. In general $-1\leq$PCC$\leq+1$, where $+1$

[2]I used the following definitions: pre-transit ($\phi < -0.0082$); in-transit (-0.00433 $< \phi <$0.00416); post-transit ($\phi >$0.0082). These have been chosen so that all the transit models obtained during the analysis, modified with no limb darkening, are flat in these three intervals. I checked that other reasonable choices of the limits do not affect this analysis.

is total positive correlation, −1 is total negative correlation, and 0 is no correlation. I found that the data detrending is more effective if the first 450 data points are removed, as shown in Figures 5.13 and 5.14. This corresponds to a time interval of ∼1 hr, which is consistent with the (case-dependent) settling time of the *Spitzer* telescope (see Section 5.1.1).

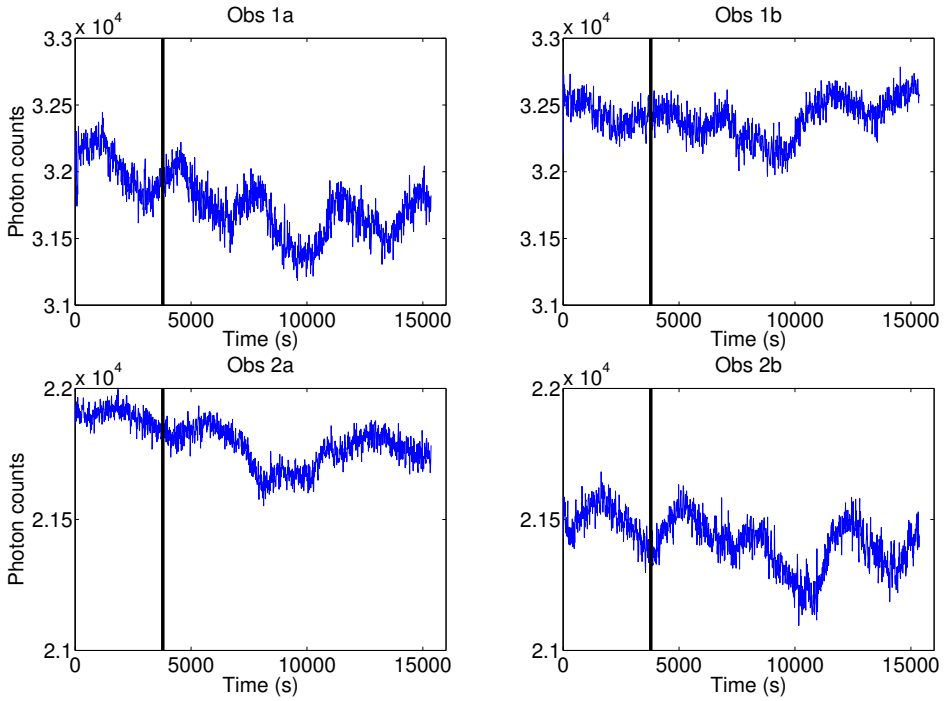

Figure 5.11: Raw integrated light-curves of the four primary transit observations. Data points on the left of the black vertical lines have been discarded for the analysis. Note that the transit depth is comparable with the amplitude of systematics.

5.4.4 Results

Figure 5.15 shows the normalised transit signals, ICA detrended with method 2 (see Section 5.2.1), the relevant best transit models and the residuals. The standard deviations of residuals are $\sim 2\times10^{-4}$ for the observations at 3.6 μm (1a and 1b) and 2.6–2.9$\times10^{-4}$ for the first and second observations at 4.5 μm (2a and 2b), respectively. The transit models obtained with the two sets of limb darkening coefficients are very similar, with average standard deviations $\lesssim 1.9\times10^{-5}$ and maximum discrepancies $\lesssim 10^{-4}$, while the relevant transit parameters are systematically shifted by about ~ 1 σ (see Figure 5.16). The ATLAS model is limited by a lower number of molecular linelists compared to the PHOENIX model, which are relatively important for stars with $T_{\rm eff}$ $\lesssim$4,000 K, as it is the case for GJ436. Hence I select the results obtained with the PHOENIX limb darkening coefficients. In addition to the individual model-fits for each observation, I performed simultaneous fits over the two observations at the same wavelengths with common orbital parameters, to remove the effect of parameter correlations. All the results

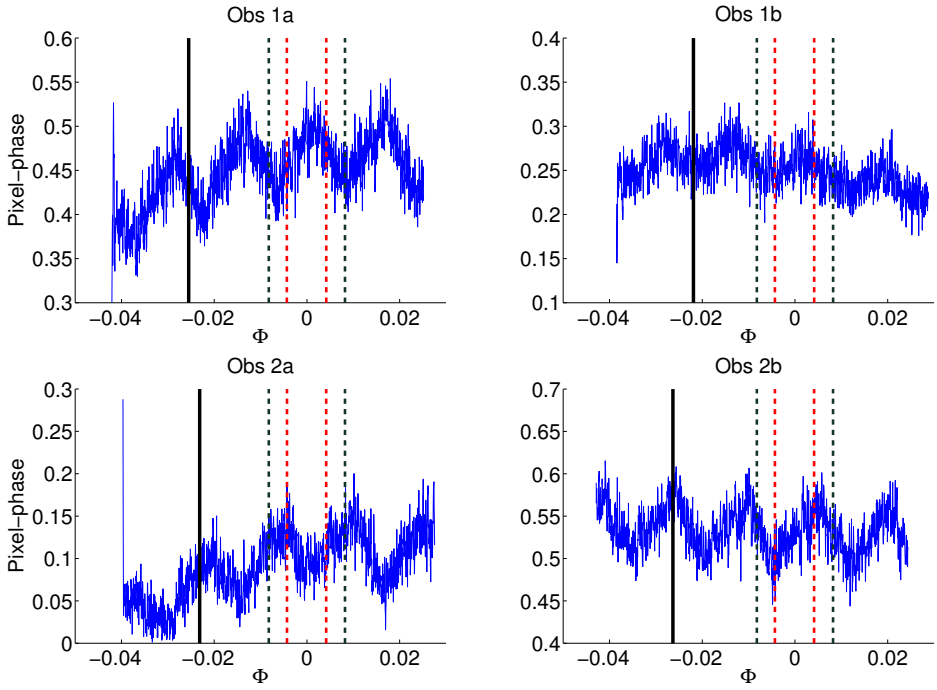

Figure 5.12: Time series of the pixel-phase values for the four observations. Data points on the left of black vertical lines have been discarded for the analysis; dashed green lines delimit the ends of pre-transits and the begins of post-transits; dashed red lines delimit the in-transits.

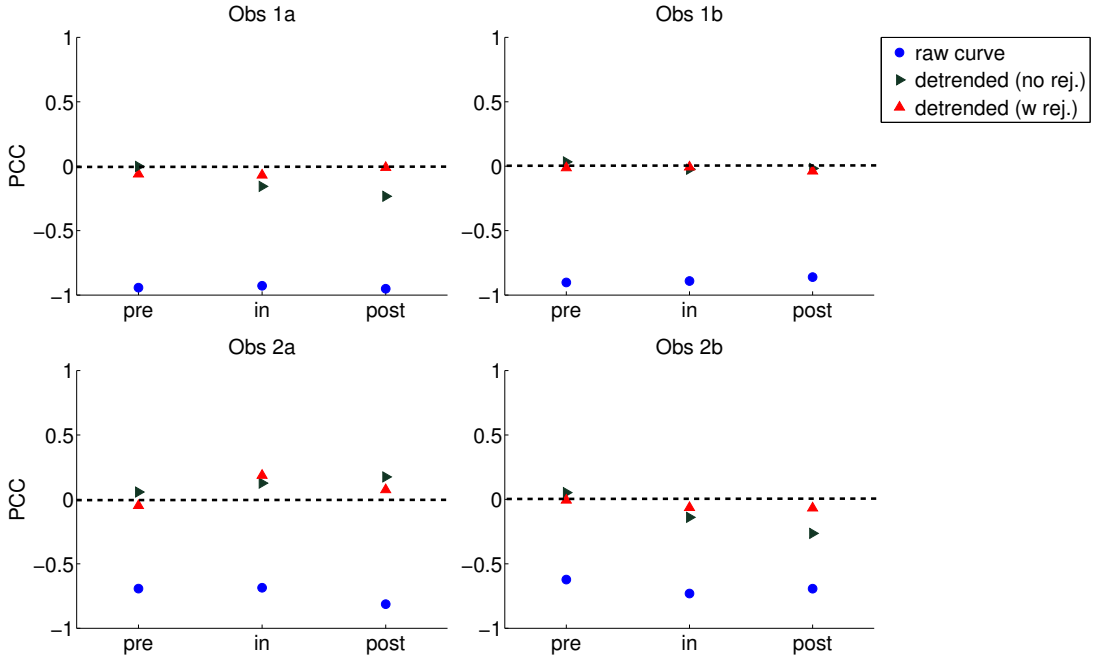

Figure 5.13: PCCs between fluxes and pixel-phases for pre-, in-, and post-transits of the four light-curves; (blu circles) raw data, (green rightwards triangles) ICA detrended data with no rejections, (red upwards triangles) ICA detrended data after rejecting the first 450 points.

are reported in Tables 5.7 and 5.8.

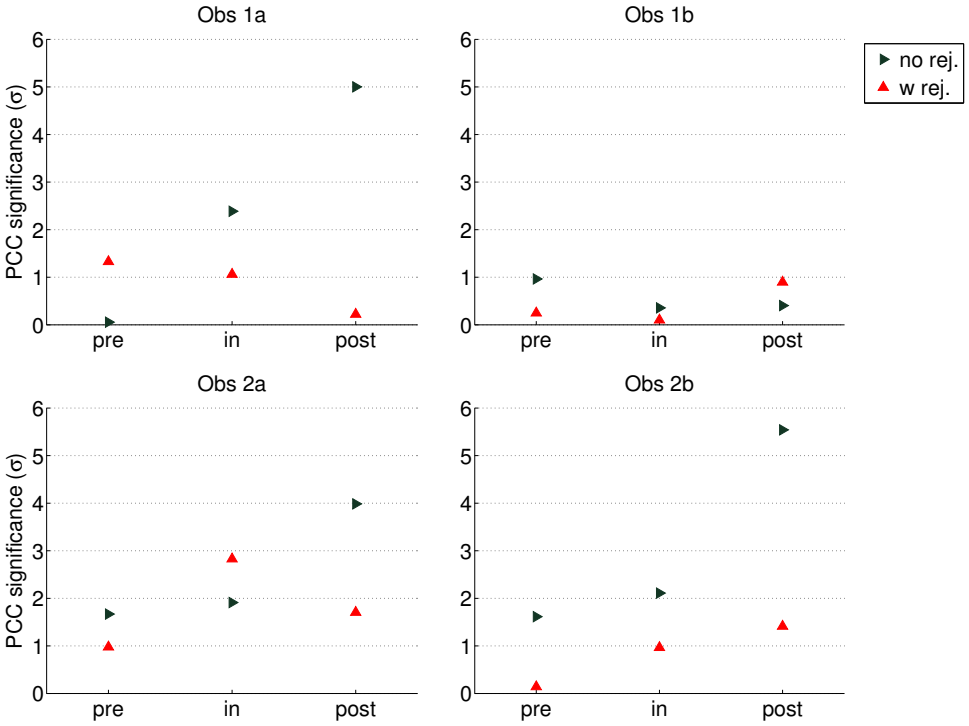

Figure 5.14: Significance level of correlation between fluxes and pixel-phases for the four observations; (green rightwards triangles) ICA detrended data with no rejections, (red upwards triangles) ICA detrended data after rejecting the first 450 points.

	1a	1b	1a+1b
p	0.0828±0.0006	0.0831±0.0005	0.0825±0.0005 / 0.0834±0.0005
a_R	14.0±0.4	13.7±0.3	13.8±0.3
i	86.54±0.15	86.47±0.12	86.49±0.09
p^2	0.00686±0.00010	0.00690±0.00008	0.00681±0.00008 / 0.00696±0.00008
b	0.845±0.011	0.844±0.008	0.845±0.007
T	2805±24 s	2884±20 s	2845±16 s

Table 5.7: Final best parameter values for the exoplanet GJ436b at 3.6 μm.

	2a	2b	2a+2b
p	0.0830±0.0005	0.0836±0.0006	0.0833±0.0005 / 0.0833±0.0005
a_R	14.0±0.4	13.2±0.4	13.6±0.3
i	86.55±0.12	86.27±0.14	86.40±0.09
p^2	0.00688±0.00008	0.00699±0.00010	0.00694±0.00008 / 0.00694±0.00008
b	0.841±0.009	0.861±0.009	0.852±0.006
T	2850±19 s	2832±26 s	2840±16 s

Table 5.8: Final best parameter values for the exoplanet GJ436b at 4.5 μm.

5.4.5 Discussion

Even in this case, the pixel-ICA reanalysis shows more consistent results over the multiple epochs at the same wavelengths compared to the previous results reported in the literature (see Figure 5.16), which were obtained using parametric detrending techniques. All parameters at the mul-

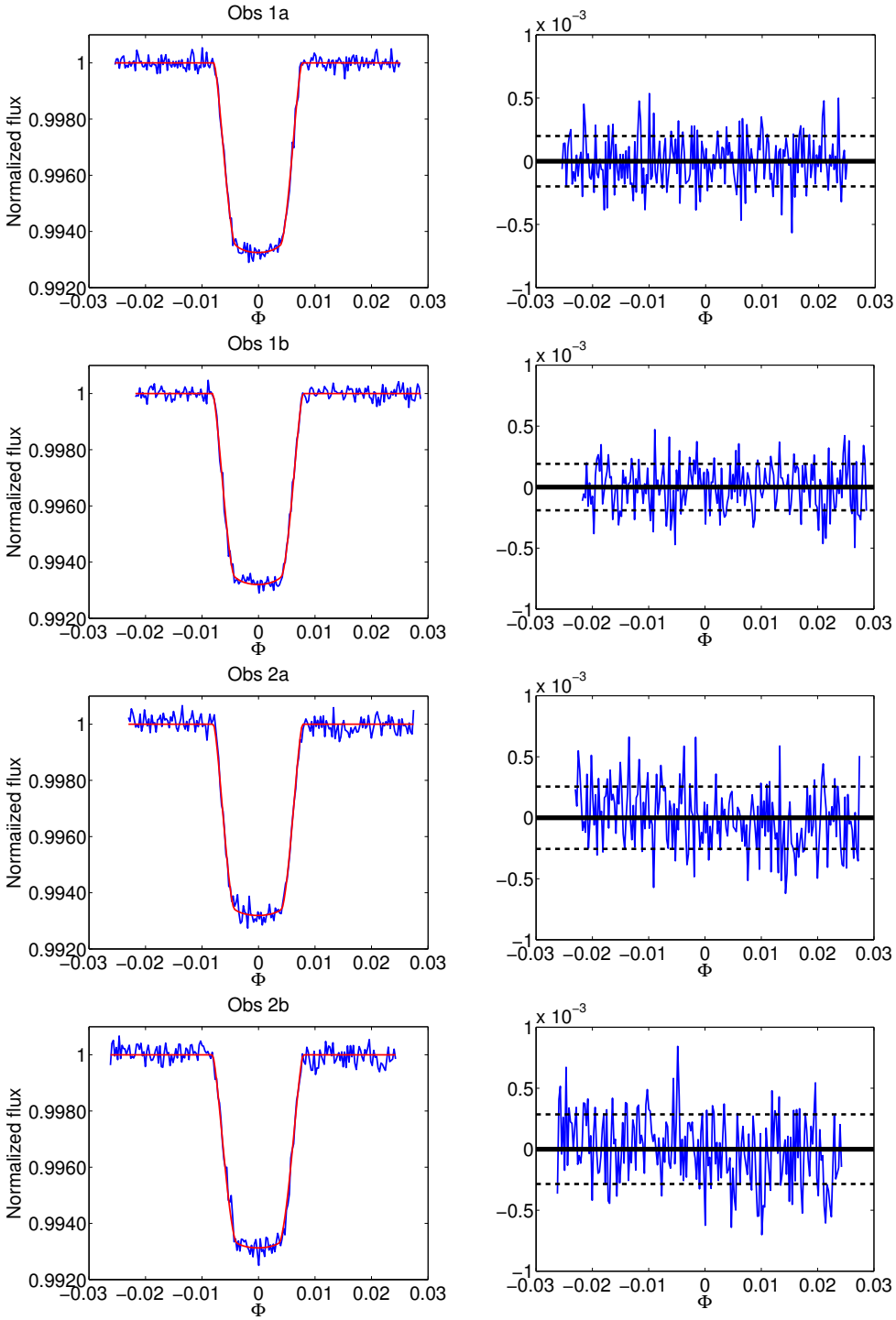

Figure 5.15: Left panels: (blue) detrended light-curves for the four observations with (red) best transit models overplotted, binned over 7 points; best transit models are calculated with p, a_R, and i as free parameters, and Phoenix quadratic limb darkening coefficients (see Section 5.4.3). Right panels: Residuals between detrended light-curves and best transit models; black horizontal dashed lines indicate the standard deviations of residuals.

tiple epochs are consistent within 1 σ, except for the transit durations between the observations 1a and 1b, which are consistent within 2 σ. Although it is a low-significance detection, it may be caused by the presence of an external perturber, as hypothesised by several studies (see Section

5.4.1). The simultaneous fit with common orbital parameters, which forces the transit duration to be the same, gives slightly worse results in the case 1a+1b. The simultaneous fit 2a+2b, instead, strengthens the lack of variations between these two epochs at 4.5 μm. The transit depth variations are below 1 part in 10^4 at both wavelengths, independent on the potential duration variation. Also, no significant differences are detected between the transit depths at 3.6 and

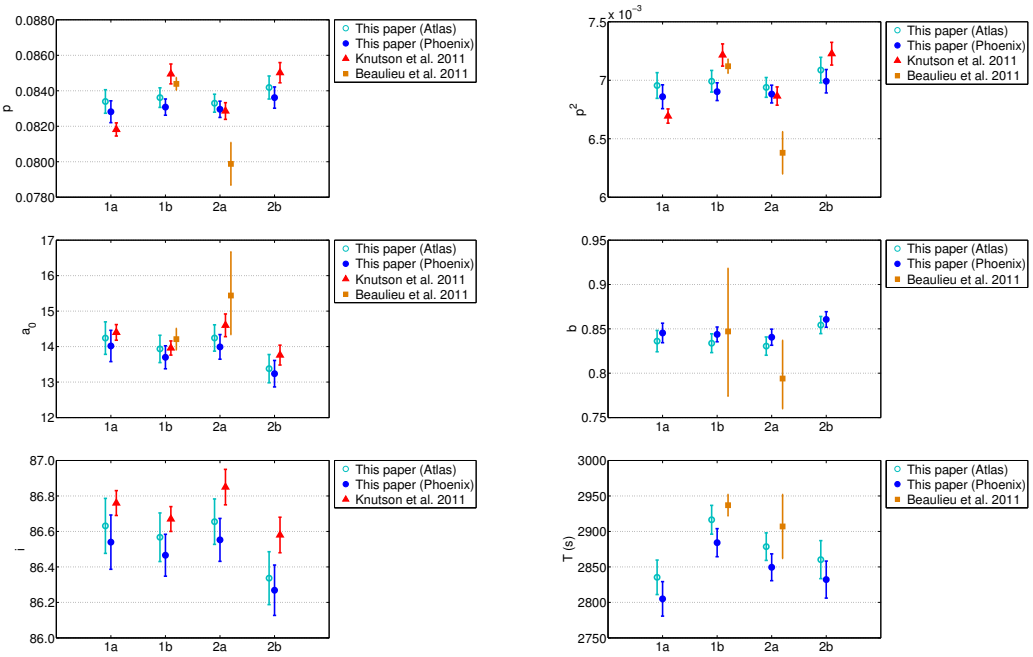

Figure 5.16: From top to bottom: Comparisons of the parameters p, a_R, and i (left side), p^2, b, and T (right side), obtained for GJ436b with the pixel-ICA technique by using Atlas stellar model (cyan, empty circles), Phoenix stellar model (blue, full circles), in Knutson et al. (2011) (red triangles), and in Beaulieu et al. (2011) (yellow squares).

4.5 μm, nor with the recent measurements in the range 1.2–1.6 μm reported in Knutson et al. (2014a), supporting the hypothesis of a flat transmission spectrum (see Figure 5.17).

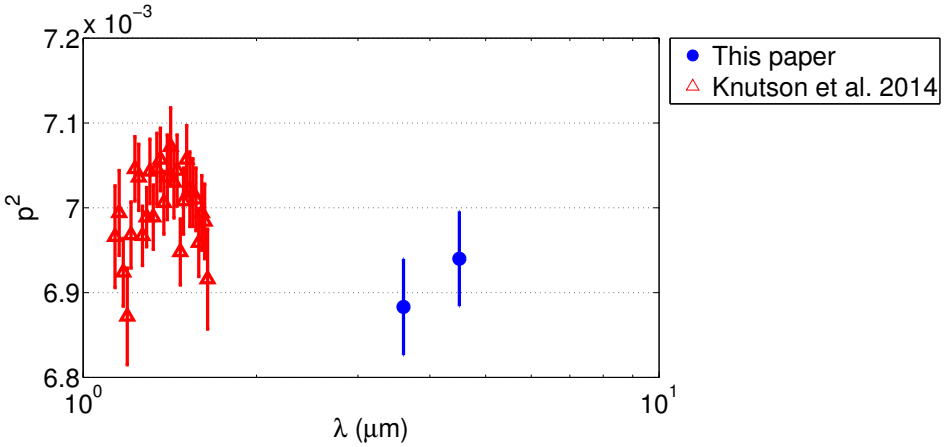

Figure 5.17: Transit depth values obtained in this paper at 3.6 and 4.5 μm (blue circles); values at 1.2–1.6 μm reported by Knutson et al. (2014a) (red triangles).

Chapter 6

Application to simulated photometric data

In this Chapter, I investigate the limits and advantages of pixel-ICA on a series of simulated datasets with different instrument properties, and a range of jitter timescales and shapes, non-stationarity, sudden change points, etc. The content of this chapter has been published in Morello (2015).

6.1 Instrument simulations

6.1.1 Instrument jitter only

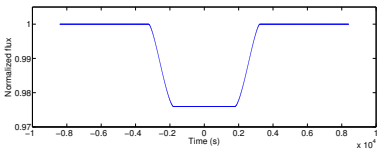

Figure 6.1: Reference transit light-curve adopted in simulations.

I consider an *ideal* transit light-curve with parameters reported in Table 6.1, sampled at 8.4 s over 4.7 hours, totaling 2001 data points, symmetric with respect to the transit minimum. Figure 6.1 shows the ideal light-curve. To each data point I associate a

Table 6.1: Transit parameter values adopted in all simulations: $p = r_p/R_s$ is the ratio of planetary to stellar radii, $a_0 = a/R_s$ is the orbital semimajor axis in units of stellar radius, i is the orbital inclination, e is the eccentricity, P is the orbital period, γ_1 and γ_2 are quadratic limb darkening coefficients (see Equation 3.13).

p	0.15500
a_0	9.0
i	85.80
e	0.0
P	2.218573 days
γ_1, γ_2	0.0, 0.0

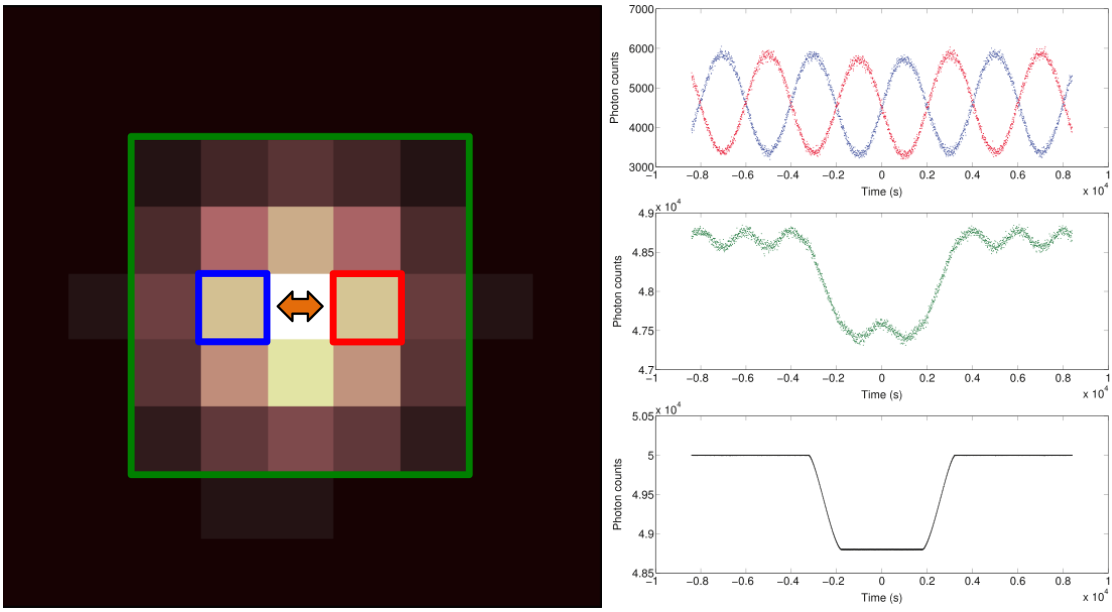

Figure 6.2: Left: Representation of one simulated frame onto the focal plane. Right: simulated time series, in absence of instrument systematics, associated to (top, blue and red)selected individual pixels, (middle, green) a centered 5×5 array, and (bottom, black) a centered 9×9 array. The centroid is assumed oscillating in the direction indicated by the double-headed arrow, with a sinusoidal pattern (sin1, see Tab. 6.2).

number of photons proportional to the expected flux, in particular 50,000 photons in the out-of-transit. I generate random gaussian coordinates for each photon, representing their positions on the detector plane. Finally, I add a grid on this plane: each square of the grid represents a pixel, and the number of photons into a square at any time is the read of an individual pixel in absence of pixel systematics. To simulate the effect of instrumental jitter, I move the gridlines from one data point to another (equivalent to shifting the coordinates of the photons).

Figure 6.2 shows the effect of pure jitter, in absence of other instrument systematics, at different levels, i.e. individual pixels, and small and large clusters. Pixel flux variations are related to the changing position of the PSF: the flux is higher when the center of the PSF is closer to the center of the pixel. The same is valid for the flux integrated over a small aperture, compared to the width of the PSF. Also note that short time-scale fluctuations are present as a sampling effect. Neither of these variations are observed with a large aperture that includes all the photons at any time.

6.1.2 Source Poisson noise

In a real-case scenario, the detected photons from the astrophysical source are distributed according to a Poisson function with fluctuations proportional to the square root of the expected number of photons. The value of the proportionality factor is specific to the instrument. Poisson noise in the source is a natural limitation to the photometric precision that can be achieved for any astrophysical target. To include this effect in the simulations, I added a random time series to the astrophysical model, multiplied by different scaling factors, then generated frames with total number of photons determined by these noisy models.

6.1.3 The effect of pixel systematics

As discussed in Section 5.1.1, *Spitzer*/IRAC datasets for channels 1 and 2 show temporal flux variations correlated to the centroid position, independently of the aperture selected (Fazio et al., 2004; Morales-Calderón et al., 2006). Here I consider two effects that, combined to the instrument jitter, can produce this phenomenon:

1. inter-pixel quantum efficiency variations, simulated by multiplying the photons in a pixel by a coefficient to get the read, the coefficients not being identical for all the pixels;

2. intra-pixel sensitivity variations, simulated by assigning individual coefficients dependent on the position of the photon into the pixel.

6.1.4 Description of simulations

I performed simulations for two values of (gaussian) PSF widths, σ_{PSF}:

- σ_{PSF} =1 p.u. (pixel side units);

- σ_{PSF} =0.2 p.u.

The two sets of frames differ only in the scaling factor in photon coordinates, therefore no relative differences are attributable to the random generation processes. As a comparison, the nominal PSF widths for *Spitzer*/IRAC channels are in the range 0.6–0.8 p.u. (Fazio et al., 2004). By comparing two more extreme cases, I study the impact of the PSF width on pixel systematics and their detrending. I also tested eleven Poisson noise amplitudes, linearly spaced between 0 and $\sqrt{50,000}$. I simulated several jitter time series as detailed in Table 6.2 and Figure 6.3. For each case, I adopted:

1. randomly generated quantum efficiency maps with standard deviations of $\sim 10^{-2}$, to simulate the inter-pixel variations;

Table 6.2: List of jitter time series adopted in simulations and their properties. Six armonics are used to test the ability of detrending periodic signals with different timescales and phasing relative to the transit. The sawtooth time series is more similar to the jitter observed with Spitzer, and its variants test the effects of non-periodicity and monotonic trends. The last configuration test a case of a sudden discontinuity, such as re-pointing of the telescope.

Abbr.	Shape	Peak-to-peak amplitude (p.u.)	Period (s)
sin1	sinusoidal	0.6	4014.6
cos1	cosinusoidal	0.6	4014.6
sin2	sinusoidal	0.6	3011.0
cos2	cosinusoidal	0.6	3011.0
sin3	sinusoidal	0.6	2007.3
cos3	cosinusoidal	0.6	2007.3
saw1	∼sawtooth	0.6	2990.4
saw1v1	∼sawtooth	variable	2990.4
saw1v2	∼sawtooth	variable	2990.4
saw1v3	∼sawtooth	decreasing	2990.4
saw1vf1	∼sawtooth	0.6	variable
saw1vf2	∼sawtooth	0.6	decreasing
jump04c	Heaviside step	0.4	mid-transit discontinuity

2. a non-uniform response function for each pixel, i.e. $1-0.1d$, where d is the distance from the center of the pixel, to simulate the intra-pixel variations.

These values are of the same order as the nominal pixel-to-pixel accuracy of flat-fielding and sub-pixel response for *Spitzer*/IRAC channels 1 and 2 (Fazio et al., 2004), but slightly larger to visualize better their effects. Finally, I add white noise time series at an arbitrary level of 5 counts/pixel/data point for most cases, to simulate high-frequency pixel noise (HFPN), such as dark current and readout noise. It is worth noting that the same quantum efficiency maps and noise time series have been adopted for all the simulations with pixel arrays of the same size, to minimize possible stochastic effects when comparing the results.

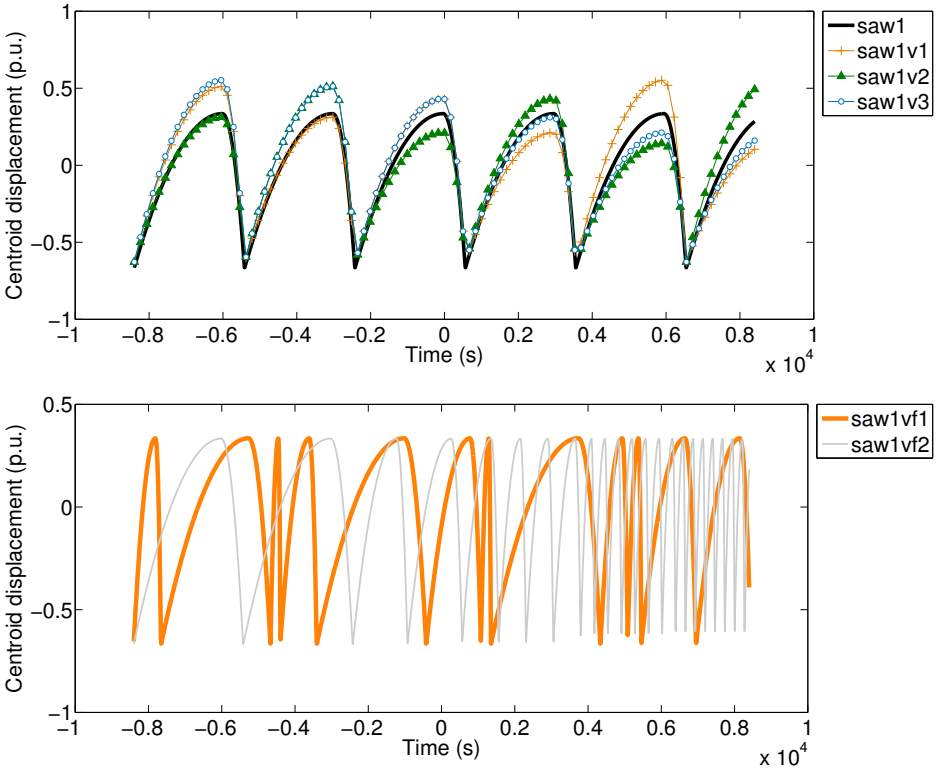

Figure 6.3: Top panel: jitter time series saw1 (black), saw1v1 (ecru, cross markers), saw1v2 (green, triangles), and saw1v3 (cyan, empty circles); markers are represented every 20 data points for reasons of visibility. Bottom panel: jitter time series saw1vf1 (orange), and saw1vf2 (grey). The other jitter time series are not reported, since their representations are obvious (see Table 6.2).

6.2 Results

After having generated the simulated raw datasets, I applied both pixel-ICA and polynomial centroid detrending (PCD) techniques, largely adopted in the literature (e.g. Reach et al., 2005; Charbonneau et al., 2005, 2008; Beaulieu et al., 2008; Knutson et al., 2011), to evaluate their reliability and robustness in those contexts. More specifically, the polynomial decorrelating function adopted by default is:

$$p(x,y) = a_1 + a_2(x-\bar{x}) + a_3(y-\bar{y}) + a_4(x-\bar{x})^2 + a_5(y-\bar{y})^2 \tag{6.1}$$

where x and y are the centroid coordinates, calculated as weighted means of the counts per pixel; $\bar{x}$ and $\bar{y}$ are the mean centroid coordinates on the out-of-transit; and a_i coefficients are fitted on the out-of-transit. In several cases, I tested some variants of PCD, i.e. higher-order polynomials, cross terms, etc.

6.2.1 Zero poissonian noise

Since the main purpose of this Chapter is to test the ability of the pixel-ICA method to detrend instrumental systematics, I first report the detailed results for all the configurations obtained in the limit of zero photon noise. This limit is approximately valid for bright targets such that the variations due to the statistical fluctuations in the number of collected photons are much smaller than the effects of the instrumental systematics. I show in particular:

- the simulated raw light-curves and the corresponding detrended ones;
- the root mean square (rms) of residuals from the theoretical transit light-curve, before and after the detrending processes;
- the residual systematics in the detrended light-curves;
- the planetary, orbital and stellar parameters estimated by fitting the light-curves;
- for a subsample of cases, the results of full parameter retrieval, including error bars.

Case I: inter-pixel effects, large PSF

Figure 6.4 shows the raw light-curves simulated with σ_{PSF} =1 p.u., and inter-pixel quantum efficiency variations over 9×9 array of pixels, and the corresponding detrended light-curves obtained with the pixel-ICA and PCD methods. This array is large enough that the observed

Table 6.3: Root mean square of residuals between the light-curves and the theoretical model for simulations with $\sigma_{PSF} = 1$ p.u., and inter-pixel quantum efficiency variations over 9×9 array of pixels; in particular they are calculated for the raw light-curves, light-curves detrended with the pixel-ICA and PCD methods, binned over 10 points.

Jitter	rms (raw − theoretical)	rms (ICA − theoretical)	rms (PCD − theoretical)
sin1	6.5×10^{-4}	2.0×10^{-4}	3.0×10^{-4}
cos1	6.9×10^{-4}	2.1×10^{-4}	3.2×10^{-4}
sin2	6.7×10^{-4}	2.0×10^{-4}	3.0×10^{-4}
cos2	6.5×10^{-4}	2.1×10^{-4}	3.1×10^{-4}
sin3	6.6×10^{-4}	2.0×10^{-4}	3.0×10^{-4}
cos3	6.6×10^{-4}	2.0×10^{-4}	3.1×10^{-4}
saw1	5.4×10^{-4}	2.1×10^{-4}	3.1×10^{-4}
saw1v1	6.0×10^{-4}	2.1×10^{-4}	3.0×10^{-4}
saw1v2	5.6×10^{-4}	2.1×10^{-4}	3.1×10^{-4}
saw1v3	5.9×10^{-4}	2.1×10^{-4}	3.1×10^{-4}
saw1vf1	5.5×10^{-4}	2.1×10^{-4}	3.0×10^{-4}
saw1vf2	5.3×10^{-4}	2.0×10^{-4}	3.0×10^{-4}
jump04c	6.9×10^{-4}	1.9×10^{-4}	3.0×10^{-4}

modulations are only due to the pixel effects (see Section 6.1.1). Table 6.3 reports the discrepancies between the detrended light-curves and the theoretical model. The amplitude of residuals after PCD detrending, i.e. 3.0×10^{-4} for the selected binning, slightly larger than the HFPN level, i.e. 2.8×10^{-4} for this configuration (see also Section 6.1.4), while for pixel-ICA detrended data it is smaller by a factor $\sim$1/3. It is possible to partially correct for the HFPN, because, after detrending the common non-gaussian components, the individual pixel effects appear as components with mixing coefficients equal to zero for all pixels but one. I note that two independent components are enough to correct for the main instrumental systematics within the HFPN level, the other components slightly correct for the residual pixel systematics. Interestingly, a similar behaviour has been observed for real Spitzer datasets (Morello et al., 2014), but with the best-fit model instead of the (unknown) theoretical one. Figure 6.5 shows how the residuals scale with binning over n points, with $1\leq n \leq10$. This behaviour suggests a high level of temporal structure in the raw data, which is not present in the ICA-detrended light-curves. Some systematics are still detected in residuals obtained with the parametric method. I checked that the empirical centroid coordinates are accurate to within 0.006 p.u. on average, and higher-order polynomial corrections lead to identical results. Figure 6.6 shows the transit parameters retrieved from the detrended light-curves; in a few representative cases, I calculated the error bars as detailed in Morello et al. (2015), and Section 5.2 in this Thesis. Numerical results are reported in Table 6.7.

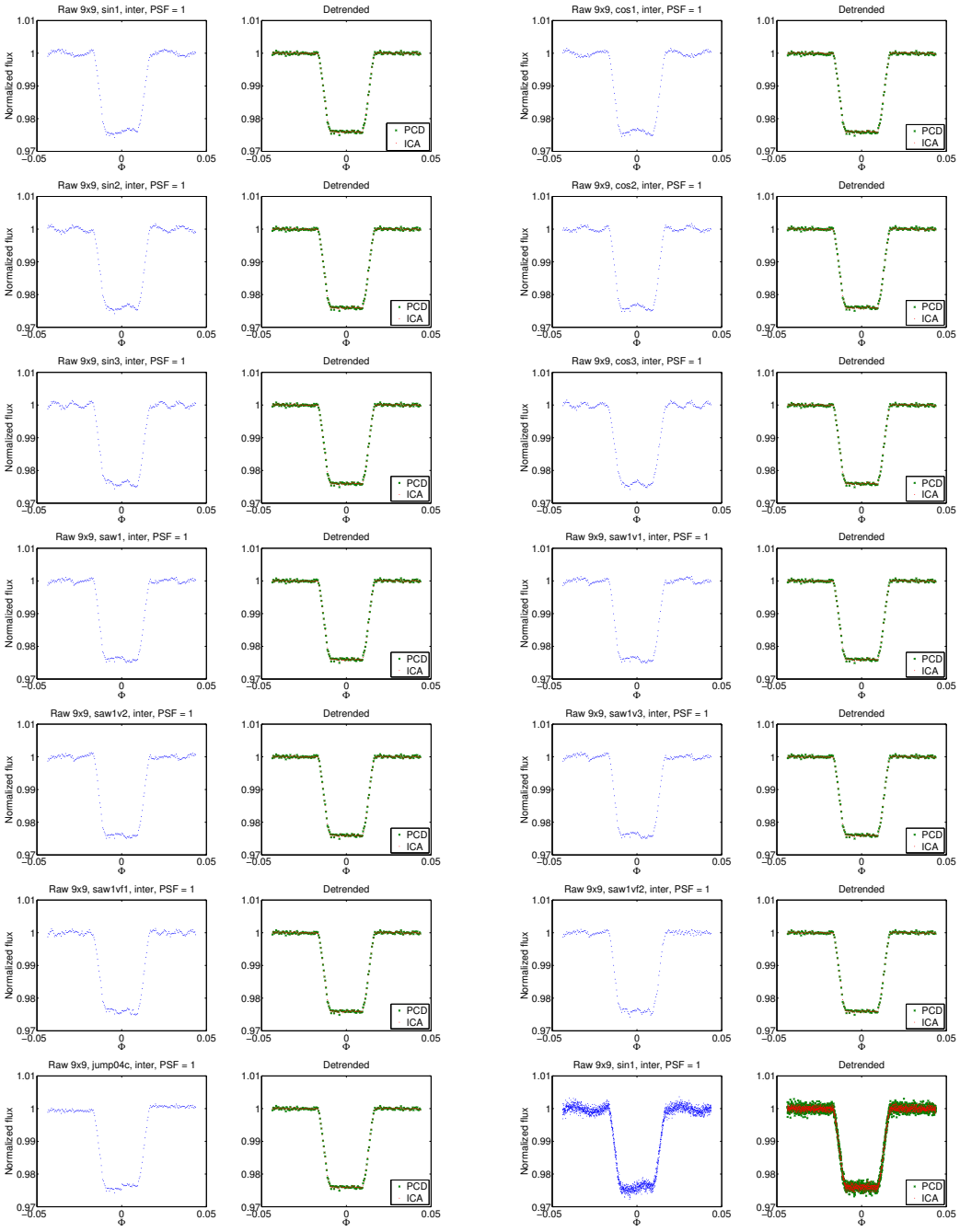

Figure 6.4: Left panels: (blue) raw light-curves simulated with $\sigma_{PSF} = 1p.u.$, and inter-pixel quantum efficiency variations over 9×9 array of pixels. Right panels: detrended transit light-curves obtained with (green 'x') polynomial centroid fitting method, and (red dots) pixel-ICA method. All the light-curves are binned over 10 points, except those in the bottom right, to show a clearer visualization of the systematic effects.

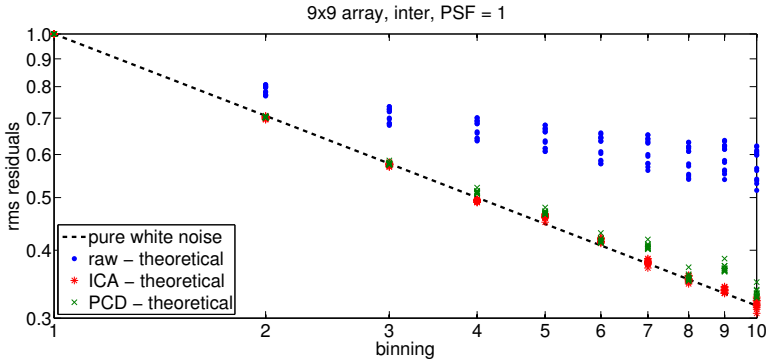

Figure 6.5: Root mean square of residuals for light-curves binned over 1 to 10 points, scaled to their non-binned values. The simulations were obtained with σ_{PSF} =1 p.u., 9×9 array, and inter-pixel effects. The dashed black line indicates the expected trend for white residuals, blue dots are for normalized raw light-curves, red '∗' are for pixel-ICA detrendend light-curves, and green 'x' for PCD detrended light-curves. The spread in points of a given colour represents different jitter models.

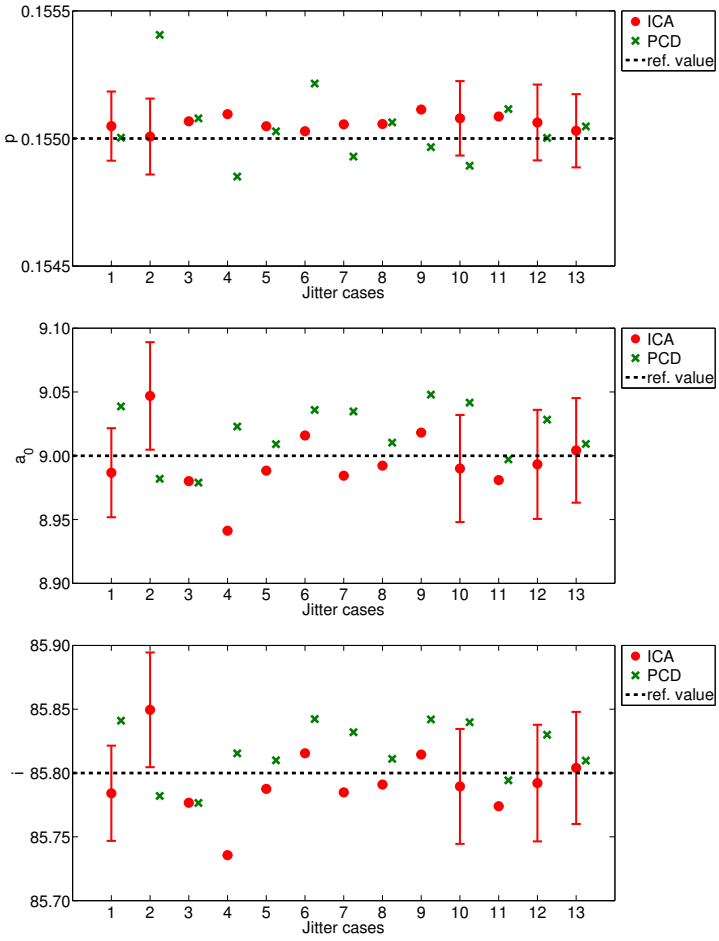

Figure 6.6: Top panel: best estimates of the planet-to-star radii ratio, $p = r_p/R_s$, for detrended light-curves with (red dots) pixel-ICA, and (green x) PCD method (σ_{PSF} =1 p.u., inter-pixel effects over 9×9 array). Error bars are reported for a few representative cases of jitter signal, i.e. sin1, cos1 (chosen as examples of periodic functions with different phasing), saw1v3 (example with non-stationary amplitude), saw1vf2 (non-stationary frequency), and jump04c (sudden change). Middle panel: the same for the orbital semimajor axis in units of the stellar radius, $a_0 = a/R_s$. Bottom panel: the same for the orbital inclination, i.

Table 6.4: Root mean square of residuals between the light-curves and the theoretical model for simulations with $\sigma_{PSF} = 1$ p.u., and inter-pixel quantum efficiency variations over 5×5 array of pixels; in particular they are calculated for the raw light-curves, light-curves detrended with the pixel-ICA and PCD methods, binned over 10 points.

Jitter	rms (raw − theoretical)	rms (ICA − theoretical)	rms (PCD − theoretical)
sin1	1.5×10^{-3}	3.1×10^{-4}	2.6×10^{-4}
cos1	1.4×10^{-3}	3.4×10^{-4}	8.1×10^{-4}
sin2	1.5×10^{-3}	3.2×10^{-4}	2.8×10^{-4}
cos2	1.5×10^{-3}	3.2×10^{-4}	6.2×10^{-4}
sin3	1.5×10^{-3}	3.1×10^{-4}	2.7×10^{-4}
cos3	1.4×10^{-3}	3.2×10^{-4}	4.9×10^{-4}
saw1	1.7×10^{-3}	3.1×10^{-4}	3.5×10^{-4}
saw1v1	1.7×10^{-3}	2.9×10^{-4}	2.5×10^{-4}
saw1v2	1.6×10^{-3}	3.6×10^{-4}	3.7×10^{-4}
saw1v3	1.7×10^{-3}	3.1×10^{-4}	4.0×10^{-4}
saw1vf1	1.7×10^{-3}	3.1×10^{-4}	2.9×10^{-4}
saw1vf2	1.6×10^{-3}	3.2×10^{-4}	2.6×10^{-4}
jump04c	3.3×10^{-3}	2.6×10^{-4}	2.6×10^{-4}

For the same configuration, i.e. σ_{PSF} =1 p.u., inter-pixel effects, I investigated the consequences of considering a smaller array (5×5), which does not include the whole PSF. Figure 6.7 shows the raw light-curves, and the corresponding detrended ones, obtained with the two methods. Table 6.4 reports the discrepancies between those light-curves and the theoretical model. The discrepancies are higher than for the larger pixel-array by a factor $\gtrsim 2$ (for the raw light-curves), because of the additional effect. After pixel-ICA detrending, the discrepancies are reduced by a factor ∼5 (for the selected binning) in most cases, and ∼13 for the 'jump04c' (mid-transit discontinuity), while the performances of the parametric method are case-dependent, and discrepancies are reduced by a factor between 2 and 7 in most cases, and also ∼13 for 'jump04c'. In all cases, the final discrepancies are higher than the HFPN level, i.e. $\sim1.7\times10^{-4}$ for the 5×5 array. Figure 6.8 shows how the residuals scale for binning over n points, with $1\leq n \leq10$. The temporal structure due to jitter effects is dominant in raw data, but little traces of this behaviour are present after pixel-ICA detrending. Even for this aspect, the performances of the parametric method are case-dependent. Figure 6.9 shows the transit parameters retrieved from detrended light-curves; in a few representative cases, I calculated the error bars. Numerical results are reported in Table 6.8. In conclusion, the choice of a non-optimal pixel array introduces additional systematics that worsen the parameter retrieval, but it is quite remarkable that the pixel-ICA technique gives consistent results in most cases, whereas the parametric technique appears to be less robust. In general, the photometric aperture is not necessarily an array of pixels. In fact, it is possible to integrate the flux, e.g., over a circular aperture and use the time series from the pixels at least partially contained within the aperture as input for the ICA. Such options can be

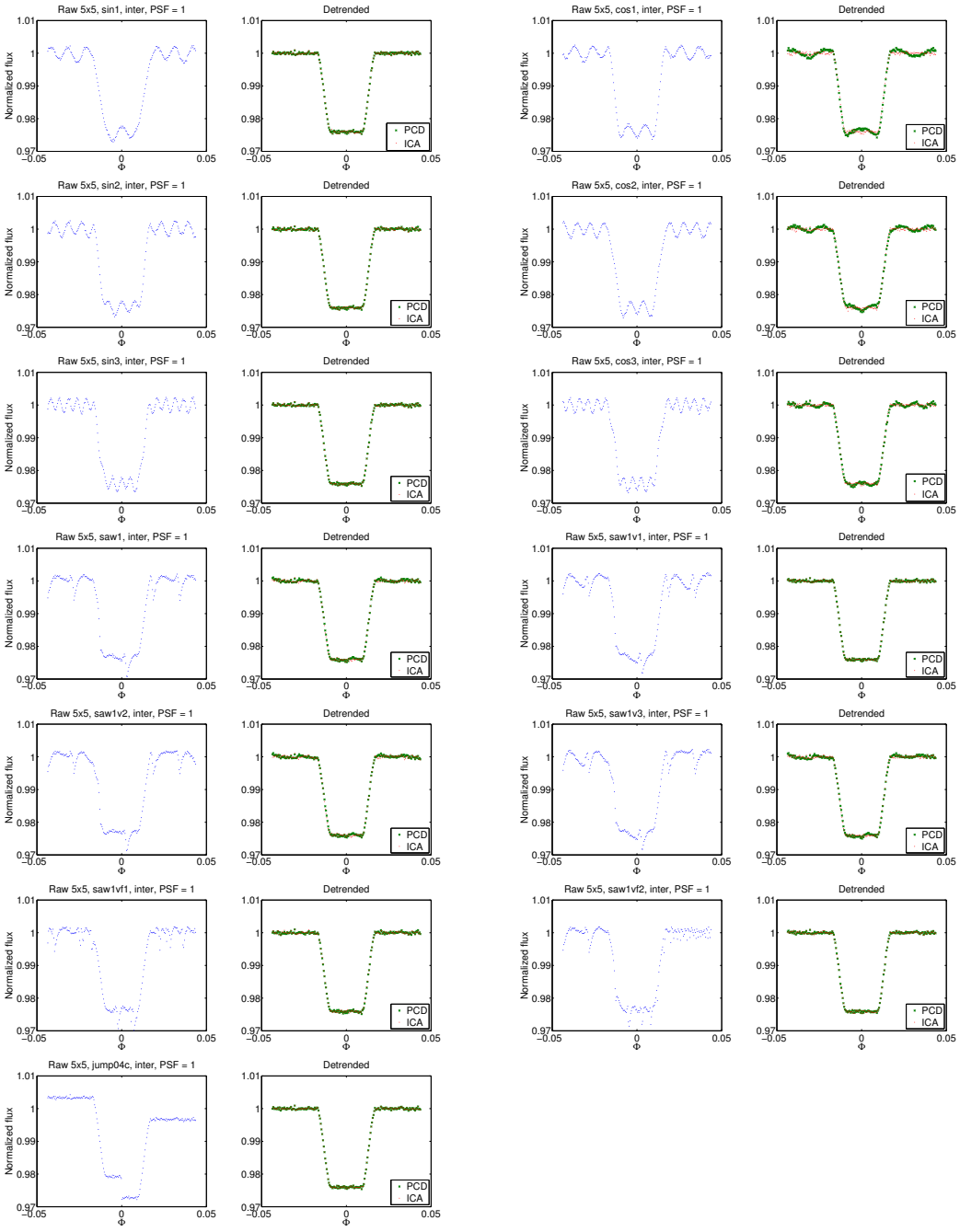

Figure 6.7: Left panels: (blue) raw light-curves simulated with $\sigma_{PSF} = 1p.u.$, and inter-pixel quantum efficiency variations over 5×5 array of pixels. Right panels: detrended transit light-curves obtained with (green 'x') polynomial centroid fitting method, and (red dots) pixel-ICA method. All the light-curves are binned over 10 points to show a clearer visualization of the systematic effects.

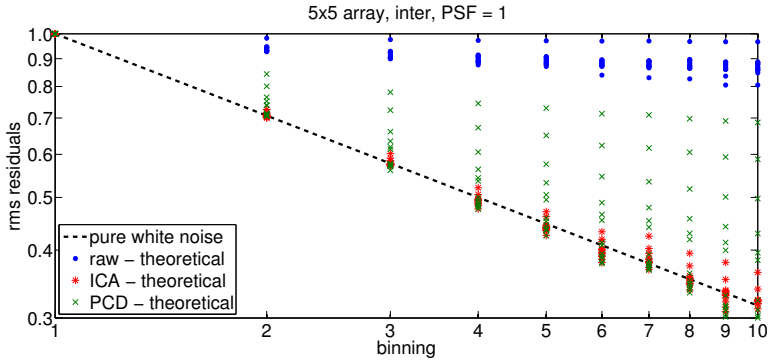

Figure 6.8: Root mean square of residuals for light-curves binned over 1 to 10 points, scaled to their non-binned values. The simulations were obtained with σ_{PSF} =1 p.u., 5×5 array, and inter-pixel effects. The dashed black line indicates the expected trend for white residuals, blue dots are for normalized raw light-curves, red '$*$' are for pixel-ICA detrendend light-curves, and green 'x' for PCD detrended light-curves.

important in cases where the choice of the aperture is critical to maximize the Signal-to-Noise ratio. A detailed analysis of different methods to select an optimal aperture is beyond the scope of this study.

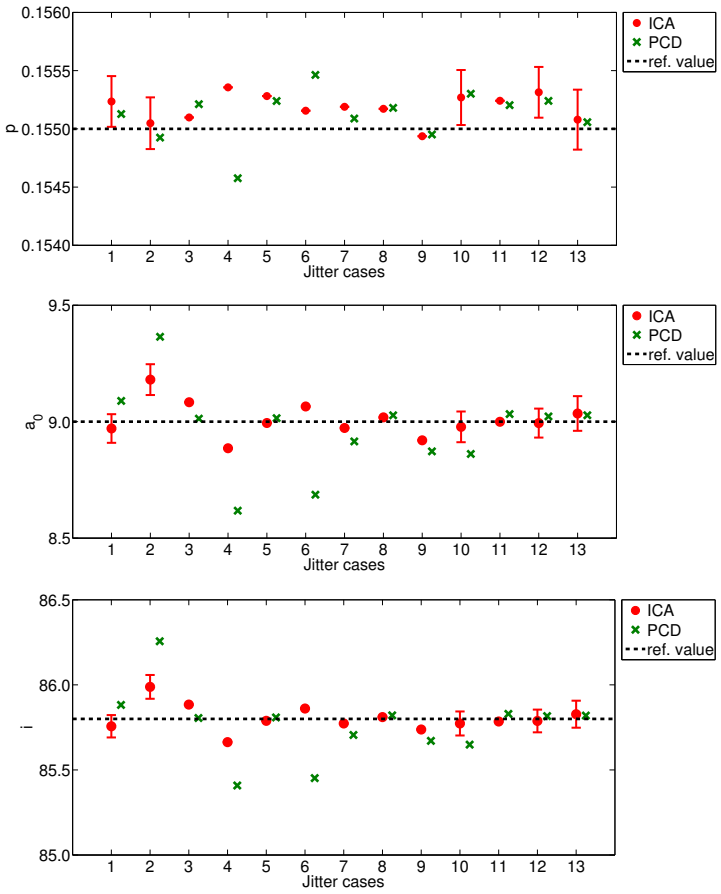

Figure 6.9: Top panel: best estimates of the planet-to-star radii ratio, $p = r_p/R_s$, for detrended light-curves with (red dots) pixel-ICA, and (green 'x') PCD method (σ_{PSF} =1 p.u., inter-pixel effects over 5×5 array). Error bars are reported for representative cases of jitter signal, i.e. sin1, cos1, saw1v3, saw1vf2, and jump04c. Middle panel: the same for the orbital semimajor axis in units of the stellar radius, $a_0 = a/R_s$. Bottom panel: the same for the orbital inclination, i.

Table 6.5: Root mean square of residuals between the light-curves and the theoretical model for simulations with σ_{PSF} =0.2 p.u., and inter-pixel quantum efficiency variations over 5×5 array of pixels; in particular they are calculated for the raw light-curves, light-curves detrended with the pixel-ICA and PCD methods, binned over 10 points.

Jitter	rms (raw − theoretical)	rms (ICA − theoretical)	rms (PCD − theoretical)
sin1	7.2×10^{-4}	7.2×10^{-5}	1.9×10^{-4}
cos1	7.0×10^{-4}	7.7×10^{-5}	2.8×10^{-4}
sin2	7.1×10^{-4}	7.4×10^{-5}	1.8×10^{-4}
cos2	7.4×10^{-4}	7.4×10^{-5}	2.4×10^{-4}
sin3	7.1×10^{-4}	7.8×10^{-5}	1.8×10^{-4}
cos3	7.0×10^{-4}	7.5×10^{-5}	2.0×10^{-4}
saw1	2.6×10^{-4}	6.7×10^{-5}	1.5×10^{-4}
saw1v1	2.3×10^{-4}	6.8×10^{-5}	1.5×10^{-4}
saw1v2	2.3×10^{-4}	6.6×10^{-5}	1.5×10^{-4}
saw1v3	2.3×10^{-4}	6.8×10^{-5}	1.5×10^{-4}
saw1vf1	2.3×10^{-4}	6.6×10^{-5}	1.5×10^{-4}
saw1vf2	2.4×10^{-4}	6.8×10^{-5}	1.5×10^{-4}
jump04c	7.6×10^{-4}	7.4×10^{-5}	1.5×10^{-4}

Case II: inter-pixel effects, narrow PSF

Figure 6.10 shows the raw light-curves simulated with σ_{PSF} =0.2 p.u., and inter-pixel quantum efficiency variations over 5×5 array of pixels, and the corresponding detrended light-curves obtained with the pixel-ICA and PCD techniques. The array is large enough that observed modulations are due only to the pixel effects. Table 6.5 reports the discrepancies between those light-curves and the theoretical model. Again, the discrepancies after pixel-ICA detrending are below the HFPN level, i.e. 1.5×10^{-4} for the selected binning, outperforming the parametric method by a factor 2 to 3. I also note that the empirical centroid coordinates may differ from the "true centroid coordinates" up to 0.15–0.33 p.u., which is an error comparable with the jitter amplitude. This is not surprising, given that the PSF is undersampled, being much narrower than the pixel size. Despite the large errors in empirical centroid coordinates, in some cases, the discrepancies between PCD detrended light-curves and the theoretical model are at the HFPN level, and slightly larger in other cases. Figure 6.11 shows how the residuals scale for binning over n points, with $1\leq n \leq10$. A significant temporal structure is present in the raw data, but not in the pixel-ICA detrended light-curves, while the performances of the parametric method are case-dependent. Figure 6.12 shows the transit parameters retrieved from detrended light-curves; in representative cases, I calculated the error bars. Numerical results are reported in Table 6.9.

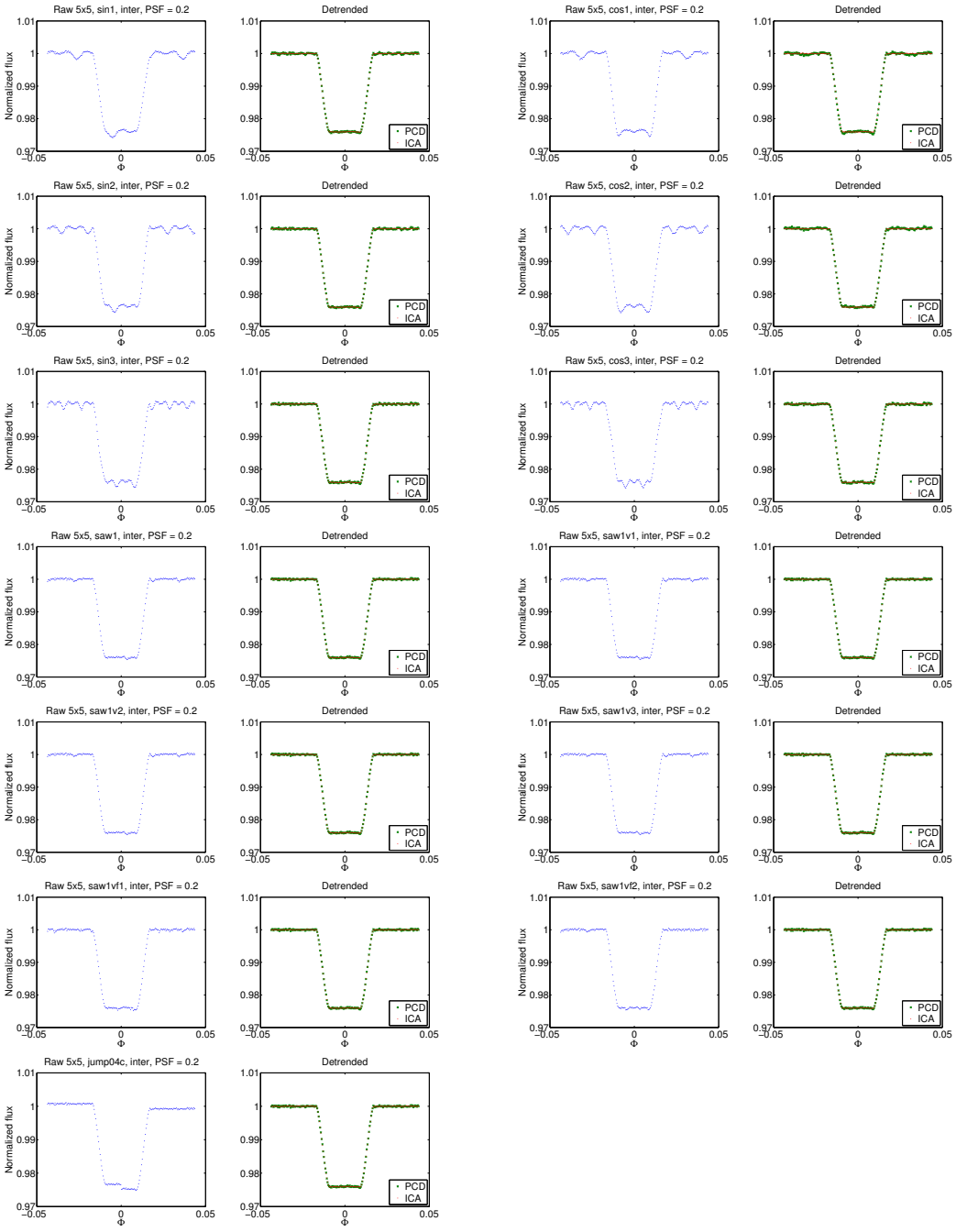

Figure 6.10: Left panels: (blue) raw light-curves simulated with σ_{PSF} =0.2 p.u., and inter-pixel quantum efficiency variations over 5×5 array of pixels. Right panels: detrended transit light-curves obtained with (green 'x') polynomial centroid fitting method, and (red dots) pixel-ICA method. All the light-curves are binned over 10 points to show a clearer visualization of the systematic effects.

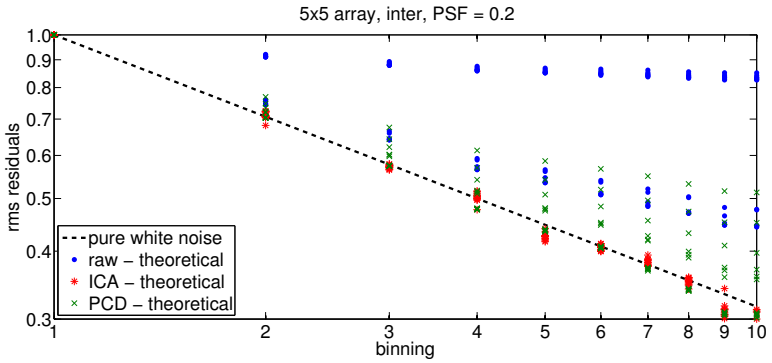

Figure 6.11: Root mean square of residuals for light-curves binned over 1 to 10 points, scaled to their non-binned values. The simulations were obtained with σ_{PSF} =0.2 p.u., 5×5 array, and inter-pixel effects. The dashed black line indicates the expected trend for white residuals, blue dots are for normalized raw light-curves, red '$*$' are for pixel-ICA detrendend light-curves, and green 'x' for PCD detrended light-curves.

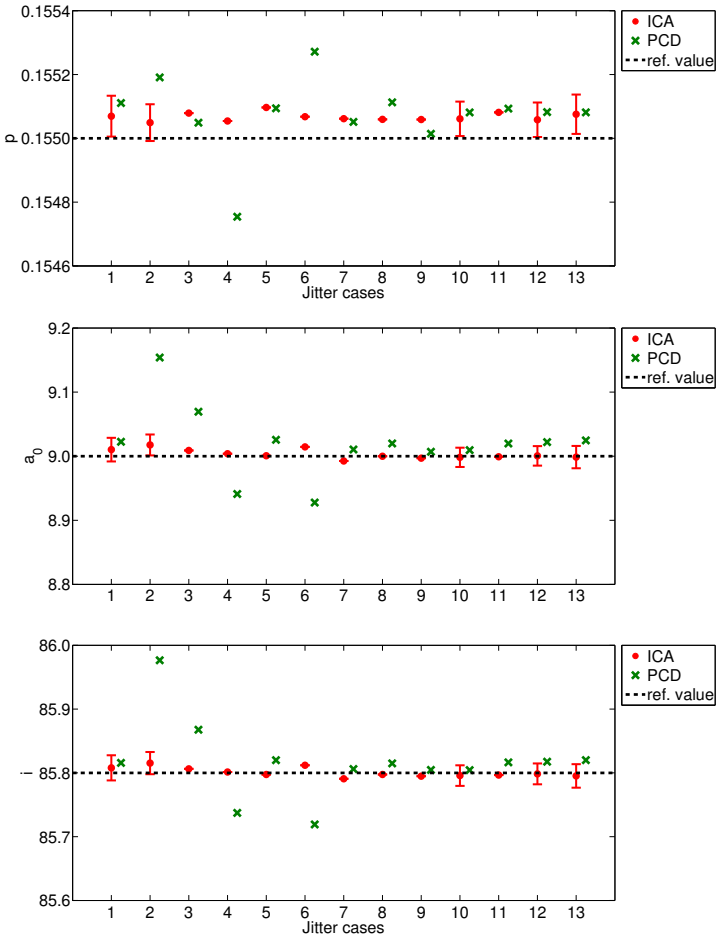

Figure 6.12: Top panel: best estimates of the planet-to-star radii ratio, $p = r_p/R_s$, for detrended light-curves with (red dots) pixel-ICA, and (green 'x') PCD method (σ_{PSF} =0.2 p.u., inter-pixel effects over 5×5 array). Error bars are reported for representative cases of jitter signal, i.e. sin1, cos1, saw1v3, saw1vf2, and jump04c. Middle panel: the same for the orbital semimajor axis in units of the stellar radius, $a_0 = a/R_s$. Bottom panel: the same for the orbital inclination, i.

Case III: intra-pixel effects

For simulations with σ_{PSF} =1 p.u., the effect of intra-pixel sensitivity variations is negligible, i.e. $\sim 10^{-5}$, unless we consider unphysical or very unlikely cases, where the quantum efficiency can assume both positive and negative values in a pixel, or is zero for a significant fraction of the area of the pixel. Intra-pixel effects become significant when the PSF is narrower; therefore, I analyzed only the relevant simulations with σ_{PSF} =0.2 p.u.

Figure 6.13 shows the raw light-curves simulated with σ_{PSF} =0.2 p.u. and intra-pixel quantum efficiency variations over 5×5 array of pixels, and the corresponding detrended light-curves. The array is large enough that the observed modulations are only due to the pixel effects. Table 6.6 reports the discrepancies between those light-curves and the theoretical model. The pixel-ICA technique reduces the dicrepancies by a factor 4 to 8 (for the selected binning) for the first 12 jitter series, and by a factor 83 for the case 'jump04c', outperforming the parametric method by a factor 2 to 4. Figure 6.14 shows how the residuals scale for binning over n points, with $1 \leq n \leq 10$. In this case, the temporal structure is preserved in all detrended light-curves, except for the case 'jump04c', which means that both methods have some troubles to decorrelate intra-pixel effects. Figure 6.15 shows the transit parameters retrieved from detrended light-curves; in representative cases, I calculated the error bars. Detailed numerical results are reported in Table 6.10. While in some cases the parametric method may perform better than pixel-ICA if adopting higher order polynomials, in some other cases higher order polynomials lead to worse results than lower order polynomials. Higher-order polynomials might approximate better the out-of-transit baseline, but the residuals to the theoretical light-curve are not necessarily improved, hence the correction can bias the astrophysical signal. The pixel-ICA method is less case-dependent. It is quite remarkable that, although the systematics are not well decorrelated, the parameter retrieval gives the correct results within the error bars.

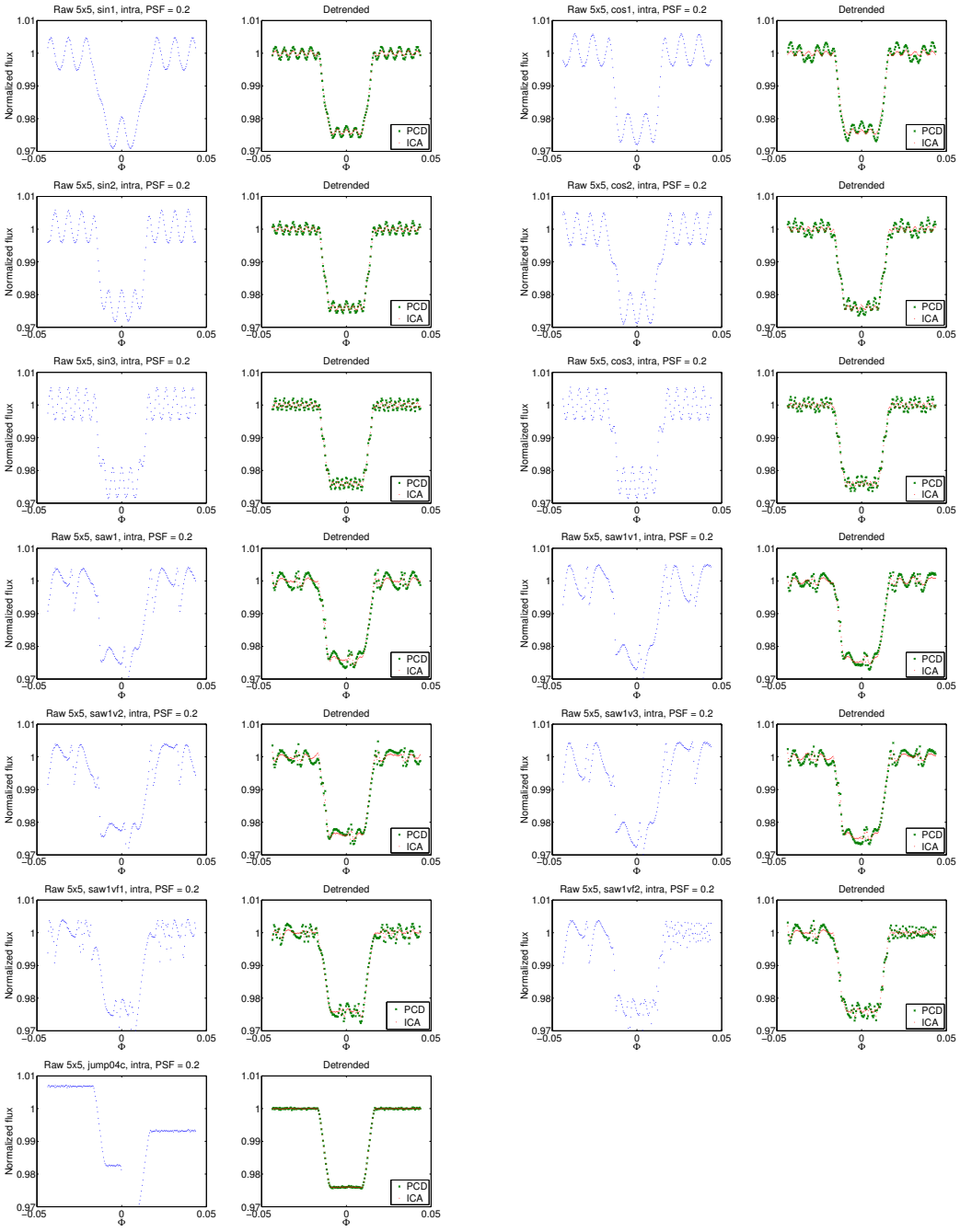

Figure 6.13: Left panels: (blue) raw light-curves simulated with σ_{PSF} =0.2 p.u., and intra-pixel quantum efficiency variations over 5×5 array of pixels. Right panels: detrended transit light-curves obtained with (green 'x') polynomial centroid fitting method, and (red dots) pixel-ICA method. All the light-curves are binned over 10 points to show a clearer visualization of the systematic effects.

Table 6.6: Root mean square of residuals between the light-curves and the theoretical model for simulations with $\sigma_{PSF} = 0.2$ p.u., and intra-pixel quantum efficiency variations over 5×5 array of pixels; in particular they are calculated for the raw light-curves, light-curves detrended with the pixel-ICA and PCD methods, binned over 10 points.

Jitter	rms (raw − theoretical)	rms (ICA − theoretical)	rms (PCD − theoretical)
sin1	3.5×10^{-3}	5.1×10^{-4}	1.2×10^{-3}
cos1	3.5×10^{-3}	5.1×10^{-4}	1.8×10^{-3}
sin2	3.4×10^{-3}	4.9×10^{-4}	1.2×10^{-3}
cos2	3.5×10^{-3}	5.0×10^{-4}	1.5×10^{-3}
sin3	3.4×10^{-3}	5.0×10^{-4}	1.2×10^{-3}
cos3	3.4×10^{-3}	5.0×10^{-4}	1.4×10^{-3}
saw1	3.4×10^{-3}	7.4×10^{-4}	1.8×10^{-3}
saw1v1	3.8×10^{-3}	7.3×10^{-4}	1.7×10^{-3}
saw1v2	3.6×10^{-3}	6.8×10^{-4}	1.7×10^{-3}
saw1v3	3.7×10^{-3}	7.3×10^{-4}	1.7×10^{-3}
saw1vf1	3.2×10^{-3}	6.6×10^{-4}	1.7×10^{-3}
saw1vf2	3.0×10^{-3}	6.1×10^{-4}	1.5×10^{-3}
jump04c	6.8×10^{-3}	8.2×10^{-5}	1.6×10^{-4}

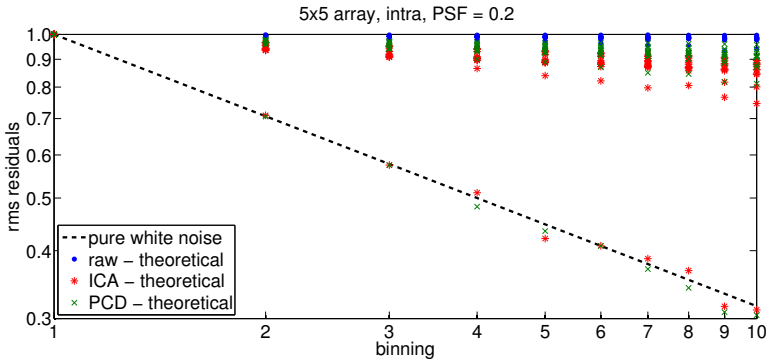

Figure 6.14: Root mean square of residuals for light-curves binned over 1 to 10 points, scaled to their non-binned values. The simulations were obtained with σ_{PSF} =0.2 p.u., 5×5 array, and intra-pixel effects. The dashed black line indicates the expected trend for white residuals, blue dots are for normalized raw light-curves, red '$*$' are for pixel-ICA detrendend light-curves, and green 'x' for PCD detrended light-curves. The only case of jitter for which the residuals are close to white noise is the sudden change ('jump04c' in Table 6.2).

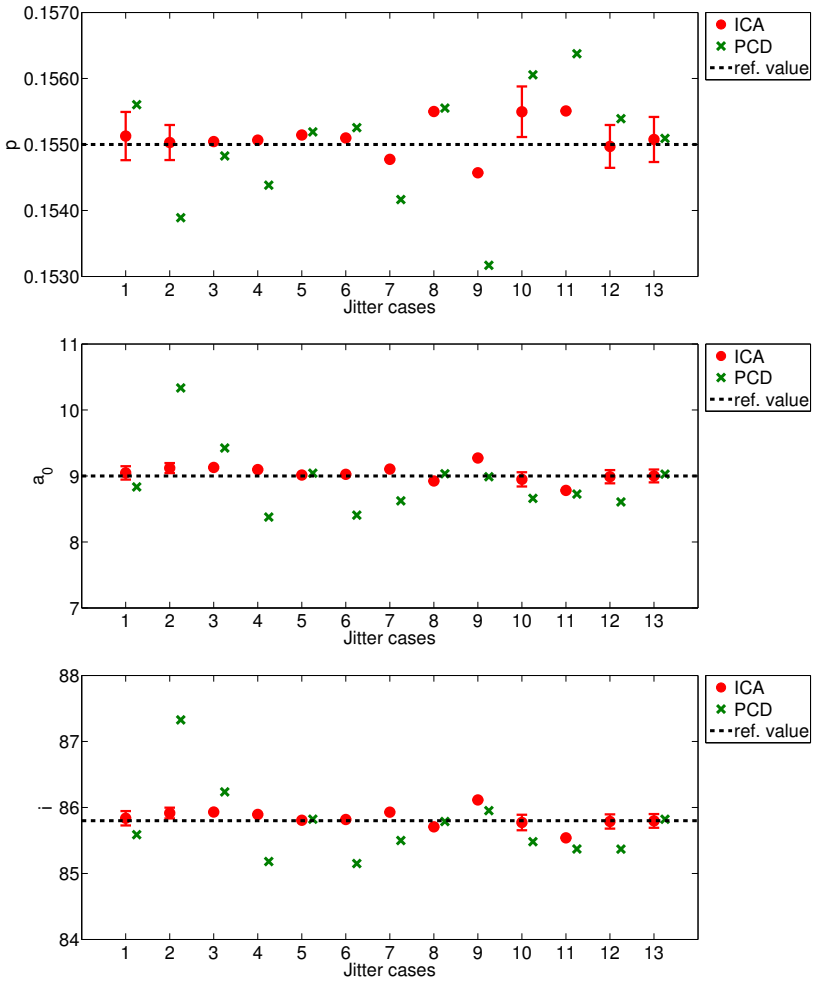

Figure 6.15: Top panel: best estimates of the planet-to-star radii ratio, $p = r_p/R_s$, for detrended light-curves with (red dots) pixel-ICA, and (green 'x') PCD method (σ_{PSF} =0.2 p.u., intra-pixel effects over 5×5 array). Error bars are reported for representative cases of jitter signal, i.e. sin1, cos1, saw1v3, saw1vf2, and jump04c. Middle panel: the same for the orbital semimajor axis in units of the stellar radius, $a_0 = a/R_s$. Bottom panel: the same for the orbital inclination, i.

Additional tables

Table 6.7: Retrieved transit parameters for simulations with σ_{PSF} =1, 9×9 array, inter-pixel effects (see Sec. 6.2.1). In representative cases, I report the partial error bars obtained by the residuals and the final error bars (see Section 5.2).

Jitter	Parameters	Best values	1- σ errors (residual scatter only)	1- σ errors (final)
	p	0.15505	9×10^{-5}	1.4×10^{-4}
sin1	a_0	8.99	0.02	0.03
	i	85.78	0.03	0.04
	p	0.15501	1.0×10^{-4}	1.5×10^{-4}
cos1	a_0	9.05	0.03	0.04
	i	85.85	0.03	0.04
	p	0.15507		
sin2	a_0	8.98		
	i	85.78		
	p	0.15510		
cos2	a_0	8.94		
	i	85.74		
	p	0.15505		
sin3	a_0	8.99		
	i	85.79		
	p	0.15503		
cos3	a_0	9.02		
	i	85.82		
	p	0.15506		
saw1	a_0	8.98		
	i	85.78		
	p	0.15506		
saw1v1	a_0	8.99		
	i	85.79		
	p	0.15511		
saw1v2	a_0	9.02		
	i	85.81		
	p	0.15508	1.0×10^{-4}	1.5×10^{-4}
saw1v3	a_0	8.99	0.03	0.04
	i	85.79	0.03	0.05
	p	0.15509		
saw1vf1	a_0	8.98		
	i	85.77		
	p	0.15506	1.0×10^{-4}	1.5×10^{-4}
saw1vf2	a_0	8.99	0.03	0.04
	i	85.79	0.03	0.05
	p	0.15503	1.0×10^{-4}	1.4×10^{-4}
jump04c	a_0	9.00	0.03	0.04
	i	85.80	0.03	0.04

Table 6.8: Retrieved transit parameters for simulations with σ_{PSF} =1, 5×5 array, inter-pixel effects (see Sec. 6.2.1). In representative cases, I report the partial error bars obtained by the residuals and the final error bars (see Section 5.2).

Jitter	Parameters	Best values	1- σ errors (residual scatter only)	1- σ errors (final)
	p	0.15524	1.5×10^{-4}	2.2×10^{-4}
sin1	a_0	8.97	0.04	0.06
	i	85.76	0.05	0.07
	p	0.15505	1.6×10^{-4}	2.2×10^{-4}
cos1	a_0	9.18	0.05	0.07
	i	85.99	0.05	0.07
	p	0.15510		
sin2	a_0	9.08		
	i	85.88		
	p	0.15536		
cos2	a_0	8.89		
	i	85.66		
	p	0.15528		
sin3	a_0	8.99		
	i	85.79		
	p	0.15516		
cos3	a_0	9.07		
	i	85.86		
	p	0.15519		
saw1	a_0	8.97		
	i	85.77		
	p	0.15517		
saw1v1	a_0	9.02		
	i	85.81		
	p	0.15494		
saw1v2	a_0	8.92		
	i	85.74		
	p	0.15527	1.5×10^{-4}	2.4×10^{-4}
saw1v3	a_0	8.98	0.04	0.07
	i	85.77	0.05	0.07
	p	0.15524		
saw1vf1	a_0	9.00		
	i	85.78		
	p	0.15531	1.6×10^{-4}	2.2×10^{-4}
saw1vf2	a_0	8.99	0.04	0.06
	i	85.79	0.05	0.07
	p	0.15508	1.3×10^{-4}	2.6×10^{-4}
jump04c	a_0	9.04	0.04	0.07
	i	85.83	0.04	0.08

Table 6.9: Retrieved transit parameters for simulations with σ_{PSF} =0.2, 5×5 array, inter-pixel effects (see Sec. 6.2.1). In representative cases, I report the partial error bars obtained by the residuals and the final error bars (see Section 5.2).

Jitter	Parameters	Best values	1- σ errors (residual scatter only)	1- σ errors (final)
	p	0.15507	3×10^{-5}	6×10^{-5}
sin1	a_0	9.010	0.010	0.018
	i	85.808	0.010	0.020
	p	0.15505	4×10^{-5}	6×10^{-5}
cos1	a_0	9.018	0.010	0.016
	i	85.815	0.011	0.017
	p	0.15508		
sin2	a_0	9.009		
	i	85.806		
	p	0.15505		
cos2	a_0	9.004		
	i	85.801		
	p	0.15510		
sin3	a_0	9.001		
	i	85.798		
	p	0.15507		
cos3	a_0	9.015		
	i	85.812		
	p	0.15506		
saw1	a_0	8.993		
	i	85.791		
	p	0.15506		
saw1v1	a_0	9.000		
	i	85.798		
	p	0.15506		
saw1v2	a_0	8.997		
	i	85.795		
	p	0.15506	3×10^{-5}	5×10^{-5}
saw1v3	a_0	8.998	0.009	0.015
	i	85.796	0.010	0.016
	p	0.15508		
saw1vf1	a_0	8.999		
	i	85.797		
	p	0.15506	3×10^{-5}	5×10^{-5}
saw1vf2	a_0	9.001	0.009	0.015
	i	85.798	0.010	0.016
	p	0.15508	4×10^{-5}	6×10^{-5}
jump04c	a_0	9.00	0.011	0.017
	i	85.80	0.011	0.018

Table 6.10: Retrieved transit parameters for simulations with σ_{PSF} =0.2, 5×5 array, intra-pixel effects (see Sec. 6.2.1). In representative cases, I report the partial error bars obtained by the residuals and the final error bars (see Section 5.2).

Jitter	Parameters	Best values	1- σ errors (residual scatter only)	1- σ errors (final)
	p	0.1551	3×10^{-4}	4×10^{-4}
sin1	a_0	9.05	0.07	0.10
	i	85.84	0.08	0.11
	p	0.1550	2×10^{-4}	3×10^{-4}
cos1	a_0	9.12	0.07	0.08
	i	85.92	0.08	0.08
	p	0.1550		
sin2	a_0	9.13		
	i	85.93		
	p	0.1551		
cos2	a_0	9.10		
	i	85.89		
	p	0.1551		
sin3	a_0	9.01		
	i	85.81		
	p	0.1551		
cos3	a_0	9.02		
	i	85.82		
	p	0.1548		
saw1	a_0	9.10		
	i	85.93		
	p	0.1555		
saw1v1	a_0	8.92		
	i	85.71		
	p	0.1546		
saw1v2	a_0	9.27		
	i	86.11		
	p	0.1555	4×10^{-4}	4×10^{-4}
saw1v3	a_0	8.95	0.10	0.11
	i	85.77	0.11	0.12
	p	0.1555		
saw1vf1	a_0	8.78		
	i	85.54		
	p	0.1550	3×10^{-4}	3×10^{-4}
saw1vf2	a_0	8.99	0.09	0.10
	i	85.79	0.10	0.11
	p	0.15508	4×10^{-5}	3×10^{-4}
jump04c	a_0	9.001	0.011	0.10
	i	85.796	0.012	0.10

6.2.2 The effect of Poisson noise

I tested the effect of Poisson noise associated with the astrophysical source at different levels. It is well explained by the results obtained with:

1. σ_{PSF} =1 p.u., inter-pixel variations over 9×9 array, jitter 'sin1';

2. σ_{PSF} =0.2 p.u., intra-pixel variations over 5×5 array, jitter 'sin1' and 'cos1';

Figure 6.16 shows the raw and detrended light-curves obtained for the listed cases with two finite values of Signal-to-Noise Ratio, SNR = 447 (intermediate) and SNR = 224 (lowest). Figure 6.17 shows how the residuals scale for binning over n points, with $1 \leq n \leq 10$, in one of the most problematic case of intra-pixel variations (jitter 'sin1'). As expected, binning properties depend on the amplitude of the white noise relative to systematic noise; therefore, for cases with lower SNR it may superficially appear that systematics are better removed in the detrending process (Figure 6.14 shows much higher deviations from the white noise behaviour for the case with zero poissionian noise). Figure 6.18 reports the transit parameters retrieved from detrended light-curves; in representative cases, I calculated the error bars.

Figure 6.19 shows the amplitude of discrepancies between the detrended light-curves and the theoretical model as a function of astrophysical Poisson noise, for pixel-ICA and PCD method with different polynomial orders:

1. For the inter-pixel effects the efficiency of the two methods is limited by the astrophysical Poisson noise level, except when it is smaller than the instrument HFPN, in which cases pixel-ICA slightly outperforms PCD.

2. For the intra-pixel effects, residual systematics are clearly present in high-SNR cases, while for lower SNR the limit is the Poissonian threshold. The second-order PCD method is far from optimal, while higher-order polynomials in some cases can do better than pixel-ICA, but they do not always improve the results, as already mentioned in Section 6.2.1.

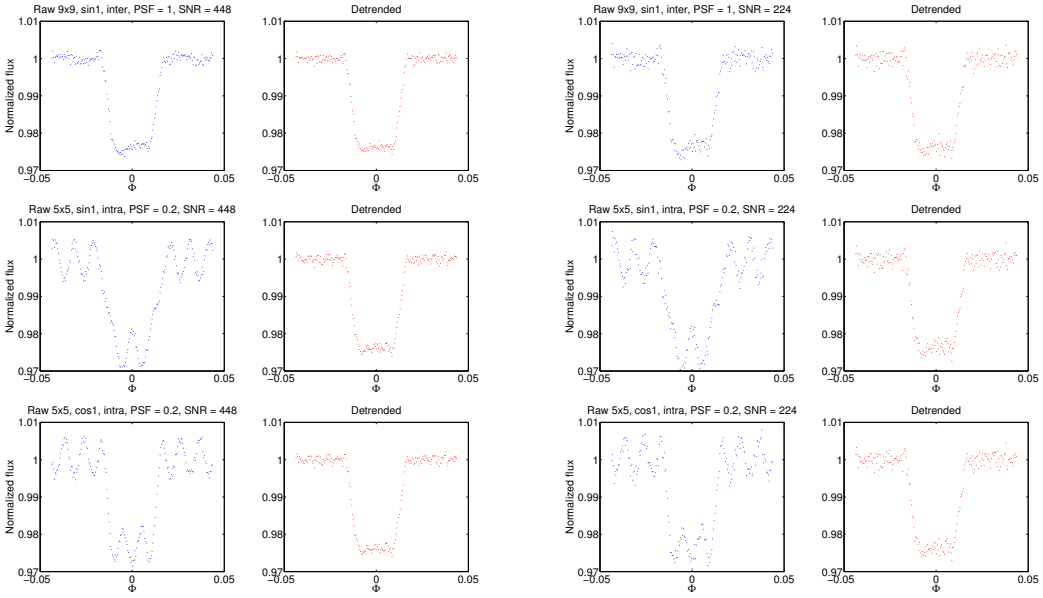

Figure 6.16: Top panels: (blue) raw light-curves simulated with σ_{PSF} =1 p.u., inter-pixel quantum efficiency variations over 9×9 array of pixels, jitter 'sin1', and poissonian noise with (left) SNR = 447, and (right) SNR = 224; (red) corresponding detrended light-curves with pixel-ICA. Middle panels: the same for raw light-curves simulated with σ_{PSF} =0.2 p.u., intra-pixel quantum efficiency variations over 5×5 array of pixels, and jitter 'sin1'. Bottom panels: the same for light-curves simulated with σ_{PSF} =0.2 p.u., intra-pixel quantum efficiency variations over 5×5 array of pixels, and jitter 'cos1'. All the light-curves are binned over 10 points, as in previous figures.

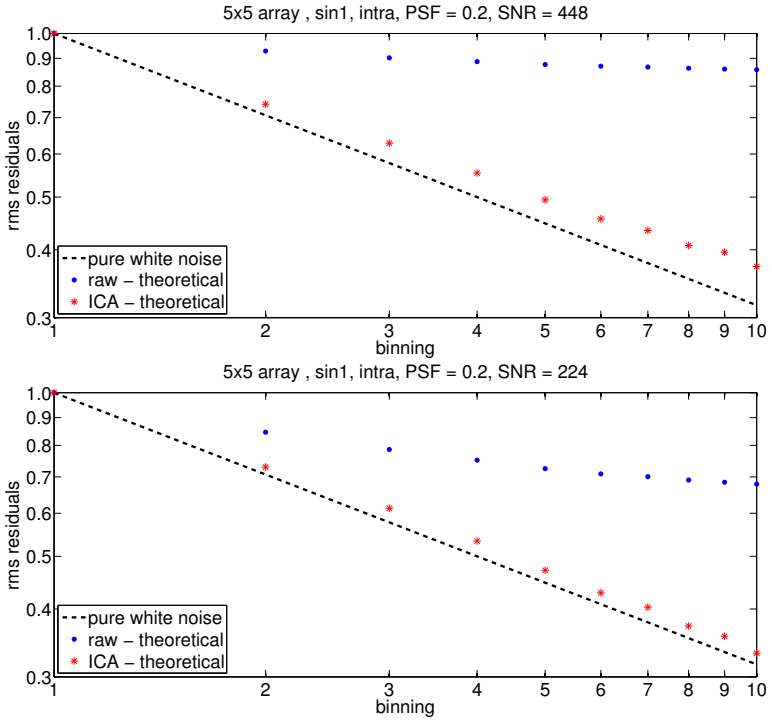

Figure 6.17: Top panel: Root mean square of residuals for binning over 1 to 10 points, scaled to their non-binned values, obtained for simulations with σ_{PSF} =0.2 p.u., intra-pixel effects over a 5×5 array, jitter 'sin1', and poissonian noise with SNR = 447. The dashed black line indicates the expected trend for white residuals, blue dots are for normalized raw light-curves, and red '∗' are for pixel-ICA detrendend light-curves. Bottom panel: the same, but with SNR = 224.

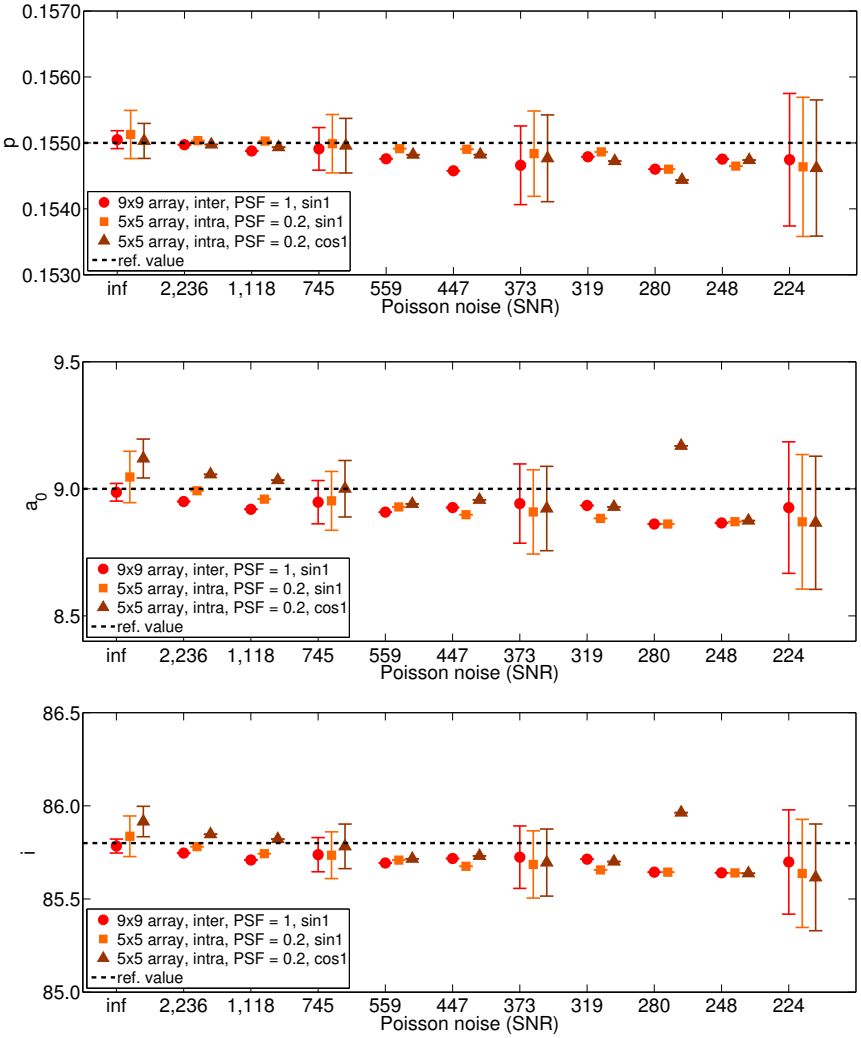

Figure 6.18: Top panel: best estimates of the planet-to-star radii ratio, $p = r_p/R_s$, for some detrended light-curves with Poissonian noise at different levels. Error bars are reported for representative cases. Middle panel: the same for the orbital semimajor axis in units of the stellar radius, $a_0 = a/R_s$. Bottom panel: the same for the orbital inclination, i. The parameter estimates appear to be biased in the same direction because the same realization of poissonian noise is adopted for all cases, only with different scaling factors.

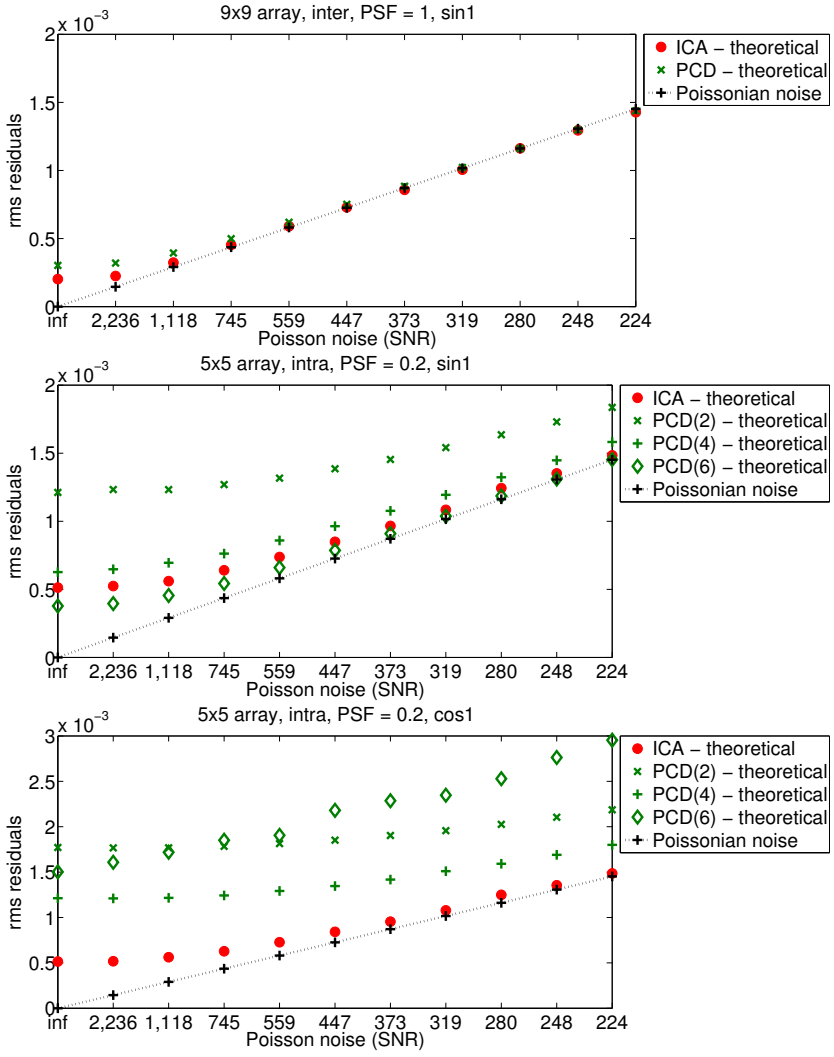

Figure 6.19: Top panel: Root mean square of discrepancies between detrended light-curves with (red circles) pixel-ICA, and (green) PCD method, and the theoretical model, obtained for simulations with σ_{PSF} =1 p.u., inter-pixel effects over a 9×9 array, jitter 'sin1', and poissonian noise at different levels. Black '+' along dashed line indicate the root mean square of the poissonian signal. Middle panel: The same for simulations with σ_{PSF} =0.2 p.u., intra-pixel effects over a 5×5 array, jitter 'sin1'. Green '+' refer to light-curves detrendend with a 4^{th} order polynomial, and green rhomboids with a 6^{th} order one. Bottom panel: The same for simulations with σ_{PSF} =0.2 p.u., intra-pixel effects over a 5×5 array, jitter 'cos1'.

6.2.3 Inter-pixel effects without noise

In Section 6.2.1 I state that inter-pixel effects are well detrended with pixel-ICA method, based on the binning properties of residuals (and consistent results). Given that binning properties can only prove that systematics are negligible compared to the actual white noise level, I performed a last test for a simulation with inter-pixel effects (σ_{PSF} =1, 9×9 array, jitter sin1) and a white noise level reduced by a factor 10. Note that the white noise level is an extremely low value of 0.5 photon counts/pixel/data point[1]. Figure 6.20 shows the raw and detrended light-curves for this simulation, and the binning properties of their residuals. The time structure is very high for the raw light-curve, but it is again well detrended by pixel-ICA. I also checked that all the retrieved parameters are consistent with the original values within 1 σ.

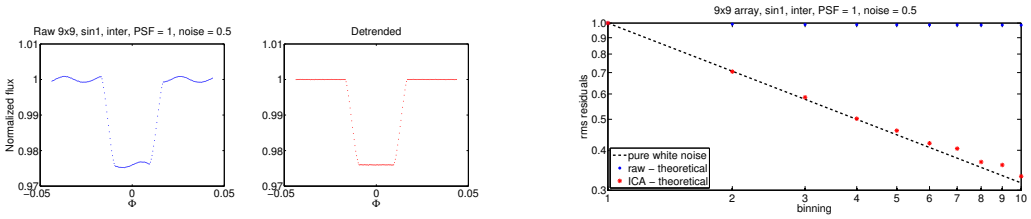

Figure 6.20: Left panels: (blue) raw light-curve simulated with σ_{PSF} =1 p.u., inter-pixel sensitivity variations over 9×9 array of pixels, jitter 'sin1', and white noise at 0.5 photon counts/pixel/frame; (red) corresponding detrended light-curve with pixel-ICA. Right panel: Root mean square of residuals for binning over 1 to 10 points, scaled to their non-binned values.

6.2.4 Comparison with different detrending methods

I have tested the pixel-ICA algorithm over the simulations using method 2 and method 3 in Equation 5.3; the results have been reported for method 2. The results obtained with method 3 were identical, except for some of the configurations obtained with 'cos1' jitter (unfortunate timescale and phasing), for which the results obtained with the two approaches are not identical, but consistent within 1 σ.

I also tested a modified version of the PLD algorithm for data detrending (Deming et al., 2015). The modification was necessary for the algorithm to converge (Morello, 2015). A possible explanation is that they adopt a first-order approximation which is fine for the eclipses, but not for the much deeper transit considered in this work. The results obtained with the modified PLD algorithm are practically indistinguishable from the ones obtained with pixel-ICA.

[1] I do not set this noise exactly to 0, because pixel time series with many zeroes would negatively affect the ICA detrending.

6.3 Conclusion

I have tested the pixel-ICA algorithm to detrend simulated datasets. Systematics similar to the ones present in *Spitzer*/IRAC datasets are obtained by combining instrumental jitter with inter- or intra-pixel sensitivity variations. A variety of jitter time series is used to test the pixel-ICA method with:

1. periodic signals with different frequencies, phasing and shape;
2. non-stationary signals with varying amplitudes or frequencies;
3. sudden change.

The detrending performances of pixel-ICA method have been compared to a division by a polynomial function of the centroid, in this chapter PCD method, and the PLD method (Deming et al., 2015). Here I summarize the main results found:

1. Pixel-ICA algorithm can detrend non-stationary signals and sudden changes, as well as periodic signals with different frequencies and phasing, relative to the transit.
2. Inter-pixel effects are well-detrended with pixel-ICA method.
3. Even if the instrument PSF is not entirely within the array of pixels, pixel-ICA leads to results which are consistent at $\sim$1 σ with the input parameters.
4. In most cases, pixel-ICA outperforms the PCD method, especially if the instrument PSF is narrow, or it is not entirely within the photometric aperture.
5. Intra-pixel effects are only detectable if the PSF is relatively small.
6. Intra-pixel effects cannot be totally detrended by any of the three methods, but pixel-ICA, in most cases, outperforms the PCD method, which is largely case-dependent. Also, the pixel-ICA method provides consistent results within the error bars.
7. It is possible to fit the astrophysical signal after detrending or together with the other components. Differences are registered only if at least one of the non-transit components has a similar shape at the time of transit, in which case the first approach is preferable, but the two results were consistent within 1 σ.
8. The PLD method, updated to include cross-terms between pixel fluctuations and the astrophysical signals, leads to very similar results as pixel-ICA, particularly if the astrophysical signal is fitted together with the other components.

In conclusion, I have found thar in a variety of simulated cases pixel-ICA performs as well or better than other methods used in the literature, in particular polynomial centroid corrections and pixel-level decorrelation (Deming et al., 2015). The main advantage of pixel-ICA over other methods relies on its purely statistical foundation without the need to impose prior knowledge of the instrumental systematics, therefore avoiding a potential source of error. The results of this study, together with previous analyses of real *Spitzer*/IRAC datasets (Morello et al., 2014, 2015), suggest that photometric precision and repeatability at the level of one part in 10^4 can be achieved with current infrared space instruments.

Chapter 7

Application to Warm Spitzer eclipse observations

7.1 Wavelet ICA

7.1.1 Motivation

The ability of ICA to decorrelate non-gaussian signals is inherently limited to cases where the gaussian noise amplitude is low relative to the other signals. This poses a limit on the quality of the data that can be successfully detrended with ICA. Wavelet ICA algorithms have been proposed to outperform the standard ICA in detrending low signal-to-noise data in a variety of contexts, such as medical sciences (e.g. La Foresta et al., 2006; Inuso et al., 2007; Mammone et al., 2012), engineering (e.g. Lin and Zhang, 2005), acoustics (e.g. Moussaoui et al., 2006; Zhao et al., 2006), image denoising (e.g. Karande and Talbar, 2014) and astrophysics (e.g. Waldmann, 2014). Other preprocessing steps for denoising, e.g. Wiener filters, have been tested, but preliminary results were less promising and they have not been further investigated. A possible explanation is that Wiener filters, differently from a wavelet or Fourier decomposition, introduce a distortion in the original signals.

7.1.2 Continuous Wavelet Transform (CWT)

The wavelet transform (WT) decomposes a given signal, $x(t)$, into its frequency components. This is done by convolving the time signal with a basis of highly localized impulses or "wavelets". To fix the ideas, I assume that $x(t)$ is a time series, although this is not necessary, as the WT can be applied to different kinds of signals. The individual wavelet functions are derived from

a single "mother wavelet", $\psi(t)$, through translation and dilation of the mother wavelet. The mathematical definition of the CWT is

$$c_{\tau,\varphi} = \int_{\mathbb{R}} x(t)\psi_{\tau,\varphi}(t)\ dt \tag{7.1}$$

$$\psi_{\tau,\varphi}(t) = \frac{1}{\sqrt{2}}\ \psi\left(\frac{t-\tau}{\varphi}\right) \tag{7.2}$$

where $\psi_{\tau,\varphi}$ is the mother wavelet for a given scaling φ and translation τ, and $c_{\tau,\varphi}$ is the wavelet coefficient with respect to τ and φ.

If the wavelet basis is orthogonal, the inverse wavelet transform can be used to reconstruct the original time series:

$$x(t) = \sum_{\varphi\in\mathbb{Z}}\sum_{\tau\in\mathbb{Z}} c_{\tau,\varphi}\psi_{\tau,\varphi}(t), \tag{7.3}$$

where $\mathbb{Z}$ is the set of integer numbers.

The mother wavelet can be chosen from a variety of wavelet families with different properties. For more details I refer to the relevant literature, e.g. Daubechies (1992); Percival and Walden (2000).

7.1.3 Discrete Wavelet Transform (DWT)

Astronomical data are usually in the form of discrete time series. For the DWT the mother wavelet is denoted by $h(t)$, and the scaling function, also called "father wavelet", is denoted by $g(t)$. The mother and father wavelets act as high-pass and low-pass frequency filters, respectively. They are related by

$$g(L-1-t) = (-1)^t\ h(t), \tag{7.4}$$

where L is the filter length and corresponds to the number of points in the time series $x(t)$.

The one-level DWT is defined by

$$cA_1(\tau) = (x * g)(t) \downarrow 2 = \sum_{t=-\infty}^{+\infty} x(t)\ g(2\tau - t) \tag{7.5}$$

$$cD_1(\tau) = (x * h)(t) \downarrow 2 = \sum_{t=-\infty}^{+\infty} x(t)\ h(2\tau - t) \tag{7.6}$$

The cA_1 time series, so-called "average coefficients", approximates the underlying low-frequency trend of $x(t)$, while the cD_1 time series, so-called "detail coefficients", represents a higher-frequency component. They are down-sampled by a factor 2 ("$\downarrow 2$" in Equations 7.5 and 7.6) with respect to the original time series, in recognition of the Nyquist theorem.

It is possible to apply the g and h filters to the cA_1 time series, then obtain new sets of coefficients, cA_2 and cD_2, and iterate the process. The n-level DWT includes the cA_n series of average coefficients, down-sampled by a factor 2^n, and n series cD_1–cD_n of detail coefficients, representing bands of higher frequencies. The original data can be reconstructed by reversing the process:

$$x(t) = cA_n(\tau)\ g(-t + 2\tau) + \sum_{i=1}^{n} \sum_{\tau=-\infty}^{+\infty} (cD_i\ h(-t + 2\tau)) \tag{7.7}$$

7.1.4 Wavelet ICA

In wavelet ICA algorithms, the DWT is applied to the observed signals:

$$x_k(t) \rightarrow \hat{x}_k = (cA_{k,n}, cD_{k,n}, \ldots, cD_{k,1}) \tag{7.8}$$

$$\mathbf{x}(t) \rightarrow \hat{\mathbf{x}} = (\hat{x}_1(t), \hat{x}_2(t), \ldots, \hat{x}_m(t))^T \tag{7.9}$$

The ICA separation is performed with the series of coefficients:

$$\hat{\mathbf{s}} = \hat{\mathbf{W}}\hat{\mathbf{x}} \tag{7.10}$$

The independent component series of coefficients are:

$$\hat{s}_l = (cA_{l,n}, cD_{l,n}, \ldots, cD_{l,1}) \tag{7.11}$$

They can be converted into the time domain through inverse DWT (Equation 7.7).

The DWT first separates the high-frequency components from the low-frequency trend, enhancing the ability of ICA to disentangle the low-frequency independent components. The trade-off is down-sampling the signals by a factor 2^n, n being the level of the DWT. This step is particularly important in cases where the gaussian noise is dominant. Additional processing options/variants have been proposed in the literature to improve the ICA performance further in specific contexts, e.g. coefficients' thresholding (Stein, 1981; Donoho, 1995), suppression of some frequency ranges (Lin and Zhang, 2005), or taking individual levels as input to ICA (Inuso et al., 2007; Mammone et al., 2012). In this Thesis, I aim to provide the most objective analysis of the datasets, with minimal prior assumptions, hence these variants are not considered. The impact of these variants and other operations on the data will be carefully investigated in future studies.

7.2 Eclipses of XO3b observed with Warm Spitzer

7.2.1 The exoplanet system XO3b

XO3b is a hot Jupiter (M_p =11.7 ± 0.5 M_J, Johns-Krull et al., 2008; Hirano et al., 2011) in an eccentric orbit (e =0.283 ± 0.003, Knutson et al., 2014a) with a period of 3.19 days and orbital semimajor axis of a = 0.045 AU (Winn et al., 2008). The host star is F5V with T_* = 6760 ± 80 K, and $\log g$ =4.24 ± 0.03 (Winn et al., 2008; Torres et al., 2012). The apparent magnitude is ∼8.8 in the infrared K band. A previous analysis of the 12 eclipses reported an average eclipse depth of $1.58^{+0.03}_{-0.04}\times\ 10^{-3}$ relative to the out-of-eclipse flux (star+planet), and a phase-curve slope of $6.0^{+1.3}_{-1.6}\times\ 10^{-4}$ days^{-1} (Wong et al., 2014).

7.2.2 Observations

I reanalysed twelve eclipse observations of XO3b taken with *Spitzer*/IRAC in the 4.5 μm band. Ten individual eclipses were observed over six months (Nov 11, 2012 – May 24, 2013), including two sets of three consecutive eclipses; another eclipse is contained within a full-orbit observation on May 5, 2013 (PID: 90032). Each individual observation consists of 14,912 frames over 8.4 hr using IRAC's sub-array readout mode with 2.0 s integration time. In sub-array mode 64 frames are taken consecutively, and the reset time is ∼1 s. I extracted 14,912 frames from the full-orbit observation to analyse the light-curve of the eclipse over a time interval similar to other observations. The last eclipse was extracted out of a 66 hr observation on April 8, 2010 (PID: 60058). Table 7.1 reports the dates in which the eclipses were observed.

Table 7.1: Eclipse observations dates and orbit numbers of XO3b.

Obs. Number	UT Date	Orbit Number
1	2010 Apr 8	0
2	2012 Nov 11	297
3	2012 Nov 17	299
4	2012 Nov 20	300
5	2012 Nov 23	301
6	2012 Dec 2	304
7	2012 Dec 9	306
8	2013 Apr 22	348
9	2013 May 5	352
10	2013 May 18	356
11	2013 May 21	357
12	2013 May 24	358

7.2.3 Analysis

Here, I list the main steps of the wavelet pixel-ICA algorithm that I have developed to detrend warm *Spitzer*/IRAC data, followed by a more accurate description and comments:

1. Select an array of pixels. The raw light-curve is the sum of the individual pixel time series within the selected array.
2. Remove outliers.
3. Subtract the background from the raw light-curve.
4. Compute the wavelet transforms of the pixel light-curves.
5. Perform ICA decomposition of the wavelet-transformed pixel light-curves.
6. Compute the inverse wavelet transforms of the independent components.
7. Simultaneously fit the components (except the eclipse one) and astrophysical model to the raw light-curve.
8. Estimate parameter error bars.

Selecting the pixel-array

The previous analyses, discussed in Chapter 5, showed that pixel-ICA performances are only slightly dependent on the choice of the array. Larger arrays are more photometrically stable, as they contain larger fractions of the instrument PSF and are less subject to the variable loss of photons depending on the PSF position, but they also include more noise. Several tests favored the choice of a 5×5 array, immediately followed by the 7×7 one. The new observations differ from the previous ones, as the new ones are taken during the warm Spitzer era, hence they are affected by stronger systematics and higher noise levels (Krick et al., 2015). Also, the amplitude of the astrophysical signal is an order of magnitude smaller in the new observations. Under the new conditions, tests confirmed that different choices of the pixel-array led to consistent results to well within 1 σ, but the error bars are more dependent on this choice. In particular, the error bars obtained with the 7×7 array are 1 to 1.5 times larger than those obtained with the 5×5 array, mainly because of the larger σ_{ICA} term. For these reasons, I selected the results obtained with the 5×5 array of pixels.

Outlier rejection

I flag and correct outliers in the flux time series. First, I calculate the standard deviations of any set of five consecutive points and take the median value as the representative standard deviation.

I define the expected value in one point as the median of the four closest points, i.e. two before and two after. Points differing from their expected values by more than five times the standard deviation are flagged as outliers. They are then replaced with the mean value of the points immediately before and after, or, in case of two consecutive outliers, with a linear interpolation between the closest points which are not outliers. I checked that the outliers **replaced** after this process are coincident with outliers that would have been spotted by eye. They are less than 0.35% the number of points in each observation. No significant differences are found if the outliers are removed from the analysis without replacing with new values.

Background subtraction

The background is estimated by taking the mean flux over four arrays of pixels with the same size of the selected array (5×5 or 7×7) near the corners of the sub-array area. Uncorrected background may bias the normalized amplitude of the eclipse depth, as well as the phase-curve's slope, if the background is not constant over time. The typical morphology of a background time series is either a constant or a slow monotonic drift. The lack of a distinct temporal structure and non-gaussianity makes it difficult to disentangle it with ICA or with other statistical methods. For this reason, I performed ad hoc background subtractions before ICA detrending. The impact of background is potentially higher compared to the other observations analysed in this Thesis, because XO3 is less bright than the other targets. Here I found that the impact of background on individual measurements of the eclipse depth is at the level of $\sim 10^{-5}$, well below the error bars. Instead, the phase constant is systematically larger without background subtraction, i.e., in average, $\sim 13 \times 10^{-4}$ vs $\sim 7 \times 10^{-4}$ days^{-1}. The individual error bars account for this discrepancy, but the weighted mean is not reliable in presence of a systematic error.

Temporal binning

Given the large number of frames for each observation (14,912), binning the data is very useful, in particular to decrease the computational time needed to run the MCMC calculations. Some authors suggest that an optimal choice of the bin size can be useful to reduce the noise on the timescale of interest (Deming et al., 2015; Kammer et al., 2015), provided that the theoretical curve is similarly binned to eliminate the bias, and the bin size is not too long to cause significant loss of astrophysical information (Kipping, 2010).

An additional choice for the pixel-ICA algorithm is whether to bin the pixel time series prior the ICA separation, or to bin the independent components extracted from the unbinned pixel time series. I found that the two options are almost equivalent, as the eclipse signals obtained

after removing the systematic components from the raw light-curve are identical (discrepancies 1 to 2 order of magnitudes smaller than the fitting residuals), except in cases for which the unbinned ICA separation fails to retrieve an eclipse component. It is worth noting that for the unbinned case, the amplitude of the total noise plus systematics is higher than the eclipse depth. Thus I decided to bin the pixel light-curves prior ICA retrieval.

I tested bin sizes of 32 and 64 frames, i.e. 64 and 128 s, respectively. The parameter results obtained with the two binning choices are all consistent within 0.5 σ, and on average within 0.16 σ. The smaller bin size led to smaller error bars and standard deviations for the twelve measurements of the eclipse depth and phase constant by factors of $\sim$1.4, and also whiter fitting residuals. Based on these tests, I consider the results obtained with bin size of 32 frames as the best ones.

Wavelet-transforms

The pixel light-curves are wavelet-transformed before performing the ICA separation. More specifically, I adopted one-level DWT with mother wavelet Daubechies-4 (Daubechies, 1992). I found that different choices of the mother wavelet, among different families and numbers, lead to exactly the same results, and higher-level DWTs often appear to make it impossible for ICA to retrieve the eclipse component. The difficulties with higher-level DWTs may arise from sub-sampling the signals, and the fact that some of the low-frequency components may be smeared over a higher level of detail coefficients.

ICA decomposition

It is performed on the wavelet-transformed pixel light-curves (see Equation 7.10).

Inverse wavelet transforms

The independent components are transformed back in the time domain through inverse DWTs (see Equation 7.7).

MCMC fitting

I adopt an approach similar to method 3 in Section 5.2, i.e., in this case, simultaneous fitting of an eclipse model (see Section 3.4.2) and a linear combination of the non-eclipse components extracted by ICA. When fitting the eclipse models, the orbital parameters are fixed to the values reported in Table 7.2, taken from Wong et al. (2014), while the center of eclipse, eclipse depth and phase constant are free parameters. First estimates of the parameters and scaling coefficients are

Table 7.2: Values of the parameters fixed while generating the eclipse models.

P	3.19153285 days
a_R	7.052
i	84.11°
e	0.2833
ω	346.8°

Table 7.3: Individual best parameters results obtained in this work. The MCMC error bars without the σ_{ICA} contribution are reported in parenthesis next to the final error bars.

Obs. Number	Depth (10^{-3})	1 σ error	Phase constant (10^{-4} days^{-1})	1σ error
1	1.66	0.11 (0.09)	-6	7 (6)
2	1.72	0.11 (0.10)	6	8 (7)
3	1.54	0.10 (0.10)	8	5 (5)
4	1.56	0.10 (0.08)	9	7 (6)
5	1.52	0.10 (0.09)	-9	7 (6)
6	1.56	0.13 (0.10)	2	10 (8)
7	1.64	0.11 (0.10)	5	10 (9)
8	1.57	0.12 (0.09)	0	11 (9)
9	1.54	0.11 (0.09)	0	5 (3)
10	1.52	0.10 (0.10)	11	8 (7)
11	1.50	0.12 (0.09)	16	7 (5)
12	1.48	0.12 (0.09)	8	6 (5)

obtained through a Nelder-Mead optimization algorithm (Lagarias et al., 1998); they are then used as optimal starting points for an Adaptive Metropolis algorithm with delayed rejection (Haario et al., 2006), generating chains of 300,000 values. The output chains are samples of the posterior (gaussian) distributions. I adopt the mean values of the chains as final best estimates of the parameters, and the standard deviations as zero-order error bars, $\sigma_{par,0}$.

Final error bars

The final error bars are calculated according to Equations 5.2 and 5.3 (method 3).

7.2.4 Results

Figure 7.1 shows the raw light-curves for the twelve observations, the corresponding detrended eclipses and best models, obtained using the 5×5 array and binning over 32 frames, i.e. ∼64 s. The individual measurements of eclipse depth and phase constant are reported in Figure 7.2 and Table 7.3. The results from all epochs are consistent within the error bars, suggesting the lack of any detectable astrophysical variability for this system, and of any residual instrument variability. By taking the weighted means of the individual measurements, I obtained global best estimates of $(1.57 \pm 0.03)\times10^{-3}$ for the eclipse depth, and $(4.4 \pm 2.0)\times10^{-4}$ days^{-1} for the phase constant.

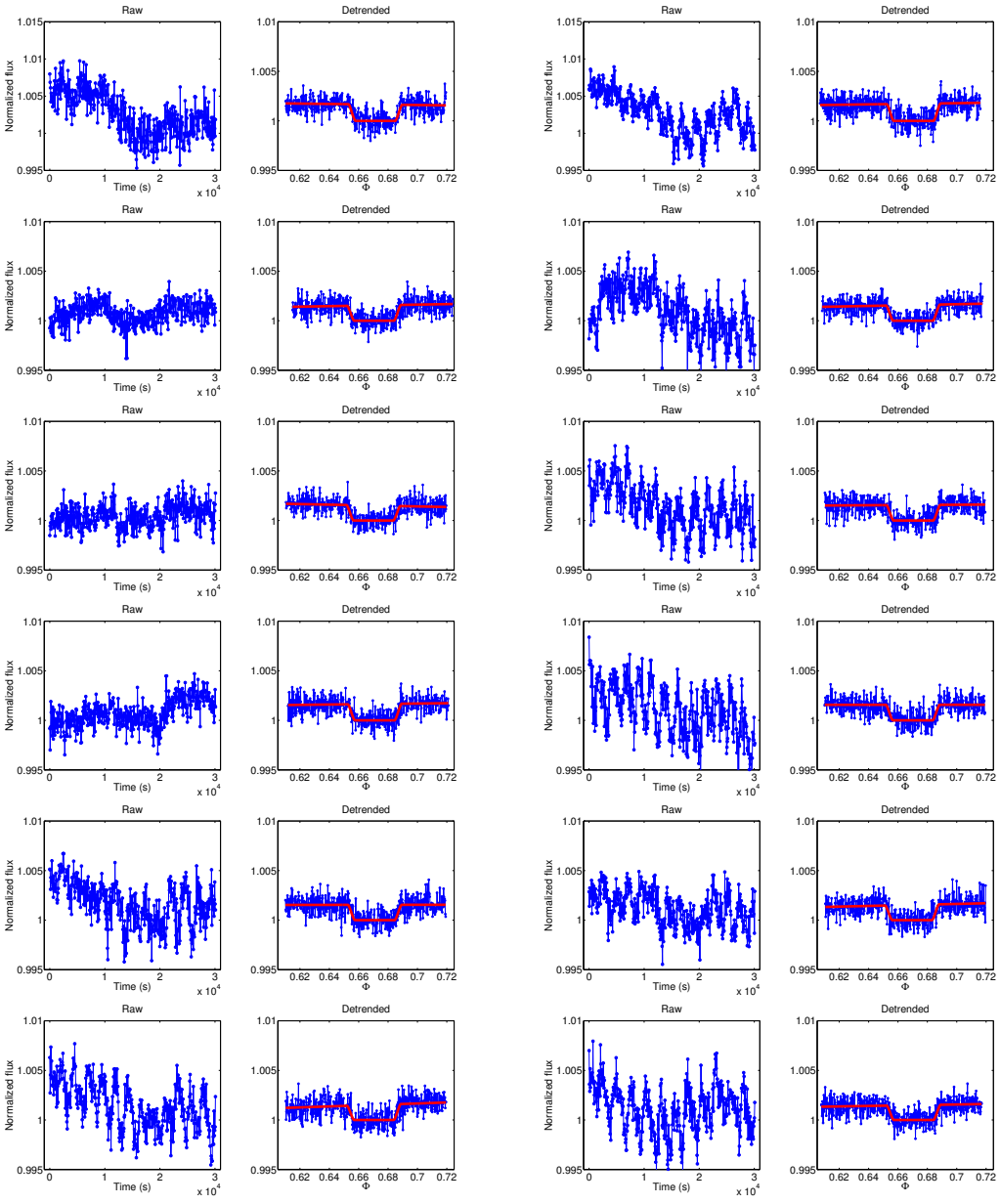

Figure 7.1: Left panels: (blue) raw light-curves obtained from 5×5 array of pixels. Right panels: (blue) detrended eclipse light-curves obtained with wavelet pixel-ICA method, and (red) best eclipse models. All the light-curves are binned over 32 frames, i.e. ∼64 s.

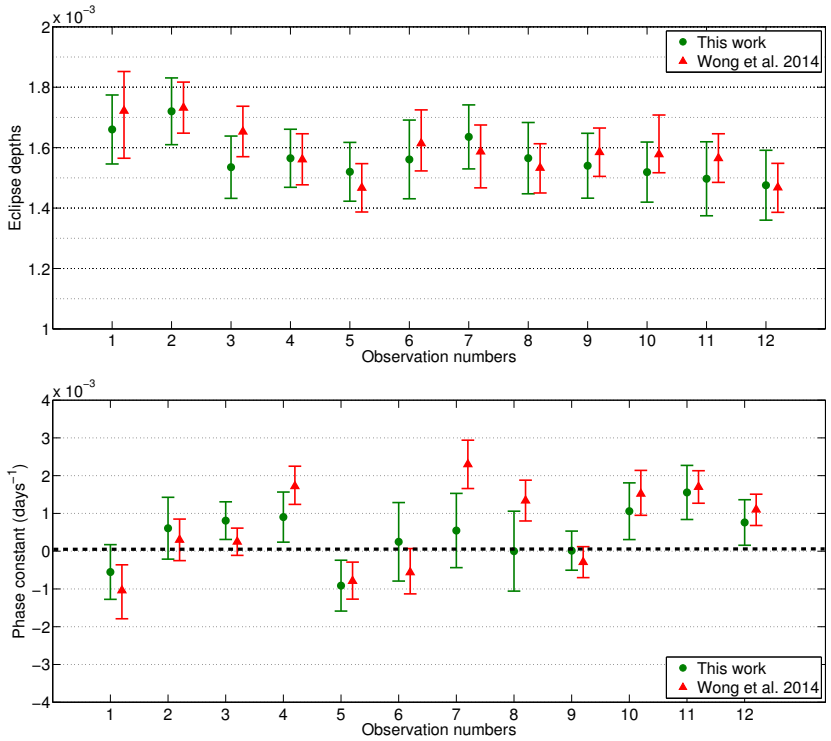

Figure 7.2: Top panel: (green circles) individual best eclipse depth measurements obtained in this work, and (red triangles) results from Wong et al. (2014). Bottom panel: the same for individual measurements of the phase constant.

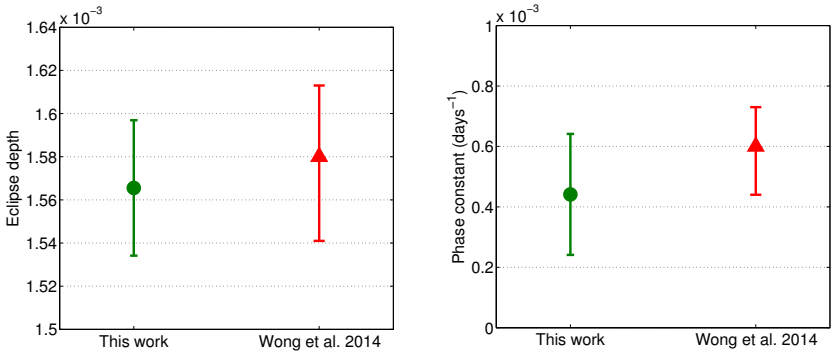

Figure 7.3: Left panel: (green circle) best global eclipse depth estimate obtained in this work, and (red triangle) in Wong et al. (2014). Right panel: the same for the global phase constant.

7.2.5 Discussion

Reduced chi-squared tests

The underlying assumption for the weighted mean to be a valid parameter estimate is that individual measurements of that parameter are normally distributed around the same mean value with variances σ_i^2, and there are no systematic errors. The reduced chi-squared can be

used to test, in part, this hypothesis:

$$\chi_0^2 = \frac{1}{n-k} \sum_{i=1}^{n} \frac{(x_i - \bar{x})^2}{\sigma_i^2} \tag{7.12}$$

where $x_i \pm \sigma_i$ are the individual measurements, $\bar{x}$ is the weighted mean value, n =12 is the number of measurements, and k =1 is the number of calculated parameters. Ideally, if the assumption is valid, we should expect $\chi_0^2 \lesssim 1$. Conventionally, the hypotesis is rejected if $\chi_0^2 > M_{n,k}$, where $M_{n,k}$ is the critical value corresponding to a probability of less than 5% for the hypothesis to be valid. In our case, the final error bars account for potential uncorrected systematics and biases in the detrending method, hence χ_0^2 =1.0 only represents an upper limit. I found χ_0^2 =0.42 for the eclipse depth, and χ_0^2 =1.0 for the phase constant, confirming the non-detection of any inter-epoch variability. By considering the MCMC error bars without the σ_{ICA} contribution, the χ_0^2 values increase up to 0.56 for the eclipse depth and 1.7 for the phase constant. These results suggest that systematics errors are present in the residuals, which do not significantly affect the transit depth at different epochs, but they do affect the phase constant. Note that the reduced chi-squared tests whether the actual dispersion in the measurements is consistent within their error bars, but it is not sensitive to a uniform bias for all measurements, e.g. a constant shift. Hence, it is not sufficient alone to justify the use of the weighted mean as global estimate of a parameter. Additional tests, partly discussed in the previous section 7.2.4, show that the weighted mean result is very stable for the eclipse depth. The phase constant appears to be more depending on certain detrending options, in particular background subtraction. In this case, the adopted weighted mean error bar of 2.0×10^{-4} days^{-1} is a lower limit, valid with some caveats. In the worst-case scenario, the maximum error bar, calculated without scaling when combining multiple measurements, is 7×10^{-4} days^{-1}.

Comparison with a previous analysis of the same dataset

The results obtained with the wavelet pixel-ICA technique are consistent within 1 σ with the ones from a previous analysis reported in Wong et al. (2014) (see Figures 7.2 and 7.3). I obtained, on average, larger error bars by a factor 0.8 to 1.5 for the eclipse depth and 1.0 to 2.0 for the phase constant compared to the ones in the literature. The factors for the weighted mean eclipse depth and phase constant are 0.9 and 1.4, respectively. Slightly larger error bars are a worthwhile trade-off for much higher objectivity, which derives from the lack of assumptions about the origin of instrument systematics and their functional forms in the ICA detrending method. I also note that, despite the larger nominal error bars, the dispersions in the best parameter estimates are slightly smaller than the ones calculated from the results reported in Wong et al. (2014) (see

Table 7.4).

The reduced chi-squared values inferred from their individual parameter estimates are χ^2_0 =0.86 for the eclipse depth, and χ^2_0 =4.3 for the phase constant. While the first χ^2_0 value is consistent with the hypothesis of a constant transit depth within the quoted error bars, the second χ^2_0 value indicates that the analogous hypothesis for the phase constant can be rejected (less than 0.1% probability of being true). This may suggest either that they were able to detect some astrophysical variability of the phase-curve's slope, or that their individual error bars are under-estimated by a factor ∼2. Given that the astrophysical slope is degenerate with other instrumental trends, such as long-term position drift of the telescope and possible thermal heating, it is possible that their individual error bars do not fully accounts for these degeneracies, as the authors themselves state. If this is the case, I observe that their final error bar on the phase constant, derived by a joint fit of all eclipses, could be equally under-estimated, because it is not guaranteed that residual systematic errors cancel out over multiple observations as if they were random errors. Note that the joint fit approach is theoretically valid under the same assumptions for which the weighted mean is valid, and the two approaches are expected to lead to very similar results (I checked that this happens in this case). In conclusion, the reanalysis in this Thesis confirms the results reported in Wong et al. (2014) for the eclipse depth, and relative inter-epoch variability, but not the 4 σ detection of a non-flat phase-curve's slope during the eclipse, as larger error bars are needed to account for the possible residual systematics.

Table 7.4: Weighted mean parameter results, dispersions and reduced chi-squared values obtained in this Thesis and reported in Wong et al. (2014).

Eclipse depth	This work	Wong et al. 2014
Best estimate	$(1.57 \pm 0.03)\times10^{-3}$	$1.580^{+0.033}_{-0.039}\times10^{-3}$
Dispersion	7.2×10^{-5}	8.4×10^{-5}
χ^2_0	0.42	0.86
Phase constant (days^{-1})	This work	Wong et al. 2014
Best estimate	$(4.4 \pm 2.0)\times10^{-4}$	$6.0^{+1.3}_{-1.6}\times10^{-4}$
Dispersion	7.0×10^{-4}	11.3×10^{-4}
χ^2_0	1.0	4.3

7.3 The IRAC Data Challenge 2015

To assess the repeatability, reliability, and accuracy of post-cryogenic observations with IRAC, the Spitzer Science Center (SSC) organized the IRAC Data Challenge 2015 (Krick et al., 2015). The SSC made available to the public synthetic data sets containing ten simulated eclipse observation of the exoplanet XO3b generated with the IRACSIM package (Krick et al., 2015), using

the same observing mode of the real datasets analysed in Section 7.2 (PID: 90032). The simulations adopted constant astrophysical parameters and number of frames (15,232), while varying the observing conditions, such as pointing fluctuations, drifts and phase of the first frame. All teams working in the field and using *Spitzer*/IRAC data were invited to test their detrending methods both over the synthetic and real datasets. No constraints about the data analysis, e.g. photometric aperture, background definition, fitting strategies, other astrophysical and instrument parameters to adopt, were given by the SSC, so that the full detrending pipelines were tested. The final results are discussed by Ingalls et al. (2016), together with more technical details relative to the simulations.

The following techniques have been tested by the teams participating to the data challenge: BiLinearly-Interpolated Subpixel Sensitivity mapping (BLISS, Stevenson et al., 2012), Kernel Regression (KR/Data, Wong et al., 2014, KR/PMap, Krick et al., 2016), Segmented Polynomial K2 pipeline (SP(K2), Buzasi et al., 2015), Pixel Level Decorrelation (PLD, Deming et al., 2015), Gaussian Process regression (GP, Evans et al., 2015) and wavelet pixel-ICA (Morello et al., 2016). A series of statistical estimators is used to compare the results obtained with the different techniques and to assess their robustness:

1. the weighted mean eclipse depth and relative uncertainty over the two sets of ten observations,

$$\overline{D} = \frac{\sum_{i=1}^{10} \frac{D_i}{\sigma_i^2}}{\sum_{i=1}^{10} \frac{1}{\sigma_i^2}} \tag{7.13}$$

$$\sigma_{orig} = \frac{1}{\sum_{i=1}^{10} \frac{1}{\sigma_i^2}}, \tag{7.14}$$

   where $D_i \pm \sigma_i$ are the individual eclipse depth estimates;

2. the mean eclipse depth uncertainty,

$$\overline{\sigma} = \frac{1}{10} \sum_{i=1}^{10} \sigma_i \tag{7.15}$$

3. the dispersion factor, required to make $\chi_0^2 = 1$, if the original $\chi_0^2 > 1$,

$$f_{dis}^2 = max \left(\sum_{i=1}^{10} \frac{(D_i - \overline{D})^2}{9\sigma_i^2},\ 1 \right); \tag{7.16}$$

4. the total uncertainty in the mean eclipse depth, after being corrected for the dispersion

factor,

$$\sigma_{TOT} = f_{dis}\sigma_{orig}; \tag{7.17}$$

5. the sample standard deviation in eclipse depth,

$$SD = \sqrt{\frac{1}{9}\sum_{i=1}^{10}(D_i - \overline{D})^2}; \tag{7.18}$$

6. the repeatability, R, i.e. the standard deviation in differences between pairs of eclipse depth measurements;

7. the reliability,

$$r = \frac{\sigma_{phot}}{SD}, \tag{7.19}$$

where σ^2_{phot} is the theoretical photon noise variance;

8. the mean bias,

$$\overline{B} = \overline{D} - D_t, \tag{7.20}$$

where D_t is the input eclipse depth;

9. the root mean square deviation from the input eclipse depth,

$$RMSE = \sqrt{\frac{1}{9}\sum_{i=1}^{10}(D_i - D_t)^2}; \tag{7.21}$$

10. the accuracy,

$$a = \frac{\sigma_{phot}}{RMSE}. \tag{7.22}$$

The last three estimators, i.e. $\overline{B}$, $RMSE$ and a, can be computed only for the simulations.

7.3.1 Results and discussion

The results reported in this Section are taken from Ingalls et al. (2016) and Morello et al. (2016).

Real data

Figure 7.4 compares the weighted mean results obtained for the real datasets with the different pipelines. It shows that most of the detrending pipelines lead to consistent results within 1 σ, according to the various definitions of σ given above. In particular, ICA, PLD and KR/Data constitutes the triple with the smallest range in eclipse depth estimates, i.e. only 13 ppm. The

original error bars for five of the detrending pipelines, including ICA, are well consistent with their inter-epoch dispersions (f_{dis} =1), the only exceptions are for BLISS (f_{dis} =1.5) and SP(K2) (f_{dis} =2.8).

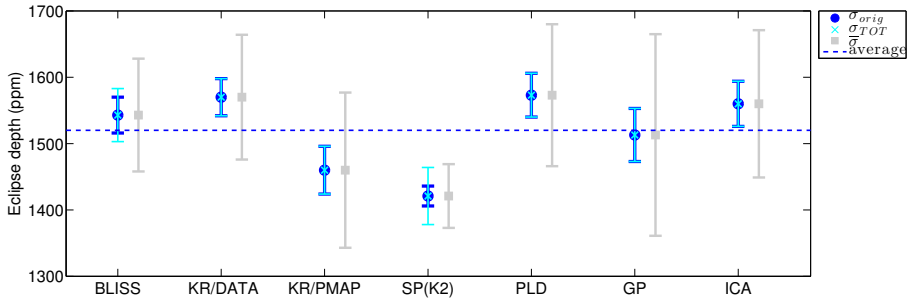

Figure 7.4: Weighted mean eclipse depth results obtained with the different pipelines for the real observations analysed for the IRAC Data Challenge 2015.

Figure 7.5 reports the repeatability and reliability estimates, sorted according to decreasing performances. ICA is the most repeatable and the most reliable technique, closely followed by the KR techniques. The overall standard deviations of the individual ICA measurements is ∼30% larger than the photon noise limit. It is worth noting that, at least in principle, there might be some real variability of the planet that would prevent achieving the theoretical photon noise limit for the repeated observations.

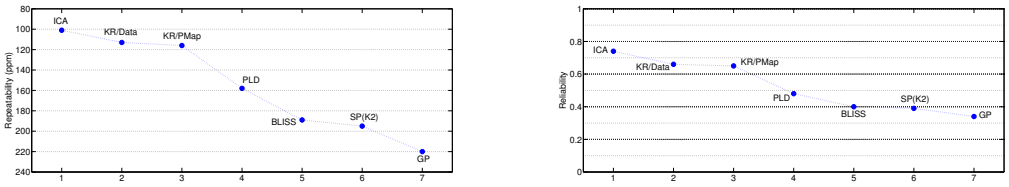

Figure 7.5: Left panel: repeatability of the detrending pipelines for the real datasets analysed for the IRAC Data Challenge 2015. Right panel: the same for reliability.

Simulated data

Figure 7.6 compares the weighted mean results obtained for the simulated datasets with the different pipelines, and also with the input eclipse depth value. Even in this case, most detrending pipelines lead to consistent results within 1 σ. However, this time the original error bars appear to be slightly underestimated relative to the inter-epoch dispersions, except for ICA and BLISS, which are consistent with f_{dis} =1 within the statistical error. The most likely cause of this discrepancy compared to the real datasets is the use of slightly larger systematics for the simulated ones. All measurements appear to be biased to eclipse depths smaller than the true value, except for the PLD value, which is 5 ppm larger. The PLD pipeline differs from the other

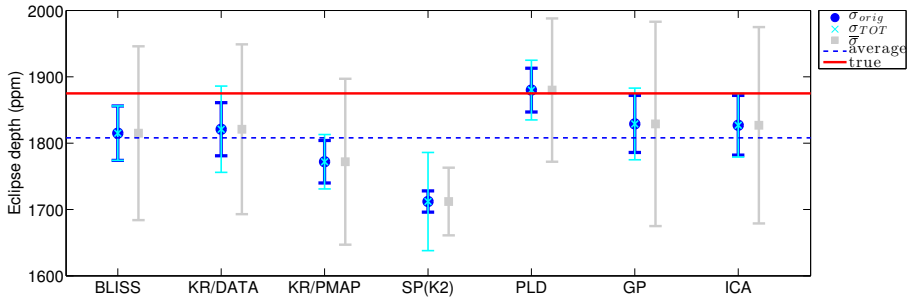

Figure 7.6: Weighted mean eclipse depth results obtained with the different pipelines for the simulated observations analysed for the IRAC Data Challenge 2015.

ones in the use of a quadratic polynomial to approximate the out-of-eclipse phase-curve, while the other ones reported results obtained with a flat or a linear approximation to the phase-curve. By fitting the three eclipse models to a noiseless input light-curve, it has been found that the eclipse depth is biased by -51 ppm for the flat phase-curve model, -27 ppm for the linear model and -2 ppm for a quadratic model. This accounts for $\sim$60% of the bias obtained with ICA, as I adopted a linear model. Note that this issue is specific to the nature of the input astrophysical model for the simulations, as the real phase-curve shape is unknown. Nonetheless, it indicates the potential error due to the phase-curve model function. Figure 7.7 reports the repeatability and reliability estimates. Figure 7.8 reports the accuracy and the bias divided by the original standard deviations, sorted according to decreasing performances. BLISS, PLD and ICA are the most repeatable, reliable and accurate techniques. While the accuracy depends on the dispersion relative to the true eclipse depth value, the latter estimator is a measure of the bias in units of σ_{orig}. If $\overline{B}/\sigma_{orig} \lesssim 1$, this indicates that the error bars assessed by the pipeline are sufficiently large to include the bias, as it is the case for PLD, ICA and GP; the $\overline{B}/\sigma_{orig}$ values for the other pipelines are BLISS (1.3), KR/Data (1.4), KR/PMap (3.2) and SP(K2) (10.1).

7.3.2 Conclusions

The results of the IRAC Data Challenge 2015 indicates that, based both on the analysis of the real and simulated datasets, the wavelet pixel-ICA pipeline performs as well or better than other state-of-the-art detrending algorithms for *Spitzer*/IRAC.

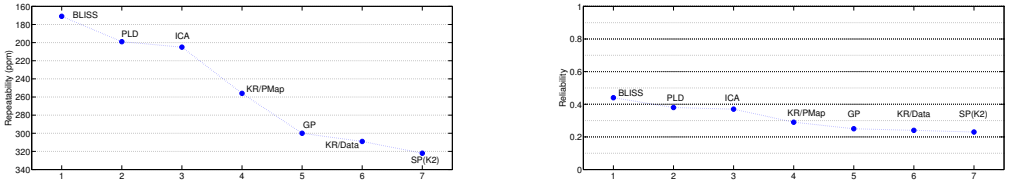

Figure 7.7: Left panel: repeatability of the detrending pipelines for the simulated datasets analysed for the IRAC Data Challenge 2015. Right panel: the same for reliability.

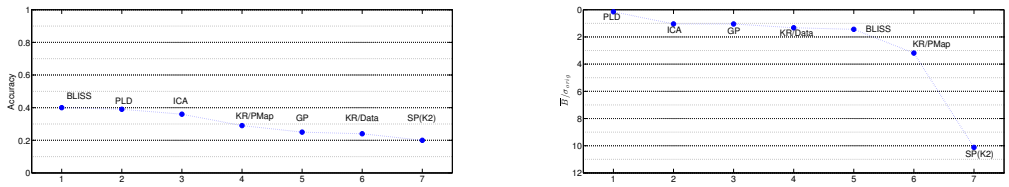

Figure 7.8: Left panel: accuracy of the detrending pipelines for the simulated datasets analysed for the IRAC Data Challenge 2015. Right panel: the same for the mean bias over the original weighted error bars.

Chapter 8

Application to *HST*/WFC3 transit observations

8.1 Hubble Space Telescope

The Hubble Space Telescope (HST) is a space-borne observatory launched in 1990. It is one of the four NASA Great Observatories, the one originally dedicated to cover the visible and near-UV regions of the electromagnetic spectrum. It follows a geocentric orbit. The telescope has an aperture of 2.4 m diameter. It is the only telescope designed to be serviced in space by astronauts. This function allowed replacing the old instruments with new ones during its operational time. A scheme of the HST's equipment history is shown in Figure 8.1. Currently operating instruments are:

- the Wide Field Camera 3 (WFC3), a versatile camera with two channels collecting light in the 200–1,000 and 800–1,700 nm spectral ranges, each channel equipped with a variety of broad- and narrow-band filters, prisms and grisms enabling wide-field low-resolution spectroscopy;
- the Near Infrared Camera and Multi-Object Spectrometer (NICMOS), which contains three near-IR detectors in three optical channels providing high-resolution ($\sim 0.1''$), coronagraphic and polarimetric imaging, and slitless spectroscopy in the range 800–2,400 nm;
- the Space Telescope Imaging Spectrograph (STIS), with three detector arrays covering the far-UV to the near-IR (115–170, 160–310 and 200–1,030 nm);
- the Advanced Camera for Surveys (ACS), with the Wide Field Channel (WFC) observing an effective field of view $202'' \times 202''$ in the spectral range 350–1,100 nm, and the Solar Blind

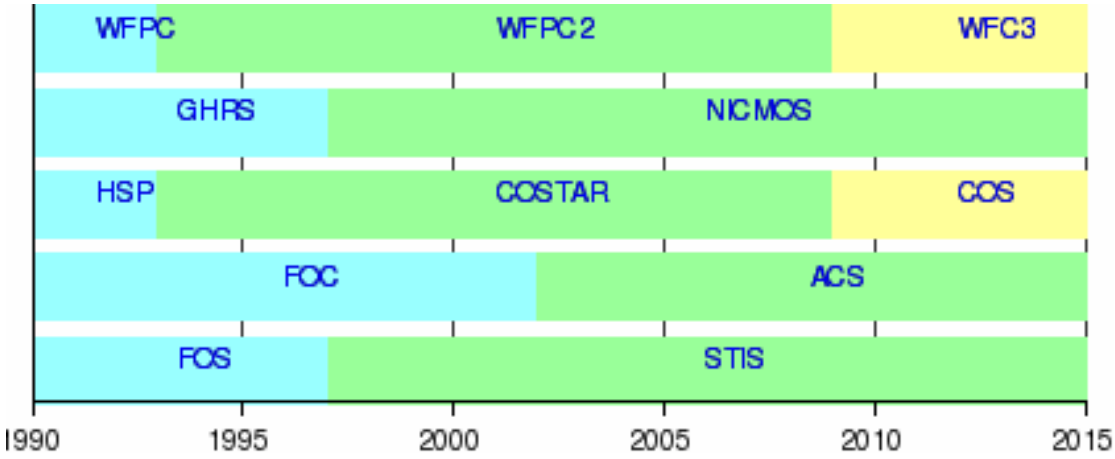

Figure 8.1: Instruments operating on the Hubble Space Telescope.

Channel (SBC) observing a smaller 25″×25″ field of view in the spectral range 115–170 nm;

- the Cosmic Origins Spectrograph (COS), which is designed for ultraviolet spectroscopy of faint point sources with eight different grisms.

8.1.1 The Wide Field Camera 3 (WFC3)

Overview

WFC3 is the latest and most technologically advanced instrument installed onboard the HST. WFC3 features two UV/visible detecting CCDs, each 2,048×4,096 pixels, and a separate IR detector of 1,024×1,024 pixels. The optical channel covers a 164″×164″ (2.7′×2.7′) field of view with 0.04″/pixel. The near-IR channel has a field of view of 135″×127″ (2.3′×2.1′) and 0.13″/pixel scale.

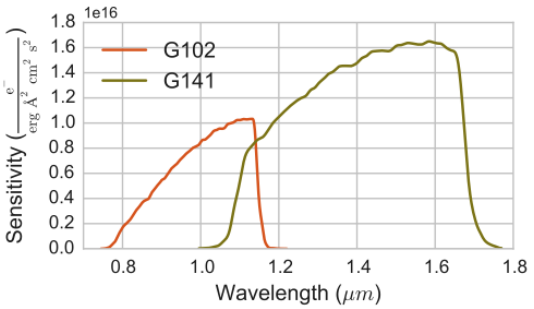

Figure 8.2: *HST*/WFC3 G102 and G141 grism sensitivity. Image from Varley and Tsiaras (2015).

Scanning-mode observations

Exoplanet transit spectra were initially observed with WFC3 in HST's traditional staring mode, where the telescope pointing is fixed on the target star. The scanning-mode was introduced in 2011 during HST Cycle 19, and is now the preferred mode to perform exoplanet spectroscopy. This mode slews the telescope during an exposure under the control of either the fine-guidance sensors (FGS, for scans speeds below 1″/s) or gyroscope-only control (for scan speeds up to

7.84″/s). The scanning mode has been introduced to observe bright targets that would normally saturate the detector. It can also achieve higher signal-to-noise ratios as more photons from the source can be collected and spread over the detector before saturation.

UCL pipeline

Tsiaras et al. (2015) developed a pipeline to analysing *HST*/WFC3 scanning-mode data, using the *raw* data frames as input rather than the more commonly used *ima* frames. The following are the main steps of the pipeline:

1. data reduction, i.e. bias drift correction, zero read subtraction, non-linearity correction, dark current subtraction, gain variations calibration, sky background subtraction, bad pixels and cosmic rays correction;
2. wavelength calibration and extraction of 1D spectra;
3. simultaneous fitting of the astrophysical model and instrument systematics.

The main instrument systematics are: an approximately exponential short-term ramp, with 1-orbit duration, and an approximately linear long-term ramp. They are corrected by the pipeline parametrically and/or using the white light-curve as a model for the systematics.

8.2 Stripe-ICA

The algorithm that I have developed to decorrelate *HST*/WFC3 data is called "stripe-ICA", as it uses the time series registered by individual stripes, rather than "pixel light-curves", as input for the ICA. This is possible if each spatial scan is subsampled through more than one non-destructive read. A stripe is defined as the difference between two consecutive non-destructive reads. By taking the corresponding stripes from each spatial scan, a set of quasi-simultaneous stripe light-curves is obtained. One set of these light-curves can be obtained for the white light-curve, as well as one set for each spectral bin. In this Thesis, I adopted the stripe time series computed by Mario Damiano using the Tsiaras et al. pipeline without correction of the instrument systematics. The ICA is applied over each set of quasi-simultaneous light-curves separately, without mixing the information from multiple wavelengths.

One of the independent components mostly contains the transit signals, the others are simultaneously fitted, together with a transit model, to a reference light-curve. This is analogous to method 3 described for the pixel-ICA pipeline (see Section 5.2). Here, I considered the following two options:

1. summing the relevant stripe light-curves to obtain a unique reference light-curve for each spectral bin (in other words, summing along the spatial direction);

2. fitting each stripe light-curve alone, then taking the weighted mean for each spectral bin.

Hereafter, I refer to the two spectra as "stacked" and "weighted", respectively.

An evolution of the simple stripe-ICA decorrelation includes the residuals obtained for the white light-curve, summed over the stripes, as an additional component. This accounts for possible systematics common to all wavelength bins, which were not separated by the ICA, and it is equivalent to using the white light-curve as a model for the systematics.

The final error bars are calculated according to Equations 5.2 and 5.3 (method 3).

8.3 Transit of HAT-P 32b

I analyzed the observation of a transit of the hot-Jupiter HAT-P 32b taken with the G141 grism of the *HST*/WFC3 instrument. It consists of a single visit spanning five HST orbits. The scans are subsampled allowing the extraction of 12 stripes. The results of this analysis are as yet unpublished.

8.3.1 Analysis

Fixed and free parameters

Each stripe has been divided in 20 spectral bins. Table 8.1 includes the wavelength limits and the four limb darkening coefficients (Equation 3.14), computed with the modified version of ATLAS9 code described in Howarth (2011b). The orbital period, P, and the a_R, i, e and ω parameters are fixed to values reported in Gibson et al. (2013). A possible shift in the mid-transit time, t_{mid}, is fitted to the white light-curve, as well as the square-root transit depth, p. For the spectral light-curves, p and the normalization factor are the only free parameters to determine.

8.3.2 Results

The stripe light-curves are noisier than the summed ones, mainly due to correlated jitter noise. The independent components are very effective in correcting this source of noise. Independently from the choice of the reference light-curves, for the particular observation analysed, the detrended light-curves are similar to the relevant sum over the stripes. This is attributable, at least in part, to the low amplitude of the systematic effects in the raw summed light-curves. For the same reason, the improvement caused by the inclusion of the additional component equal

to the white light-curve residuals is hard to visualize, although it is statistically significant, as it shrinks the error bars by an average factor ∼0.88. Figure 8.3 shows an example of two raw light-curves, single stripe and summed, and the detrended ones, without and with the white residuals component. Figure 8.4 reports the spectra obtained with the four methods described in Section 8.2, i.e. stacked or weighted and ICA only or with the white residuals component. The weighted error bars are not scaled according to the standard weighted mean formula, because their analyses are not independent, especially not the ICA decomposition. In this way, the stacked and the weighted approaches lead to very similar error bars.

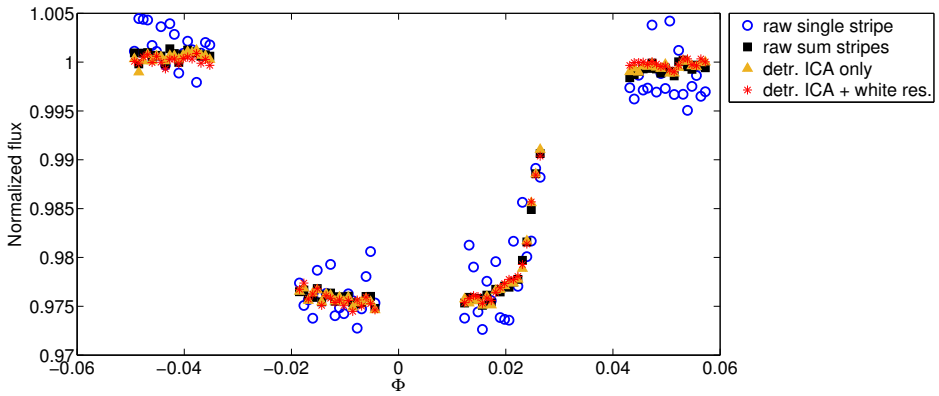

Figure 8.3: Example of light-curves for the spectral bin 1.3657−1.3901 μm: (blue circles) raw single stripe, (black squares) raw summed over the stripes, (orange triangles) detrended with ICA only and (red stars) detrended with ICA and white residuals component.

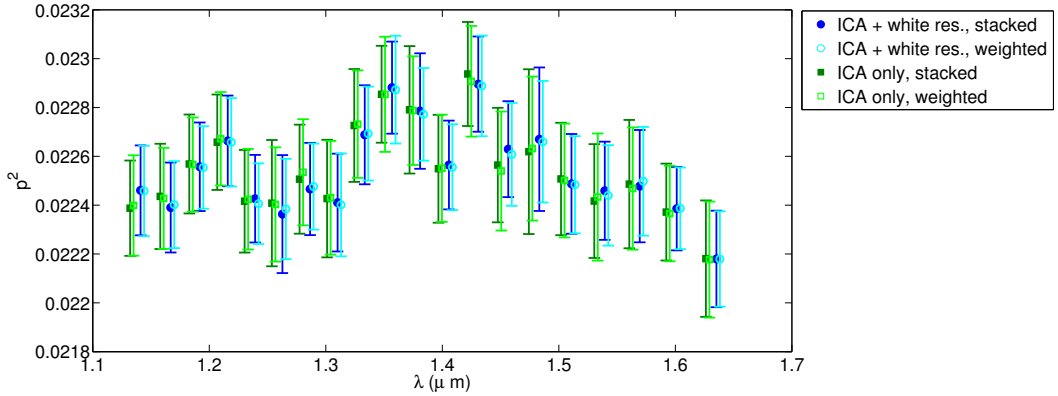

Figure 8.4: Spectra obtained with four methods: (blue, full circles) ICA plus with residuals component, stacked, (cyan, empty circles) ICA plus with residuals component, weighted, (dark green, full squares) ICA only, stacked, and (light green, empty squares) ICA only, weighted. An horizontal displacement has been introduced to make easier visualization.

Table 8.1 reports the final spectrum for the case stripe ICA with white residuals component and stacked reference light-curves.

λ_1 (μm)	λ_2 (μm)	c_1	c_2	c_3	c_4	p^2
1.1250	1.6500	0.60334	-0.22301	0.28133	-0.13986	
1.1250	1.1511	0.632741	-0.481904	0.701108	-0.306091	2.246±0.018
1.1511	1.1767	0.619205	-0.434713	0.64011	-0.282483	2.239±0.018
1.1767	1.2011	0.614294	-0.41589	0.610565	-0.272242	2.256±0.018
1.2011	1.2247	0.599151	-0.360648	0.544934	-0.247917	2.266±0.019
1.2247	1.2480	0.584001	-0.29953	0.465487	-0.216442	2.243±0.018
1.2480	1.2716	0.581928	-0.282551	0.441745	-0.210655	2.236±0.024
1.2716	1.2955	0.58946	-0.229732	0.322997	-0.169253	2.247±0.019
1.2955	1.3188	0.57237	-0.227002	0.362724	-0.181489	2.241±0.020
1.3188	1.3421	0.569522	-0.202303	0.325228	-0.166816	2.269±0.020
1.3421	1.3657	0.564634	-0.163366	0.265035	-0.14235	2.288±0.019
1.3657	1.3901	0.561817	-0.127278	0.200548	-0.113503	2.279±0.024
1.3901	1.4152	0.561832	-0.0979712	0.148201	-0.0914278	2.256±0.018
1.4152	1.4406	0.572262	-0.100901	0.133369	-0.0848254	2.290±0.020
1.4406	1.4667	0.58462	-0.111943	0.124656	-0.0799948	2.263±0.020
1.4667	1.4939	0.600205	-0.136878	0.140204	-0.0874595	2.267±0.029
1.4939	1.5219	0.609784	-0.134319	0.11158	-0.0721681	2.249±0.020
1.5219	1.5510	0.626375	-0.139701	0.0839621	-0.0555132	2.246±0.020
1.5510	1.5819	0.647904	-0.193435	0.120068	-0.0635888	2.248±0.023
1.5819	16145	0.663831	-0.223633	0.124246	-0.0583813	2.239±0.017
1.6145	1.6500	0.686226	-0.267069	0.137329	-0.0557593	2.218±0.020

Table 8.1: Spectral bins, limb darkening coefficients and transit depth results

8.3.3 Discussion

Figure 8.5 compares my final spectrum with the spectrum calculated with the Tsiaras et al. pipeline (priv. comm. of Mario Damiano). I obtained larger error bars by a factor ∼1.8,

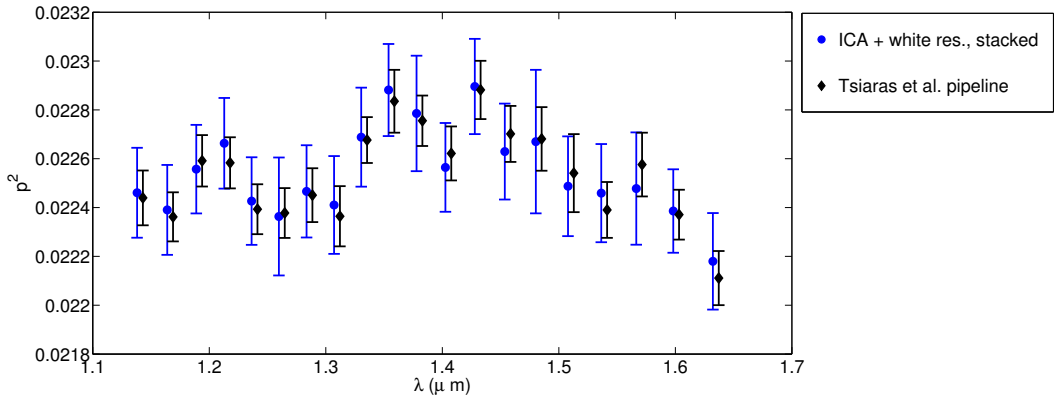

Figure 8.5: Comparing spectra: (blue circles) spectrum obtained with ICA + white residuals component, stacked, and (black rhomboids) spectrum computed with the Tsiaras et al. pipeline (priv. comm. of Mario Damiano).

in average. This is the trade-off for a higher objectivity, in this case. The robustness of the weighted approach indicates that it might be possible to decrease the error bars. This will be investigated in future studies and also using the Wayne simulator (Varley and Tsiaras, 2015).

Chapter 9

Summary and Conclusion

Characterizing exoplanetary atmospheres through transit and eclipse spectroscopy requires accurate measurements at the level of at least 1 part in 10^4 in stellar flux. Current instruments are not designed to achieve this precision, therefore correcting for the instrument systematics is a critical step of the data analysis. This is further complicated by the potential contamination of other astrophysical signals, e.g. stellar activity, and the large degeneracy of interpretation. Controversial results are reported in the literature, also based on reanalyses of the same datasets with different systematics detrending pipelines. Most of the methods adopted by several teams rely on some assumptions about the mechanisms causing the instrument systematics and apply parametric corrections.

In this Thesis, I adopted blind signal–source separation (BSS) methods to detrend the observed data. At the heart of these methods is the use of the Independent Component Analysis (ICA) of simultaneous time series. In particular, I developed two algorithms specialized to detrending individual photometric observations, i.e. pixel-ICA and wavelet pixel-ICA, the latter being an evolution with extended applicability to faint signals and low signal-to-noise observations, and another algorithm, i.e. stripe-ICA, specially designed to detrend spectroscopic observations obtained with the new *HST*/WFC3 instrument in the scanning-mode. The two techniques are different from previous applications of ICA proposed in the literature (e.g. Waldmann, 2012), mainly because they can be applied to single observations taken with instruments with a different design, and, in particular, without mixing the information at multiple wavelengths. An additional advantage, deriving from the use of time series at the same wavelengths to detrend the transit signal, is that wavelength-dependent effects on the transit shape, e.g. stellar limb darkening, are not present, allowing a more robust extraction of the signal. The pixel-ICA and wavelet pixel-ICA are tested over a series of cryogenic and post-cryogenic *Spitzer*/IRAC observa-

tions, as well as synthetic datasets, showing superior performances compared to state-of-the-art detrending pipeline specifically designed for those datasets.

A reanalysis of the existing archive datasets with these new techniques will cast light onto the unresolved controversies in the literature. With the advent of newer and more precise instruments, the use of optimal detrending techniques will still be crucial to separate the various astrophysical signals and to push the limits of detections to even smaller signals, such as the spectroscopic signatures of the atmospheres of Earth-sized exoplanets.

Bibliography

E. Agol, N. B. Cowan, H. A. Knutson, D. Deming, J. H. Steffen, G. W. Henry, and D. Charbonneau. The Climate of HD 189733b from Fourteen Transits and Eclipses Measured by Spitzer. *ApJ*, 721:1861, 2010.

F. Allard and P. H. Hauschildt. Model Atmospheres for M (Sub)Dwarfs Stars. I. The Base Model Grid. *ApJ*, 445:433, 1995.

F. Allard and D. Homeier. Phoenix Web Simulator. `https://phoenix.ens-lyon.fr/simulator`, 2014.

F. Allard, P. H. Hauschildt, D. R. Alexander, A. Tamanai, and A. Schweitzer. The Limiting Effects of Dust in Brown Dwarf Model Atmosphere. *ApJ*, 556:357, 2001.

R. Alonso, M. Barbieri, M. Rabus, H. J. Deeg, J. A. Belmonte, and J. M. Almenara. Limits to the planet candidate GJ 436c. *A&A*, 487:L5, 2008.

J. Aumont and J. F. Macías-Pérez. Blind component separation for polarized observations of the cosmic microwave background. *MNRAS*, 376:739, 2007.

S. Ballard, D. Charbonneau, D. Deming, H. A. Knutson, J. L. Christiansen, M. J. Holman, D. Fabrycky, S. Seager, and M. F. A'Hearn. A Search for a Sub-Earth-Sized Companion to GJ 436 and a Novel Method to Calibrate Warm Spitzer IRAC Observations. *PASP*, 122:1341, 2010a.

S. Ballard, J. L. Christiansen, D. Charbonneau, D. Deming, M. J. Holman, D. Fabrycky, M. F. A'Hearn, D. D. Wellnitz, R. K. Barry, M. J. Kuchner, T. A. Livengood, T. Hewagama, J. M. Sunshine, D. L. Hampton, C. M. Lisse, S. Seager, and J. F. Veverka. A Search for Additional Planets in the NASA EPOXI Observations of the Exoplanet System GJ 436. *ApJ*, 716:1047, 2010b.

T. Barman. Identification of Absorption Features in an Extrasolar Planet Atmosphere. *ApJL*, 661:L191, 2007.

J. K. Barstow, S. Aigrain, P. G. J. Irwin, L. N. Fletcher, and J.-M. Lee. Constraining the atmosphere of GJ 1214b using an optimal estimation technique. *MNRAS*, 434:2616, 2013.

J. P. Beaulieu, S. Carey, I. Ribas, and G. Tinetti. Primary Transit of the Planet HD 189733b at 3.6 and 5.8 μm. *ApJ*, 677:1343, 2008.

J. P. Beaulieu, D. M. Kipping, V. Batista, G. Tinetti, I. Ribas, S. Carey, J. A. Noriega-Crespo, C. A. Griffith, G. Campanella, S. Dong, J. Tennyson, R. J. Barber, P. Deroo, S. J. Fossey, D. Liang, M. R. Swain, Y. Yung, and N. Allard. Water in the atmosphere of HD 209458b from 3.6-8 μm IRAC photometric observations in primary transit. *MNRAS*, 409:963, 2010.

J.-P. Beaulieu, G. Tinetti, D. M. Kipping, I. Ribas, R. J. Barber, J. Y.-K. Cho, I. Polichtchouk, J. Tennyson, S. N. Yurchenko, C. A. Griffith, V. Batista, I. Waldmann, S. Miller, S. Carey, O. Mousis, S. J. Fossey, and A. Aylward. Methane in the Atmosphere of the Transiting Hot Neptune GJ436B? *ApJ*, 731:16, 2011.

A. Bell and T. Sejnowski. The 'independent components' of natural scenes are edge filters. *Vision Research*, 37:3327, 1997.

A. Belouchrani, K. Abed-Meraim, J. F. Cardoso, and E. Moulines. *IEEE Trans. Signal Processing*, 45:434, 1997.

B. Benneke and S. Seager. Atmospheric Retrieval for Super-Earths: Uniquely Constraining the Atmospheric Composition with Transmission Spectroscopy. *ApJ*, 753:100, 2012.

D. P. Bennett and S. H. Rhie. Detecting Earth-Mass Planets with Gravitational Microlensing. *ApJ*, 472:660, 1996.

J.-L.-L. Beuzit, M. Feldt, K. Dohlen, D. Mouillet, P. Puget, F. Wildi, F., L. Abe, J. Antichi, J., A. Baruffolo, P. Baudoz, A. Boccaletti, M. Carbillet, J. Charton, R. Claudi, M. Downing, C. Fabron, P. Feautrier, E. Fedrigo, T. Fusco, J.-L. Gach, R. Gratton, T. Henning, N. Hubin, F. Joos, M. Kasper, M. Langlois, R. Lenzen, C. Moutou, A. Pavlov, C. Petit, J. Pragt, P. Rabou, F. Rigal, R. Roelfsema, G. Rousset, M. Saisse, H.-M. Schmid, E. Stadler, C. Thalmann, M. Turatto, S. Udry, F. Vakili, and R. Waters. SPHERE: a 'Planet Finder' instrument for the VLT. *Proc. SPIE*, 7014:701418, 2008.

M. Bonnefoy, A. Zurlo, J. L. Baudino, P. Lucas, D. Mesa, A.-L. Maire, A. Vigan, R. Galicher, D. Homeier, F. Marocco, R. Gratton, G. Chauvin, F. Allard, S. Desidera, M. Kasper, C. Moutou, A.-M. Lagrange, J. Antichi, A. Baruffolo, J. Baudrand, J.-L. Beuzit, A. Boccaletti, F. Cantalloube, M. Carbillet, J. Charton, R. U. Claudi, A. Costille, K. Dohlen, C. Dominik, D. Fantinel, P. Feautrier, M. Feldt, T. Fusco, P. Gigan, J. H. Girard, L. Gluck, C. Gry, T. Henning, M. Janson, M. Langlois, F. Madec, Y. Magnard, D. Maurel, D. Mawet, M. R. Meyer, J. Milli, O. Moeller-Nilsson, D. Mouillet, A. Pavlov, D. Perret, P. Pujet, S. P. Quanz, S. Rochat, G. Rousset, A. Roux, B. Salasnich, G. Salter, J.-F. Sauvage, H. M. Schmid, A. Sevin, C. Soenke, E. Stadler, M. Turatto, S. Udry, F. Vakili, Z. Wahhaj, and F. Wildi. First light of the VLT planet finder SPHERE. IV. Physical and chemical properties of the planets around HR8799. *A&A*, 587:A58, 2016.

F. Bouchy, S. Udry, M. Mayor, C. Moutou, F. Pont, N. Iribarne, R. da Silva, S. Ilovaisky, D. Queloz, N. C. Santos, D. Ségransan, and S. Zucker. ELODIE metallicity-biased search for transiting Hot Jupiters. II. A very hot Jupiter transiting the bright K star HD 189733. *A&A*, 444:L15, 2005.

D. L. Buzasi, L. Carboneau, C. Hessler, A. Lezcano, and H. Preston. Serendipitous Science from the K2 Mission. *ArXiv e-prints*, 1511.09069, 2015.

C. Cáceres, V. D. Ivanov, D. Minniti, D. Naef, C. Melo, E. Mason, F. Selman, and G. Pietrzynski. High cadence near infrared timing observations of extrasolar planets. I. GJ 436b and XO-1b. *A&A*, 507:481, 2009.

S. Calchi Novati, A. Gould, A. Udalski, J. W. Menzies, I. A. Bond, Y. Shvartzvald, R. A. Street, M. Hundertmark, C. A. Beichman, J. C. Yee, S. Carey, R. Poleski, J. Skowron, S. Kozlowski, P. Mróz, P. Pietrukowicz, G. Pietrzyński, M. K. Szymański, I. Soszyński, K. Ulaczyk, Ł. Wyrzykowski, The OGLE collaboration, M. Albrow, J. P. Beaulieu, J. A. R. Caldwell, A. Cassan, C. Coutures, C. Danielski, D. Dominis Prester, J. Donatowicz, K. Lončarić, A. McDougall, J. C. Morales, C. Ranc, W. Zhu, The PLANET collaboration, F. Abe, R. K. Barry, D. P. Bennett, A. Bhattacharya, D. Fukunaga, K. Inayama, N. Koshimoto, S. Namba, T. Sumi, P. J. Suzuki, D. andTristram, Y. Wakiyama, A. Yonehara, The MOA collaboration, D. Maoz, S. Kaspi, M. Friedmann, The Wise group, E. Bachelet, R. Figuera Jaimes, D. M. Bramich, Y. Tsapras, K. Horne, C. Snodgrass, J. Wambsganss, I. A. Steele, N. Kains, The RoboNet collaboration, V. Bozza, M. Dominik, U. G. Jørgensen, K. A. Alsubai, S. Ciceri, G. D'Ago, T. Haugbølle, F. V. Hessman, T. C. Hinse, D. Juncher, L. Korhonen, H.and Mancini, A. Popovas, M. Rabus, S. Rahvar, G. Scarpetta, R. W. Schmidt, J. Skottfelt, J. Southworth, D. Starkey, J. Surdej, O. Wertz, M. Zarucki, The MiNDSTEp consortium, B. S. Gaudi, R. W. Pogge, D. L. DePoy, and The FUN collaboration. Pathway to the Galactic Distribution of Planets: Combined Spitzer and Ground-Based Microlens Parallax Measurements of 21 Single-Lens Events. *ApJ*, 804:20, 2015.

D. Charbonneau, T. M. Brown, D. W. Latham, and M. Mayor. Detection of Planetary Transits Across a Sun-like Star. *ApJL*, 529:L45, 2000.

D. Charbonneau, T. M. Brown, R. W. Noyes, and R. L. Gilliland. Detection of an Extrasolar Planet Atmosphere. *ApJ*, 568:377, 2002.

D. Charbonneau, L. E. Allen, S. T. Megeath, G. Torres, R. Alonso, T. M. Brown, R. L. Gilliland, D. W. Latham, G. Mandushev, F. T. O'Donovan, and A. Sozzetti. Detection of Thermal Emission from an Extrasolar Planet. *ApJ*, 626:523, 2005.

D. Charbonneau, H. A. Knutson, T. Barman, L. E. Allen, M. Mayor, S. T. Megeath, D. Queloz, and S. Udry. The Broadband Infrared Emission Spectrum of the Exoplanet HD 189733b. *ApJ*, 686:1341, 2008.

D. Charbonneau, Z. K. Berta, J. Irwin, C. J. Burke, P. Nutzman, L. A. Buchhave, C. Lovis, X. Bonfils, D. W. Latham, S. Udry, R. A. Murray-Clay, M. J. Holman, E. E. Falco, J. N. Winn, D. Queloz, F. Pepe, M. Mayor, X. Delfosse, and T. Forveille. A super-Earth transiting a nearby low-mass star. *Nature*, 462:891, 2009.

A. Claret. A new non-linear limb-darkening law for LTE stellar atmosphere models. Calculations for -5.0 log[M/H] +1, 2000 K = T_{eff} = 50000 K at several surface gravities. *A&A*, 363:1081, 2000.

A. Collier Cameron, V. A. Bruce, G. R. M. Miller, A. H. M. J. Triaud, and D. Queloz. Line-profile tomography of exoplanet transits - I. The Doppler shadow of HD 189733b. *MNRAS*, 403:151, 2010.

D. A. Content, R. Goullioud, J. P. Lehan, and J. E. Mentzell. Optical design trade study for the Wide Field Infrared Survey Telescope [WFIRST]. *Proc. SPIE*, 8146:81460Y, 2011.

D. A. Content, N. V. Armani, C. L. Baker, C. E. Jackson, D. M. Kahle, J. W. Kruk, J. P. Lehan, M. E. Melton, E. Mentzell, J. J. Miko, D. J. Palace, B. A. Pasquale, H. L. Peabody, B. S. Smith, W. F. Smith, J. W. Stewart, D. A. Vaughnn, A. Waczynski, and T. E. Wallace. Wide field instrument preliminary design for the Wide Field Infra-Red Survey Telescope. *Proc. SPIE*, 8860:88600F, 2013.

A. C. M. Correia, S. Udry, M. Mayor, J. Laskar, D. Naef, F. Pepe, D. Queloz, and N. C. Santos. The coralie survey for southern extra-solar planets - xiii. a pair of planets around hd 202206 or a circumbinary planet? *A&A*, 440:751, 2005.

J. L. Coughlin, G. S. Stringfellow, A. C. Becker, M. López-Morales, F. Mezzalira, and T. Krajci. New Observations and a Possible Detection of Parameter Variations in the Transits of Gliese 436b. *ApJL*, 689:L149, 2008.

N. B. Cowan and E. Agol. A Model for Thermal Phase Variations of Circular and Eccentric Exoplanets. *ApJ*, 726:82, 2011.

N. B. Cowan, P. Machalek, B. Croll, L. M. Shekhtman, A. Burrows, D. Deming, T. Greene, and J. L. Hora. Thermal phase variations of WASP-12b: defying predictions. *ApJ*, 747:82, 2012.

C. Danielski, P. Deroo, I. P. Waldmann, M. D. J. Hollis, G. Tinetti, and M. R. Swain. 0.94-2.42 μm Ground-based Transmission Spectra of the Hot Jupiter HD-189733b. *ApJ*, 785:35, 2014.

I. Daubechies. *Ten Lectures on Wavelets*. Soc. for Industrial Mathematics, 1992.

D. Deming, S. Seager, L. J. Richardson, and J. Harrington. Infrared radiation from an extrasolar planet. *Nature*, 434:740, 2005.

D. Deming, J. Harrington, G. Laughlin, S. Seager, S. B. Navarro, W. C. Bowman, and K. Horning. Spitzer Transit and Secondary Eclipse Photometry of GJ 436b. *ApJL*, 667:L199, 2007.

D. Deming, H. Knutson, J. Kammer, B. J. Fulton, J. Ingalls, S. Carey, A. Burrows, J. J. Fortney, K. Todorov, E. Agol, N. Cowan, J.-M. Desert, J. Fraine, J. Langton, C. Morley, and A. P. Showman. Spitzer Secondary Eclipses of the Dense, Modestly-irradiated, Giant Exoplanet HAT-P-20b Using Pixel-level Decorrelation. *ApJ*, 805:132, 2015.

B.-O. Demory, M. Gillon, T. Barman, X. Bonfils, M. Mayor, T. Mazeh, D. Queloz, S. Udry, F. Bouchy, X. Delfosse, T. Forveille, F. Mallmann, F. Pepe, and C. Perrier. Characterization of the hot Neptune GJ 436 b with Spitzer and ground-based observations. *A&A*, 475:1125, 2007.

B.-O. Demory, M. Gillon, J. de Wit, N. Madhusudhan, E. Bolmont, K. Heng, T. Kataria, N. Lewis, R. Hu, J. Krick, V. Stamenković, B. Benneke, S. Kane, and D. Queloz. A map of the large day-night temperature gradient of a super-Earth exoplanet. *Nature*, 532:207, 2016.

J.-M. Désert, A. Lecavelier des Etangs, G. Hébrard, D. K. Sing, D. Ehrenreich, R. Ferlet, and A. Vidal-Madjar. Search for Carbon Monoxide in the Atmosphere of the Transiting Exoplanet HD 189733b. *ApJ*, 699:478, 2009.

J.-M. Désert, J. Bean, E. Miller-Ricci Kempton, Z. K. Berta, D. Charbonneau, J. Irwin, J. Fortney, C. J. Burke, and P. Nutzman. Observational Evidence for a Metal-rich Atmosphere on the Super-Earth GJ1214b. *ApJL*, 731:L40, 2011.

H. Diamond-Lowe, K. B. Stevenson, J. L. Bean, M. R. Line, and J. J. Fortney. New Analysis Indicates No Thermal Inversion in the Atmosphere of HD 209458b. *ApJ*, 796:66, 2014.

D.L. Donoho. *IEEE Trans. on Inf. Theory*, 41:613, 1995.

D. Ehrenreich, G. Hébrard, A. Lecavelier des Etangs, D. K. Sing, J.-M. Désert, F. Bouchy, R. Ferlet, and A. Vidal-Madjar. A Spitzer Search for Water in the Transiting Exoplanet HD 189733b. *ApJL*, 668:L179, 2007.

T. M. Evans, S. Aigrain, N. Gibson, J. K. Barstow, D. S. Amundsen, P. Tremblin, and P. Mourier. A uniform analysis of HD 209458b Spitzer/IRAC light curves with Gaussian process models. *MNRAS*, 451:680, 2015.

G. G. Fazio, J. L. Hora, L. E. Allen, M. L. N. Ashby, P. Barmby, L. K. Deutsch, J.-S. Huang, S. Kleiner, M. Marengo, S. T. Megeath, G. J. Melnick, M. A. Pahre, B. M. Patten, J. Polizotti, H. A. Smith, R. S. Taylor, Z. Wang, S. P. Willner, W. F. Hoffmann, J. L. Pipher, W. J. Forrest, C. W. McMurty, C. R. McCreight, M. E. McKelvey, R. E. McMurray, D. G. Koch, S. H. Moseley, R. G. Arendt, J. E. Mentzell, C. T. Marx, P. Losch, P. Mayman, W. Eichhorn, D. Krebs, M. Jhabvala, D. Y. Gezari, D. J. Fixsen, J. Flores, K. Shakoorzadeh, R. Jungo, C. Hakun, L. Workman, G. Karpati, R. Kichak, R. Whitley, S. Mann, E. V. Tollestrup, P. Eisenhardt, D. Stern, V. Gorjian, B. Bhattacharya, S. Carey, B. O. Nelson, W. J. Glaccum, M. Lacy, P. J. Lowrance, S. Laine, W. T. Reach, J. A. Stauffer, J. A. Surace, G. Wilson, E. L. Wright, A. Hoffman, G. Domingo, and M. Cohen. The Infrared Array Camera (IRAC) for the Spitzer Space Telescope. *ApJS*, 154:10, 2004.

L. Fossati, C. A. Haswell, C. S. Froning, L. Hebb, S. Holmes, U. Kolb, C. Helling, A. Carter, P. Wheatley, A. Collier Cameron, B. Loeillet, D. Pollacco, R. Street, H. C. Stempels, E. Simpson, S. Udry, Y. C. Joshi, R. G. West, I. Skillen, and D. Wilson. Metals in the Exosphere of the Highly Irradiated Planet WASP-12b. *ApJL*, 714:L222, 2010.

J. P. Gardner, J. C. Mather, M. Clampin, R. Doyon, M. A. Greenhouse, H. B. Hammel, J. B. Hutchings, P. Jakobsen, S. J. Lilly, K. S. Long, J. I. Lunine, M. J. McCaughrean, M. Mountain, J. Nella, G. H. Rieke, M. J. Rieke, H.-W. Rix, E. P. Smith, G. Sonneborn, M. Stiavelli, H. S. Stockman, R. A. Windhorst, and G. S. Wright. Science with the James Webb space telescope. *Proc. SPIE*, 6265:62650N, 2006.

N. P. Gibson, S. Aigrain, J. K. Barstow, T. M. Evans, L. N. Fletcher, and P. G. J. Irwin. The optical transmission spectrum of the hot Jupiter HAT-P-32b: clouds explain the absence of broad spectral features? *MNRAS*, 436:2974, 2013.

M. Gillon, F. Pont, B.-O. Demory, F. Mallmann, M. Mayor, T. Mazeh, D. Queloz, A. Shporer, S. Udry, and C. Vuissoz. Detection of transits of the nearby hot Neptune GJ 436 b. *A&A*, 472:L13, 2007.

G. Gilmore, S. Randich, M. Asplund, J. Binney, P. Bonifacio, J. Drew, S. Feltzing, A. Ferguson, R. Jeffries, G. Micela, and et al. The Gaia-ESO Public Spectroscopic Survey. *The Messenger*, 147:25, 2012.

C. A. Griffith. Disentangling degenerate solutions from primary transit and secondary eclipse spectroscopy of exoplanets. *Philosophical Transactions of the Royal Society of London Series A*, 372:20130086, 2014.

C. J. Grillmair, D. Charbonneau, A. Burrows, L. Armus, J. Stauffer, V. Meadows, J. Van Cleve, and D. Levine. A Spitzer Spectrum of the Exoplanet HD 189733b. *ApJL*, 658:L115, 2007.

C. J. Grillmair, A. Burrows, D. Charbonneau, L. Armus, J. Stauffer, V. Meadows, J. van Cleve, K. von Braun, and D. Levine. Strong water absorption in the dayside emission spectrum of the planet HD189733b. *Nature*, 456:767, 2008.

C. J. Grillmair, S. J. Carey, J. R. Stauffer, M. E. Fisher, R. Olds, J. G. Ingalls, J. E. Krick, W. J. Glaccum, S. Laine, P. J. Lowrance, and J. A. Surace. Pointing effects and their consequences for Spitzer IRAC exoplanet observations. In *Proc. SPIE*, volume 8448, page 84481I, 2012.

H. Haario, M. Laine, A. Mira, and E. Saksman. DRAM: Efficient adaptive MCMC. *Statistics and Computing*, 16:339, 2006.

G. W. Henry, G. W. Marcy, R. P. Butler, and S. S. Vogt. A Transiting "51 Peg-like" Planet. *ApJ*, 529:L41, 2000.

T. Hirano, N. Narita, B. Sato, J. N. Winn, W. Aoki, M. Tamura, A. Taruya, and Y. Suto. Further Observations of the Tilted Planet XO-3: A New Determination of Spin-Orbit Misalignment, and Limits on Differential Rotation. *PASJ*, 63:L57, 2011.

M. J. Holman and N. W. Murray. The use of transit timing to detect terrestrial-mass extrasolar planets. *Science*, 307:1288, 2005.

A. W. Howard, J. A. Johnson, G. W. Marcy, D. A. Fischer, J. T. Wright, D. Bernat, G. W. Henry, K. M. G. Peek, H. Isaacson, K. Apps, M. Endl, W. D. Cochran, J. A. Valenti, J. Anderson, and N. E. Piskunov. The California Planet Survey. I. Four New Giant Exoplanets. *ApJ*, 712: 1467, 2010.

I. D. Howarth. On stellar limb darkening and exoplanetary transits. *MNRAS*, 418:1165, 2011a.

I. D. Howarth. New limb-darkening coefficients and synthetic photometry for model-atmosphere grids at Galactic, LMC and SMC abundances. *MNRAS*, 413:1515, 2011b.

R. Hu, S. Seager, and Y. L. Yung. Helium Atmosphere on Warm Neptune- and Sub-Neptune-Sized Exoplanets and Applications to GJ436 b. *ApJ*, 807:8, 2015.

D. Huber, J. A. Carter, M. Barbieri, A. Miglio, K. M. Deck, D. C. Fabrycky, D. T. Montet, L. A. Buchhave, W. J. Chaplin, S. Hekker, J. Montalbán, R. Sanchis-Ojeda, S. Basu, T. R. Bedding, T. L. Campante, and al. Stellar Spin-Orbit Misalignment in a Multiplanet System. *Science*, 342:331, 2013.

A. Hyv̈arinen. Fast and robust fixed-point algorithms for independent component analysis. *Neural Networks, IEEE Transactions on*, 10:626, 1999.

A. Hyvärinen and E. Oja. Independent component analysis: algorithms and applications. *Neural Networks*, 13:411, 2000.

A. Hyvärinen, J. Karhunen, and Oja E. *Independent Component Analysis*. Wiley & Sons Inc., 2001a.

A. Hyvärinen, J. Karhunen, and E. Oja. *Independent Component Analysis*. John Wiley & Sons, Inc., 2001b.

J. G. Ingalls, S. J. Carey, P. J. Lowrance, C. J. Grillmair, and J. R. Stauffer. Using drift scans to improve astrometry with Spitzer. In *Space Telescopes and Instrumentation 2014: Optical, Infrared, and Millimeter Wave*, volume 9143 of *Proc. SPIE*, page 91431M, 2014.

J. G. Ingalls, J. E. Krick, S. J. Carey, J. R. Stauffer, P. J. Lawrence, C. J. Grillmair, D. Buzasi, D. Deming, H. Diamond-Lowe, T. M. Evans, G. Morello, K. B. Stevenson, I. Wong, P. Capak, W. Glaccum, S. Laine, J. Surace, and L. Storrie-Lombardi. Repeatability and Accuracy of Exoplanet Eclipse Depths Measured with Post-Cryogenic Spitzer. *AJ*, 152:44, 2016.

G. Inuso, F. La Foresta, N. Mammone, and F. C. Morabito. Wavelet-ICA methodology for efficient artifact removal from Electroencephalographic recordings. In *IEEE International Conference on Neural Networks - Conference Proceedings*, volume 4371184, page 1524, 2007.

A. G. Jensen, S. Redfield, M. Endl, W. D. Cochran, L. Koesterke, and T. Barman. A Detection of Hα in an Exoplanetary Exosphere. *ApJ*, 751:86, 2012.

C. M. Johns-Krull, P. R. McCullough, C. J. Burke, J. A. Valenti, K. A. Janes, J. N. Heasley, L. Prato, R. Bissinger, M. Fleenor, C. N. Foote, E. Garcia-Melendo, B. L. Gary, P. J. Howell, F. Mallia, G. Masi, and T. Vanmunster. XO-3b: A Massive Planet in an Eccentric Orbit Transiting an F5 V Star. *ApJ*, 677:657, 2008.

I. T. Jolliffe. *Principal Component Analysis*. Springer, 2 edition, 2002.

A. Jordán and G. A. Bakos. Observability of the general relativistic precession of periastra in exoplanets. *ApJ*, 685:543, 2008.

J. A. Kammer, H. A. Knutson, M. R. Line, J. J. Fortney, D. Deming, A. Burrows, N. B. Cowan, A. H. M. J. Triaud, E. Agol, J.-M. Desert, B. J. Fulton, A. W. Howard, G. P. Laughlin, N. K. Lewis, C. V. Morley, J. I. Moses, A. P. Showman, and K. O. Todorov. Spitzer Secondary Eclipse Observations of Five Cool Gas Giant Planets and Empirical Trends in Cool Planet Emission Spectra. *ApJ*, 810:118, 2015.

K. J. Karande and S. Talbar. *Independent Component Analysis of Edge Information for Face Recognition*. Springer India, 2014. ISBN 978-81-322-1511-0.

T. Kataria, A. P. Showman, N. K. Lewis, J. J. Fortney, M. S. Marley, and R. S. Freedman. Three-dimensional Atmospheric Circulation of Hot Jupiters on Highly Eccentric Orbits. *ApJ*, 767:76, 2013.

M. Kerr, S. Johnston, G. Hobbs, and R. M. Shannon. Limits on Planet Formation Around Young Pulsars and Implications for Supernova Fallback Disks. *ApJL*, 809:L11, 2015.

D. M. Kipping. Transiting planets - light-curve analysis for eccentric orbits. *MNRAS*, 389:1383, 2008.

D. M. Kipping. Transit timing effects due to an exomoon. *MNRAS*, 392:181, 2009a.

D. M. Kipping. Transit timing effects due to an exomoon - II. *MNRAS*, 396:1797, 2009b.

D. M. Kipping. Investigations of approximate expressions for the transit duration. *MNRAS*, 407:301, 2010.

D. M. Kipping. Bayesian priors for the eccentricity of transiting planets. *MNRAS*, 444:2263, 2014.

K. Kiviluoto and E. Oja. Independent component analysis for paral- lel financial time series. In *Proceedings of the International Conference on Neural Information Processing*, volume 2, page 895, 1998.

H. A. Knutson, D. Charbonneau, L. E. Allen, J. J. Fortney, E. Agol, N. B. Cowan, A. P. Showman, C. S. Cooper, and S. T. Megeath. A map of the day-night contrast of the extrasolar planet HD 189733b. *Nature*, 447:183, 2007a.

H. A. Knutson, D. Charbonneau, R. W. Noyes, T. M. Brown, and R. L. Gilliland. Using Stellar Limb-Darkening to Refine the Properties of HD 209458b. *ApJ*, 655:564, 2007b.

H. A. Knutson, D. Charbonneau, L. E. Allen, A. Burrows, and S. T. Megeath. The 3.6-8.0 μm Broadband Emission Spectrum of HD 209458b: Evidence for an Atmospheric Temperature Inversion. *ApJ*, 673:526, 2008.

H. A. Knutson, D. Charbonneau, N. B. Cowan, J. J. Fortney, A. P. Showman, E. Agol, G. W. Henry, M. E. Everett, and L. E. Allen. Multiwavelength Constraints on the Day-Night Circulation Patterns of HD 189733b. *ApJ*, 690:822, 2009.

H. A. Knutson, N. Madhusudhan, N. B. Cowan, J. L. Christiansen, E. Agol, D. Deming, J.-M. Désert, D. Charbonneau, G. W. Henry, D. Homeier, J. Langton, G. Laughlin, and S. Seager. A Spitzer Transmission Spectrum for the Exoplanet GJ 436b, Evidence for Stellar Variability, and Constraints on Dayside Flux Variations. *ApJ*, 735:27, 2011.

H. A. Knutson, N. Lewis, J. J. Fortney, A. Burrows, A. P. Showman, N. B. Cowan, E. Agol, S. Aigrain, D. Charbonneau, D. Deming, J.-M. Désert, G. W. Henry, J. Langton, and G. Laughlin. 3.6 and 4.5 μm Phase Curves and Evidence for Non-equilibrium Chemistry in the Atmosphere of Extrasolar Planet HD 189733b. *ApJ*, 754:22, 2012.

H. A. Knutson, B. Benneke, D. Deming, and D. Homeier. A featureless transmission spectrum for the Neptune-mass exoplanet GJ436b. *Nature*, 505:66, 2014a.

H. A. Knutson, D. Dragomir, L. Kreidberg, E. M.-R. Kempton, P. R. McCullough, J. J. Fortney, J. L. Bean, M. Gillon, D. Homeier, and A. W. Howard. Hubble Space Telescope Near-IR Transmission Spectroscopy of the Super-Earth HD 97658b. *ApJ*, 794:155, 2014b.

Z. Koldovsky, P. Tichavsky, and E. Oja. Efficient variant of algorithm fastica for independent component analysis attaining the cramer-rao lower bound. *Neural Networks, IEEE Transactions on*, 17:1265, 2006.

M. Konacki. An extrasolar giant planet in a close triple-star system. *Nature*, 436:230, 2005.

L. Kreidberg, J. L. Bean, J.-M. Désert, B. Benneke, D. Deming, K. B. Stevenson, S. Seager, Z. Berta-Thompson, A. Seifahrt, and D. Homeier. Clouds in the atmosphere of the super-Earth exoplanet GJ1214b. *Nature*, 505:69, 2014.

J.. Krick, J. Ingalls, S. Carey, C. Grillmair, P. Lowrance, W. Glaccum, J. Surace, S. Laine, and P. Capak. IRAC High Precision Photometry Website. `http://irachpp.spitzer.caltech.edu`, 2015.

J. E. Krick, J. Ingalls, S. Carey, K. von Braun, S. R. Kane, D. Ciardi, P. Plavchan, I. Wong, and P. Lowrance. Spitzer IRAC Sparsely Sampled Phase Curve of the Exoplanet Wasp-14B. *ApJ*, 824:27, 2016.

F. La Foresta, N. Mammone, and F. C. Morabito. *Artifact Cancellation from Electrocardiogram by Mixed Wavelet-ICA Filter*, volume 3931 of *Lecture Notes in Computer Science*, page 78. Springer Berlin Heidelberg, Berlin, Heidelberg, 2006.

J. C. Lagarias, J. A. Reeds, M. H. Wright, and P. E. Wright. Convergence Properties of the Nelder-Mead Simplex Method in Low Dimensions. *SIAM Journal on Optimization*, 9:112, 1998.

J. Langton and G. Laughlin. Hydrodynamic Simulations of Unevenly Irradiated Jovian Planets. *ApJ*, 674:1106, 2008.

A. Lecavelier Des Etangs, D. Ehrenreich, A. Vidal-Madjar, G. E. Ballester, J.-M. Désert, R. Ferlet, G. Hébrard, D. K. Sing, K.-O. Tchakoumegni, and S. Udry. Evaporation of the planet HD 189733b observed in H I Lyman-α. *A&A*, 514:A72, 2010.

J.-M. Lee, L. N. Fletcher, and P. G. J. Irwin. Optimal estimation retrievals of the atmospheric structure and composition of HD 189733b from secondary eclipse spectroscopy. *MNRAS*, 420: 170, 2012.

N. K. Lewis, H. A. Knutson, A. P. Showman, N. B. Cowan, G. Laughlin, A. Burrows, D. Deming, J. R. Crepp, K. J. Mighell, E. Agol, G. Á. Bakos, D. Charbonneau, J.-M. Désert, D. A. Fischer, J. J. Fortney, J. D. Hartman, S. Hinkley, A. W. Howard, J. A. Johnson, M. Kao, J. Langton, and G. W. Marcy. Orbital phase variations of the eccentric giant planet HAT-P-2b. *ApJ*, 766: 95, 2013.

J. Lin and A. Zhang. Fault feature separation using wavelet-ICA filter. *NDT and E International*, 38:421, 2005.

M. R. Line, X. Zhang, G. Vasisht, V. Natraj, P. Chen, and Y. L. Yung. Information Content of Exoplanetary Transit Spectra: An Initial Look. *ApJ*, 749:93, 2012.

J. L. Linsky, H. Yang, K. France, C. S. Froning, J. C. Green, J. T. Stocke, and S. N. Osterman. Observations of Mass Loss from the Transiting Exoplanet HD 209458b. *ApJ*, 717:1291, 2010.

C. Lovis, F. Pepe, F. Bouchy, G. Lo Curto, M. Mayor, L. Pasquini, D. Queloz, G. Rupprecht, S. Udry, and S. Zucker. The exoplanet hunter HARPS: unequalled accuracy and perspectives toward 1 cm s $^{-1}$ precision. In *Society of Photo-Optical Instrumentation Engineers (SPIE) Conference Series*, volume 6269, page 62690P, 2006.

B. Macintosh, J. Graham, D. Palmer, R. Doyon, D. Gavel, J. Larkin, B. Oppenheimer, L. Saddlemyer, J. K. Wallace, B. Bauman, J. Evans, D. Erikson, K. Morzinski, D. Phillion, L. Poyneer, A. Sivaramakrishnan, R. Soummer, S. Thibault, and J.-P. Veran. The Gemini Planet Imager. *Proc. SPIE*, 6272:62720L, 2006.

N. Madhusudhan and S. Seager. A Temperature and Abundance Retrieval Method for Exoplanet Atmospheres. *ApJ*, 707:24, 2009.

N. Madhusudhan, K. K. M. Lee, and O. Mousis. A Possible Carbon-Rich Interior in Super-Earth 55 Cancri e. *ApJL*, 759:L40, 2012.

D. Maino, A. Farusi, C. Baccigalupi, F. Perrotta, A. J. Banday, L. Bedini, C. Burigana, G. De Zotti, K. M. Górski, and E. Salerno. All-sky astrophysical component separation with Fast Independent Component Analysis (FASTICA). *MNRAS*, 334:53, 2002.

D. Maino, S. Donzelli, A. J. Banday, F. Stivoli, and C. Baccigalupi. Cosmic microwave background signal in Wilkinson Microwave Anisotropy Probe three-year data with FASTICA. *MNRAS*, 374:1207, 2007.

A.-L. Maire, M. Bonnefoy, C. Ginski, A. Vigan, S. Messina, D. Mesa, R. Galicher, R. Gratton, S. Desidera, T. G. Kopytova, M. Millward, C. Thalmann, R. U. Claudi, D. Ehrenreich, A. Zurlo, G. Chauvin, J. Antichi, A. Baruffolo, A. Bazzon, J.-L. Beuzit, P. Blanchard, A. Boccaletti, J. de Boer, M. Carle, E. Cascone, A. Costille, V. De Caprio, A. Delboulbé, K. Dohlen, C. Dominik, M. Feldt, T. Fusco, J. H. Girard, E. Giro, D. Gisler, L. Gluck, C. Gry, T. Henning, N. Hubin, E. Hugot, M. Jaquet, M. Kasper, A.-M. Lagrange, M. Langlois, D. Le Mignant, M. Llored, F. Madec, P. Martinez, D. Mawet, J. Milli, O. Möller-Nilsson, D. Mouillet, T. Moulin, C. Moutou, A. Origné, A. Pavlov, C. Petit, J. Pragt, P. Puget, J. Ramos, S. Rochat, R. Roelfsema, B. Salasnich, J.-F. Sauvage, H. M. Schmid, M. Turatto, S. Udry, F. Vakili, Z. Wahhaj, L. Weber, and F. Wildi. First light of the VLT planet finder SPHERE. II. The physical properties and the architecture of the young systems PZ Telescopii and HD 1160 revisited. *A&A*, 587:A56, 2016.

N. Mammone, F. La Foresta, and F. C. Morabito. Automatic artifact rejection from multichannel scalp EEG by wavelet ICA. *IEEE Sensors Journal*, 12:533, 2012.

K. Mandel and E. Agol. Analytic Light Curves for Planetary Transit Searches. *ApJl*, 580:L171, 2002.

A. M. Mandell, L. Drake Deming, G. A. Blake, H. A. Knutson, M. J. Mumma, G. L. Villanueva, and C. Salyk. Non-detection of L-band Line Emission from the Exoplanet HD189733b. *ApJ*, 728:18, 2011.

H. L. Maness, G. W. Marcy, E. B. Ford, P. H. Hauschildt, A. T. Shreve, G. B. Basri, R. P. Butler, and S. S. Vogt. The M Dwarf GJ 436 and its Neptune-Mass Planet. *PASP*, 119:90, 2007.

M. Mayor and D. Queloz. A Jupiter-mass companion to a solar-type star. *Nature*, 378:355, 1995.

M. Mayor, F. Pepe, D. Queloz, F. Bouchy, G. Rupprecht, G. Lo Curto, G. Avila, W. Benz, J.-L. Bertaux, X. Bonfils, T. Dall, H. Dekker, B. Delabre, W. Eckert, M. Fleury, A. Gilliotte, D. Gojak, J. C. Guzman, D. Kohler, J.-L. Lizon, A. Longinotti, C. Lovis, D. Megevand, L. Pasquini, J. Reyes, J.-P. Sivan, D. Sosnowska, R. Soto, S. Udry, A. van Kesteren, L. Weber, and U. Weilenmann. Setting New Standards with HARPS. *The Messenger*, 114:20, 2003.

M. Mayor, X. Bonfils, T. Forveille, X. Delfosse, S. Udry, J.-L. Bertaux, H. Beust, F. Bouchy, C. Lovis, F. Pepe, C. Perrier, D. Queloz, and N. C. Santos. The HARPS search for southern extra-solar planets. XVIII. An Earth-mass planet in the GJ 581 planetary system. *A&A*, 507: 487, 2009.

M. Morales-Calderón, J. R. Stauffer, J. D. Kirkpatrick, S. Carey, C. R. Gelino, D. Barrado y Navascués, L. Rebull, P. Lowrance, M. S. Marley, D. Charbonneau, B. M. Patten, S. T. Megeath, and D. Buzasi. A sensitive search for variability in late L dwarfs: the quest for weather. *ApJ*, 653:1454, 2006.

G. Morello. A Blind Method to Detrend Instrumental Systematics in Exoplanetary Light Curves. *ApJ*, 808:56, 2015.

G. Morello, I. P. Waldmann, G. Tinetti, G. Peres, G. Micela, and I. D. Howarth. A New Look at Spitzer Primary Transit Observations of the Exoplanet HD 189733b. *ApJ*, 786:22, 2014.

G. Morello, I. P. Waldmann, G. Tinetti, I. D. Howarth, G. Micela, and F. Allard. Revisiting Spitzer Transit Observations with Independent Component Analysis: New Results for the GJ 436 System. *ApJ*, 802:117, 2015.

G. Morello, I. P. Waldmann, and G. Tinetti. Repeatability of Spitzer/IRAC Exoplanetary Eclipses with Independent Component Analysis. *ApJ*, 820:86, 2016.

R. Moussaoui, J. Rouat, and R. Lefebvre. Wavelet Based Independent Component Analysis for Multi-Channel Source Separation. In *2006 IEEE International Conference on Acoustics Speech and Signal Processing Proceedings*, volume 5, page V, 2006.

C. D. Murray and A. C. M. Correia. Keplerian Orbits and Dynamics of Exoplanets. arXiv:1009.1738v2, 2011.

M. W. Muterspaugh, B. F. Lane, S. R. Kulkarni, M. Konacki, B. F. Burke, M. M. Colavita, M. Shao, W. I. Hartkopf, A. P. Boss, and M. Williamson. The Phases Differential Astrometry Data Archive. V. Candidate Substellar Companions to Binary Systems. *ApJ*, 140:1657, 2010.

D. Naef, D. W. Latham, M. Mayor, T. Mazeh, J. L. Beuzit, G. A. Drukier, C. Perrier-Bellet, D. Queloz, J. P. Sivan, G. Torres, S. Udry, and S. Zucker. HD 80606 b, a planet on an extremely elongated orbit. *A&A*, 375:4, 2001.

D. Nesvorny, D. Kipping, D. Terrell, J. Hartman, G. Á. Bakos, and L. A. Buchhave. KOI142, the king of transit variations, is a pair of planets near the 2:1 resonance. *ApJ*, 777:3, 2013.

S. J. O'Toole, C. G. Tinney, H. R.A. Jones, R. P. Butler, G. W. Marcy, B. Carter, and J. Bailey. Selection functions in doppler planet searches. *MNRAS*, 392:641, 2009.

A. Pál and B Kocsis. Periastron precession measurements in transiting extrasolar planetary systems at the level of general relativity. *MNRAS*, 389:191, 2008.

L. Pasquini, S. Cristiani, R. Garcia-Lopez, M. Haehnelt, and M. Mayor. CODEX: An Ultrastable High Resolution Spectrograph for the E-ELT. *The Messenger*, 140:20, 2010.

F. Pepe, P. Molaro, S. Cristiani, R. Rebolo, N. C. Santos, H. Dekker, D. Megevand, F. M. Zerbi, A. Cabral, P. Di Marcantonio, M. Abreu, M. Affolter, M. Aliverti, C. Allende Prieto, M. Amate, G. Avila, V. Baldini, P. Bristow, C. Broeg, R. Cirami, J. Coelho, P. Conconi, I. Coretti, G. Cupani, V. D'Odorico, V. De Caprio, B. Delabre, R. Dorn, P. Figueira, A. Fragoso, S. Galeotta, L. Genolet, R. Gomes, J. I. González Hernández, I. Hughes, O. Iwert, F. Kerber, M. Landoni, J.-L. Lizon, C. Lovis, C. Maire, M. Mannetta, C. Martins, M. Monteiro, A. Oliveira, E. Poretti, J. L. Rasilla, M. Riva, S. Santana Tschudi, P. Santos, D. Sosnowska, S. Sousa, P. Spanò, F. Tenegi, G. Toso, E. Vanzella, M. Viel, and M. R. Zapatero-Osorio. Espresso: The next european exoplanet hunter. *Astronomische Nachrichten*, 335:8, 2014.

D. B. Percival and A. T. Walden. *Wavelet Methods for Time Series Analysis*. Cambridge University Press, 2000.

M. Perryman, J. Hartman, G. Á. Bakos, and L. Lindegren. Astrometric Exoplanet Detection with Gaia. *ApJ*, 797:14, 2014.

F. Pont, H. Knutson, R. L. Gilliland, C. Moutou, and D. Charbonneau. Detection of atmospheric haze on an extrasolar planet: the 0.55-1.05 μm transmission spectrum of HD 189733b with the HubbleSpaceTelescope. *MNRAS*, 385:109, 2008.

F. Pont, R. L. Gilliland, H. Knutson, M. Holman, and D. Charbonneau. Transit infrared spectroscopy of the hot Neptune around GJ 436 with the Hubble Space Telescope. *MNRAS*, 393: L6, 2009.

F. Pont, D. K. Sing, N. P. Gibson, S. Aigrain, G. Henry, and N. Husnoo. The prevalence of dust on the exoplanet HD 189733b from Hubble and Spitzer observations. *MNRAS*, 432:2917, 2013.

S. Rappaport, R. Sanchis-Ojeda, L. A. Rogers, A. Levine, and J. N. Winn. The Roche Limit for Close-Orbiting Planets: Minimum Density, Composition Constraints, and Applications to the 4.2 hr Planet KOI 1843.03. *ApJL*, 773:L15, 2013.

H. Rauer, C. Catala, C. Aerts, T. Appourchaux, W. Benz, A. Brandeker, J. Christensen-Dalsgaard, M. Deleuil, L. Gizon, M.-J. Goupil, M. Güdel, E. Janot-Pacheco, M. Mas-Hesse, I. Pagano, G. Piotto, D. Pollacco, Ċ. Santos, A. Smith, J.-C. Suárez, R. Szabó, S. Udry, V. Adibekyan, Y. Alibert, J.-M. Almenara, P. Amaro-Seoane, M. A.-v. Eiff, M. Asplund, E. Antonello, S. Barnes, F. Baudin, K. Belkacem, M. Bergemann, G. Bihain, A. C. Birch, X. Bonfils, I. Boisse, A. S. Bonomo, F. Borsa, I. M. Brandão, E. Brocato, S. Brun, M. Burleigh, R. Burston, J. Cabrera, S. Cassisi, W. Chaplin, S. Charpinet, C. Chiappini, R. P. Church, S. Csizmadia, M. Cunha, M. Damasso, M. B. Davies, H. J. Deeg, R. F. Díaz, S. Dreizler, C. Dreyer, P. Eggenberger, D. Ehrenreich, P. Eigmüller, A. Erikson, R. Farmer, S. Feltzing, F. de Oliveira Fialho, P. Figueira, T. Forveille, M. Fridlund, R. A. García, P. Giommi, G. Giuffrida, M. Godolt, J. Gomes da Silva, T. Granzer, J. L. Grenfell, A. Grotsch-Noels, E. Günther, C. A. Haswell, A. P. Hatzes, G. Hébrard, S. Hekker, R. Helled, K. Heng, J. M. Jenkins, A. Johansen, M. L. Khodachenko, K. G. Kislyakova, W. Kley, U. Kolb, N. Krivova, F. Kupka, H. Lammer, A. F. Lanza, Y. Lebreton, D. Magrin, P. Marcos-Arenal, P. M. Marrese, J. P. Marques, J. Martins, S. Mathis, S. Mathur, S. Messina, A. Miglio, J. Montalban, M. Montalto, M. J. P. F. G. Monteiro, H. Moradi, E. Moravveji, C. Mordasini, T. Morel, A. Mortier, V. Nascimbeni, R. P. Nelson, M. B. Nielsen, L. Noack, A. J. Norton, A. Ofir, M. Oshagh, R.-M. Ouazzani, P. Pápics, V. C. Parro, P. Petit, B. Plez, E. Poretti, A. Quirrenbach, R. Ragazzoni, G. Raimondo, M. Rainer, D. R. Reese, R. Redmer, S. Reffert, B. Rojas-Ayala, I. W. Roxburgh, S. Salmon, A. Santerne, J. Schneider, J. Schou, S. Schuh, H. Schunker, A. Silva-Valio, R. Silvotti, I. Skillen, I. Snellen, F. Sohl, S. G. Sousa, A. Sozzetti, D. Stello, K. G. Strassmeier, M. Švanda, G. M. Szabó, A. Tkachenko, D. Valencia, V. Van Grootel, S. D. Vauclair, P. Ventura, F. W. Wagner, N. A. Walton, J. Weingrill, S. C. Werner, P. J. Wheatley, and K. Zwintz. The PLATO 2.0 mission. *Experimental Astronomy*, 38:249, 2014.

W. T. Reach, S. T. Megeath, M. Cohen, J. Hora, S. Carey, J. Surace, S. P. Willner, P. Barmby, G. Wilson, W. Glaccum, P. Lowrance, M. Marengo, and G. G. Fazio. Absolute Calibration of the Infrared Array Camera on the Spitzer Space Telescope. *PASP*, 117:978, 2005.

I. Ribas, A. Font-Ribera, and J.-P. Beaulieu. A ˜5 M Super-Earth Orbiting GJ 436? The Power of Near-Grazing Transits. *ApJL*, 677:L59, 2008.

L. J. Richardson, D. Deming, K. Horning, S. Seager, and J. Harrington. A spectrum of an extrasolar planet. *Nature*, 445:892, 2007.

G. R. Ricker, J. N. Winn, R. Vanderspek, D. W. Latham, G. Á. Bakos, J. L. Bean, Z. K. Berta-Thompson, and T. M. Brown. Transiting exoplanet survey satellite. *Journal of Astronomical Telescopes, Instruments, and Systems*, 1:014003, 2014.

E. Schlawin, E. Agol, L. M. Walkowicz, K. Covey, and J. P. Lloyd. Exoplanetary Transits of Limb-brightened Lines: Tentative Si IV Absorption by HD 209458b. *ApJL*, 722:L75, 2010.

J. Schneider, C. Dedieu, P. Le Sidaner, R. Savalle, and I. Zolotukhin. Defining and cataloging exoplanets: the exoplanet.eu database. *A&A*, 532:A79, August 2011. doi: 10.1051/0004-6361/201116713.

S. Seager and G. Mallén-Ornelas. A Unique Solution of Planet and Star Parameters from an Extrasolar Planet Transit Light Curve. *ApJ*, 585:1038, 2003.

A. P. Showman, C. S. Cooper, J. J. Fortney, and M. S. Marley. Atmospheric Circulation of Hot Jupiters: Three-dimensional Circulation Models of HD 209458b and HD 189733b with Simplified Forcing. *ApJ*, 682:559, 2008a.

A. P. Showman, C. S. Cooper, J. J. Fortney, and M. S. Marley. Erratum: "Atmospheric Circulation of Hot Jupiters: Three-dimensional Circulation Models of HD 209458b and HD 189733b with Simplified Forcing" (ApJ, 682, 559 [2008]). *ApJ*, 685:1324, 2008b.

A. P. Showman, J. J. Fortney, Y. Lian, M. S. Marley, R. S. Freedman, H. A. Knutson, and D. Charbonneau. Atmospheric Circulation of Hot Jupiters: Coupled Radiative-Dynamical General Circulation Model Simulations of HD 189733b and HD 209458b. *ApJ*, 699:564, 2009.

D. K. Sing, J.-M. Désert, A. Lecavelier Des Etangs, G. E. Ballester, A. Vidal-Madjar, V. Parmentier, G. Hebrard, and G. W. Henry. Transit spectrophotometry of the exoplanet HD 189733b. I. Searching for water but finding haze with HST NICMOS. *A&A*, 505:891, 2009.

D. K. Sing, J.-M. Désert, J. J. Fortney, A. Lecavelier Des Etangs, G. E. Ballester, J. Cepa, D. Ehrenreich, M. López-Morales, F. Pont, M. Shabram, and A. Vidal-Madjar. Gran Telescopio Canarias OSIRIS transiting exoplanet atmospheric survey: detection of potassium in XO-2b from narrowband spectrophotometry. *A&A*, 527:A73, 2011a.

D. K. Sing, F. Pont, S. Aigrain, D. Charbonneau, J.-M. Désert, N. Gibson, R. Gilliland, W. Hayek, G. Henry, H. Knutson, A. Lecavelier Des Etangs, T. Mazeh, and A. Shporer. Hubble Space Telescope transmission spectroscopy of the exoplanet HD 189733b: high-altitude atmospheric haze in the optical and near-ultraviolet with STIS. *MNRAS*, 416:1443, 2011b.

I. A. G. Snellen, E. J. W. de Mooij, and A. Burrows. Bright optical day-side emission from extrasolar planet CoRoT-2b. *A&A*, 513:A76, 2010.

C.M. Stein. *Ann.Statist.*, 9:1135, 1981.

K. B. Stevenson, J. Harrington, S. Nymeyer, N. Madhusudhan, S. Seager, W. C. Bowman, R. A. Hardy, D. Deming, E. Rauscher, and N. B. Lust. Possible thermochemical disequilibrium in the atmosphere of the exoplanet GJ 436b. *Nature*, 464:1161, 2010.

K. B. Stevenson, J. Harrington, J. J. Fortney, T. J. Loredo, R. A. Hardy, S. Nymeyer, W. C. Bowman, P. Cubillos, M. O. Bowman, and M. Hardin. Transit and Eclipse Analyses of the Exoplanet HD 149026b Using BLISS Mapping. *ApJ*, 754:136, 2012.

F. Stivoli, C. Baccigalupi, D. Maino, and R. Stompor. Separating polarized cosmological and galactic emissions for cosmic microwave background B-mode polarization experiments. *MNRAS*, 372:615, 2006.

M. R. Swain, J. Bouwman, R. L. Akeson, S. Lawler, and C. A. Beichman. The Mid-Infrared Spectrum of the Transiting Exoplanet HD 209458b. *ApJ*, 674:482, 2008a.

M. R. Swain, G. Vasisht, and G. Tinetti. The presence of methane in the atmosphere of an extrasolar planet. *Nature*, 452:329, 2008b.

M. R. Swain, G. Tinetti, G. Vasisht, P. Deroo, C. Griffith, J. Bouwman, P. Chen, Y. Yung, A. Burrows, L. R. Brown, J. Matthews, J. F. Rowe, R. Kuschnig, and D. Angerhausen. Water, Methane, and Carbon Dioxide Present in the Dayside Spectrum of the Exoplanet HD 209458b. *ApJ*, 704:1616, 2009a.

M. R. Swain, G. Vasisht, G. Tinetti, J. Bouwman, P. Chen, Y. Yung, D. Deming, and P. Deroo. Molecular Signatures in the Near-Infrared Dayside Spectrum of HD 189733b. *ApJl*, 690:L114, 2009b.

M. R. Swain, P. Deroo, C. A. Griffith, G. Tinetti, A. Thatte, G. Vasisht, P. Chen, J. Bouwman, I. J. Crossfield, D. Angerhausen, C. Afonso, and T. Henning. A ground-based near-infrared emission spectrum of the exoplanet HD189733b. *Nature*, 463:637, 2010.

R. J. Terrile, L. Seungwon, G. Tinetti, W. Fink, P. Von Allmen, and T. L. Huntsberger. *Evolutionary computational methods for the design of spectral instruments*, volume 1-9, page 4364. 2008.

P. Tichavský, Z. Koldovský, E. Doron, A. Yeredor, and G. Gomez-Herrero. Blind signal separation by combining two ICA algorithms: HOS-based EFICA and time structure-based WASOBI. In *Proc. EUSIPCO-2006*, 2006.

P. Tichavsky, Z. Koldovsky, and E. Oja. Performance analysis of the fastica algorithm and crame rao bounds for linear independent component analysis. *Signal Processing, IEEE Transactions on*, 54:1189, 2006.

P. Tichavsky, Z. Koldovsky, A. Yeredor, G. Gomez-Herrero, and E. Doron. A hybrid technique for blind separation of non-gaussian and time-correlated sources using a multicomponent approach. *Neural Networks, IEEE Transactions on*, 19:421, 2008.

G. Tinetti, A. Vidal-Madjar, M.-C. Liang, J.-P. Beaulieu, Y. Yung, S. Carey, R. J. Barber, J. Tennyson, I. Ribas, N. Allard, G. E. Ballester, D. K. Sing, and F. Selsis. Water vapour in the atmosphere of a transiting extrasolar planet. *Nature*, 448:169, 2007.

G. Tinetti, P. Deroo, M. R. Swain, C. A. Griffith, G. Vasisht, L. R. Brown, C. Burke, and P. McCullough. Probing the Terminator Region Atmosphere of the Hot-Jupiter XO-1b with Transmission Spectroscopy. *ApJl*, 712:L139, 2010.

G. Torres, D. A. Fischer, A. Sozzetti, L. A. Buchhave, J. N. Winn, M. J. Holman, and J. A. Carter. Improved Spectroscopic Parameters for Transiting Planet Hosts. *ApJ*, 757:161, 2012.

A. Tsiaras, I. P. Waldmann, M. Rocchetto, R. Varley, G. Morello, and G. Tinetti. A new approach to analysing HST spatial scans: the transmission spectrum of HD 209458b. *ArXiv e-prints*, 1511.07796, 2015.

A. Tsiaras, M. Rocchetto, I. P. Waldmann, O. Venot, R. Varley, G. Morello, M. Damiano, G. Tinetti, E. J. Barton, S. N. Yurchenko, and J. Tennyson. Detection of an Atmosphere Around the Super-Earth 55 Cancri e. *ApJ*, 820:99, 2016.

A. Udalski, J. C. Yee, A. Gould, S. Carey, W. Zhu, J. Skowron, S. Kozlowski, R. Poleski, P. Pietrukowicz, G. Pietrzyński, M. K. Szymański, P. Mróz, I. Soszyński, K. Ulaczyk, Ł. Wyrzykowski, C. Han, S. Calchi Novati, and R. W. Pogge. Spitzer as a microlens parallax satellite: Mass measurement for the ogle-2014-blg-0124l planet and its host star. *ApJ*, 799:237, 2015.

R. Varley and A. Tsiaras. Wayne - A Simulator for HST WFC3 IR Grism Spectroscopy. *ArXiv e-prints*, 1511.07796, 2015.

A. Vidal-Madjar, A. Lecavelier des Etangs, J.-M. Désert, G. E. Ballester, R. Ferlet, G. Hébrard, and M. Mayor. An extended upper atmosphere around the extrasolar planet HD209458b. *Nature*, 422:143, 2003.

A. Vidal-Madjar, J.-M. Désert, A. Lecavelier des Etangs, G. Hébrard, G. E. Ballester, D. Ehrenreich, R. Ferlet, J. C. McConnell, M. Mayor, and C. D. Parkinson. Detection of Oxygen and Carbon in the Hydrodynamically Escaping Atmosphere of the Extrasolar Planet HD 209458b. *ApJL*, 604:L69, 2004.

A. Vigan, M. Bonnefoy, C. Ginski, H. Beust, R. Galicher, M. Janson, J.-L. Baudino, E. Buenzli, J. Hagelberg, V. D'Orazi, S. Desidera, A.-L. Maire, R. Gratton, J.-F. Sauvage, G. Chauvin, C. Thalmann, L. Malo, G. Salter, A. Zurlo, J. Antichi, A. Baruffolo, P. Baudoz, P. Blanchard, A. Boccaletti, J.-L. Beuzit, M. Carle, R. Claudi, A. Costille, A. Delboulbé, K. Dohlen, C. Dominik, M. Feldt, T. Fusco, L. Gluck, J. Girard, E. Giro, C. Gry, T. Henning, N. Hubin, E. Hugot, M. Jaquet, M. Kasper, A.-M. Lagrange, M. Langlois, D. Le Mignant, M. Llored, F. Madec, P. Martinez, D. Mawet, D. Mesa, J. Milli, D. Mouillet, T. Moulin, C. Moutou, A. Origné, A. Pavlov, D. Perret, C. Petit, J. Pragt, P. Puget, P. Rabou, S. Rochat, R. Roelfsema, B. Salasnich, H.-M. Schmid, A. Sevin, R. Siebenmorgen, A. Smette, E. Stadler, M. Suarez, M. Turatto, S. Udry, F. Vakili, Z. Wahhaj, L. Weber, and F. Wildi. First light of the VLT planet finder SPHERE. I. Detection and characterization of the substellar companion GJ 758 B. *A&A*, 587:A55, 2016.

R. Vigário, V. Jousmäki, M. Hämäläinen, R. Hari, and E. Oja. Independent Component Analysis for Identification of Artifacts in Magnetoencephalographic Recordings. In *Advances in Neural Information Processing Systems 10*, page 229. MIT Press, 1998.

I. P. Waldmann. Of "Cocktail Parties" and Exoplanets. *ApJ*, 747:12, 2012.

I. P. Waldmann. On signals faint and sparse: the ACICA algorithm for blind de-trending of exoplanetary transits with low signal-to-noise. *ApJ*, 780:23, 2014.

I. P. Waldmann, G. Tinetti, P. Drossart, M. R. Swain, P. Deroo, and C. A. Griffith. Ground-based Near-infrared Emission Spectroscopy of HD 189733b. *ApJ*, 744:35, 2012.

I. P. Waldmann, G. Tinetti, P. Deroo, M. D. J. Hollis, S. N. Yurchenko, and J. Tennyson. Blind Extraction of an Exoplanetary Spectrum through Independent Component Analysis. *ApJ*, 766:7, 2013.

I. P. Waldmann, M. Rocchetto, G. Tinetti, E. J. Barton, S. N. Yurchenko, and J. Tennyson. Tau-REx II: Retrieval of Emission Spectra. *ApJ*, 813:13, 2015a.

I. P. Waldmann, G. Tinetti, M. Rocchetto, E. J. Barton, S. N. Yurchenko, and J. Tennyson. Tau-REx I: A Next Generation Retrieval Code for Exoplanetary Atmospheres. *ApJ*, 802:107, 2015b.

J. Wang, H. Xu, J. Gu, T. An, H. Cui, J. Li, Z. Zhang, Q. Zheng, and X.-P. Wu. How to Identify and Separate Bright Galaxy Clusters from the Low-frequency Radio Sky. *ApJ*, 723:620, 2010.

J. N. Winn. Transits and occultations. arXiv:1001.2010v5, 2014.

J. N. Winn, M. J. Holman, G. Torres, P. McCullough, C. Johns-Krull, D. W. Latham, A. Shporer, T. Mazeh, E. Garcia-Melendo, C. Foote, G. Esquerdo, and M. Everett. The Transit Light Curve Project. IX. Evidence for a Smaller Radius of the Exoplanet XO-3b. *ApJ*, 683:1076, 2008.

A. Wolszczan and D. A. Frail. A planetary system around the millisecond pulsar PSR1257 + 12. *Nature*, 355:145, 1992.

I. Wong, H. A. Knutson, N. B. Cowan, N. K. Lewis, E. Agol, A. Burrows, D. Deming, J. J. Fortney, B. J. Fulton, J. Langton, G. Laughlin, and A. P. Showman. Constraints on the Atmospheric Circulation and Variability of the Eccentric Hot Jupiter XO-3b. *ApJ*, 794:134, 2014.

A. Yeredor. Blind separation of gaussian sources via second-order statistics with asymptotically optimal weighting. *Signal Processing Letters, IEEE*, 7:197, 2000.

R. T. Zellem, N. K. Lewis, H. A. Knutson, C. A. Griffith, A. P. Showman, J. J. Fortney, N. B. Cowan, E. Agol, A. Burrows, D. Charbonneau, D. Deming, G. Laughlin, and J. Langton. The 4.5 μm Full-orbit Phase Curve of the Hot Jupiter HD 209458b. *ApJ*, 790:53, 2014.

C. H. Zhao, J. Liu, and J. D. Sun. *Journal of Electronics and Information Technology*, 28:1565, 2006.

A. Zurlo, A. Vigan, R. Galicher, A.-L. Maire, D. Mesa, R. Gratton, G. Chauvin, M. Kasper, C. Moutou, M. Bonnefoy, S. Desidera, L. Abe, D. Apai, A. Baruffolo, P. Baudoz, J. Baudrand, J.-L. Beuzit, P. Blancard, A. Boccaletti, F. Cantalloube, M. Carle, E. Cascone, J. Charton, R. U. Claudi, A. Costille, V. de Caprio, K. Dohlen, C. Dominik, D. Fantinel, P. Feautrier, M. Feldt, T. Fusco, P. Gigan, J. H. Girard, D. Gisler, L. Gluck, C. Gry, T. Henning, E. Hugot, M. Janson, M. Jaquet, A.-M. Lagrange, M. Langlois, M. Llored, F. Madec, Y. Magnard, P. Martinez, D. Maurel, D. Mawet, M. R. Meyer, J. Milli, O. Moeller-Nilsson, D. Mouillet, A. Origné, A. Pavlov, P. Petit, C. andPuget, S. P. Quanz, P. Rabou, J. Ramos, G. Rousset, A. Roux, B. Salasnich, G. Salter, J.-F. Sauvage, H. M. Schmid, C. Soenke, E. Stadler, M. Suarez, M. Turatto, S. Udry, F. Vakili, Z. Wahhaj, F. Wildi, and J. Antichi. First light of the VLT planet finder SPHERE. III. New spectrophotometry and astrometry of the HR 8799 exoplanetary system. *A&A*, 587:A57, 2016.